0 0 0 0 4 2 0 5 9 9 4

LBL-3473
c. 1

GAS-PHASE PHOTOEMISSION WITH SOFT (NaKα, MgKα) AND ULTRASOFT (YMζ) X-RAY SOURCES

RECEIVED
LAWRENCE
BERKELEY LABORATORY

AUG 1 1975

LIBRARY AND
DOCUMENTS SECTION

Muhammad Salim Banna
(Ph. D. thesis)

March 1975

Prepared for the U. S. Energy Research and
Development Administration under Contract W-7405-ENG-48

For Reference

Not to be taken from this room

LAWRENCE BERKELEY LABORATORY
UNIVERSITY OF CALIFORNIA
BERKELEY

LBL-3473
c. 1

DISCLAIMER

This document was prepared as an account of work sponsored by the United States Government. While this document is believed to contain correct information, neither the United States Government nor any agency thereof, nor the Regents of the University of California, nor any of their employees, makes any warranty, express or implied, or assumes any legal responsibility for the accuracy, completeness, or usefulness of any information, apparatus, product, or process disclosed, or represents that its use would not infringe privately owned rights. Reference herein to any specific commercial product, process, or service by its trade name, trademark, manufacturer, or otherwise, does not necessarily constitute or imply its endorsement, recommendation, or favoring by the United States Government or any agency thereof, or the Regents of the University of California. The views and opinions of authors expressed herein do not necessarily state or reflect those of the United States Government or any agency thereof or the Regents of the University of California.

0 0 0 0 4 2 0 5 9 9 5

This thesis is dedicated to my mother.

CONTENTS

ABSTRACT v

I. INTRODUCTION 1

II. INSTRUMENTATION 5

A. *The Berkeley Iron-Free Spectrometer* 5

1. General Description 5

2. Calibration 7

3. Field Compensation System 8

B. *The Soft X-Ray Tubes*. 9

1. The X-Ray Tube Pumping System 10

2. The Magnesium/Aluminum X-Ray Tube 12

(a) Design 12

(b) Operation. 16

3. The Sodium X-Ray Tube 16

(a) Design 17

(b) Operation and performance. 20

(c) Possible improvements. 23

C. *The Ultrasoft X-Ray Tube*. 23

1. Motivation. 24

2. Description of Components 24

(a) The cathode assembly 33

(b) The anode. 34

(c) The window 35

3. Operation 36

4. Advantages 37

D. *Gaseous Sample Arrangements* 38

1. The Old Room Temperture Gas Cell. 39

2. The New Room Temperature Gas Cell 39

3. The Old Heated Gas Cell 42

4. The New Heated Gas Cell 42

III. ENERGY AND INTENSITY MEASUREMENT. 47

CONTENTS

IV. X-RAY EMISSION WITH NEON AS THE CONVERTER ATOM 50
A. *The K X-Ray Spectrum of Sodium* 50
B. *The M X-Ray Spectrum of Yttrium* 54

V. EXAMPLES OF HIGH TEMPERATURE GAS-PHASE SPECTRA 58
A. *NF_2 Radical*. 58
B. *Paranitroaniline* 58
C. *Other Systems*. 64

VI. EXAMPLES OF SPECTRA OBTAINED WITH SODIUM X-RAYS. 66
A. *Oxygen (1s)*. 66
B. *Methane (C1s)*. 68
C. *Metadifluorobenzene (C1s)*. 70
D. *Phosphorous Pentafluoride (F1s)*. 74

VII. THE RARE GASES NEON, ARGON, KRYPTON AND XENON. 76
A. *Results and Discussion* 76
1. Neon 76
2. Argon. 79
3. Krypton. 79
4. Xenon. 85
B. *Comparison of Relative Subshell Cross Sections with Theory* 87

VIII. THE ISOELECTRONIC HYDRIDES CH_4, NH_3, H_2O, AND HF 92
A. *Experimental* 92
B. *Binding Energies* 96
C. *Intensity Ratios* 100

IX. NITROGEN, CARBON MONOXIDE, ETHYLENE AND OXYGEN 109
A. *Nitrogen and Carbon Monoxide* 109
B. *Ethylene* 114
C. *Oxygen* 121

X. THE FLUORINATED METHANES CH_3F, CH_2F_2, CHF_3 AND CF_4 127

ACKNOWLEDGMENTS. 136
REFERENCES 137

0 0 0 0 4 2 0 5 9 9 7

GAS-PHASE PHOTOEMISSION WITH SOFT (NaKα, MgKα) AND ULTRASOFT (YMζ) X-RAY SOURCES

Muhammad Salim Banna

Nuclear Chemistry Division
Lawrence Berkeley Laboratory
University of California
Berkeley, California 94720

ABSTRACT

The Berkeley Iron-Free Photoelectron Spectrometer was equipped with three new x-ray tubes for the production of $AlK\alpha_{1,2}/MgK\alpha_{1,2}$ (1486.6 eV and 1253.6 eV respectively), $NaK\alpha_{1,2}$ (1041.0 eV) and YMζ (132.3 eV) x-rays. The (gaseous) target chamber was redesigned to allow for higher photoelectron intensity and peak-to-background ratio. Two heated cells were also constructed, one for pyrolyzing gases, the other for vaporizing solids. Design details are given for all of the above modifications.

The importance of high temperature work is illustrated by the core-level spectra of NF_2 radical (produced by pyrolyzing N_2F_4), and paranitroaniline. NF_2 shows a multiplet splitting of 1.93 eV. The spectrum of paranitroaniline contains intense satellite peaks attributable to multiple-electron transitions.

The x-ray satellites in the neighborhood of $NaK\alpha_{1,2}$ and YMζ were determined. The core levels of neon, oxygen, methane, metadifluorobenzene

(C1s) and PF_5 (F1s) were studied with NaKα in order to assess the advantages of the new source. A neon 1s linewidth of 0.59(1) eV was obtained (0.69(1) eV with $MgK\alpha_{1,2}$). The sodium line is shown to be potentially useful in photoelectron spectroscopy.

The molecular orbital region (up to ∿ 50 eV binding energy) of a number of gaseous systems was studied with MgKα and YMζ radiation. Relative intensities at both exciting energies are reported. For neon, argon and krypton, the valence p/s intensity ratio decreases in that order at 132.3 eV photon energy while increasing in the same order at 1253.6 eV photon energy. The former trend is predicted correctly by the theoretical calculations of Kennedy and Manson.

As in neon, it is shown that in a variety of compounds involving only second-row elements, the intensity of orbitals with 2s parentage decreases dramatically relative to the intensity of 2p-like orbitals when the exciting source is changed from MgKα to YMζ. This behavior is systematized by means of the simple intensity model proposed by Gelius, thus allowing orbital assignment in the fluoromethanes.

The relative molecular orbital intensities (plus core levels at the MgKα energy) in CH_4, NH_3, H_2O, HF, Ne, CO, N_2 and C_2H_4 are compared with calculations of the differential photoionization cross section for each MO. The computations represent the continuum electron by a plane wave and invoke the frozen-orbital approximation for the remaining electrons. In general, agreement with theory is better at the MgKα energy than at the YMζ energy. In most cases, the calculations predict the correct intensity ordering, but large deviations from the experimental ratios were noted in some cases.

The valence spectrum of molecular oxygen (up to $\sim$ 30 eV binding energy) is discussed. Both the MgKα and YMζ results indicate the presence of the uppermost $^2\Pi_u$ state arising from the O_2^+ configuration ... $(\pi_u)^3(\pi_g)^2$. Its intensity relative to the remaining states of this configuration is in reasonable agreement with theoretical predictions.

I. INTRODUCTION

A photoelectron spectroscopy (photoemission) experiment measures the energy, number and direction of electrons ejected from a sample by monoenergetic photons. The magnesium and aluminum $K\alpha_{1,2}$ x-ray lines (1253.6 eV and 1486.6 eV respectively) have been used extensively in gas-phase studies of this kind. They are easily produced in an x-ray tube, the unresolved $K\alpha_{1,2}$ doublet ($2p_{3/2,1/2} \rightarrow 1s$) having a linewidth of $\sim$ 0.7 eV in magnesium and $\sim$ 0.8 eV in aluminum. This makes them useful for probing the electronic structure of gaseous species. However, since the width of electronic levels accessible with soft x-rays is frequently less than 0.7 eV it is clear that considerable improvement should result from the use of narrower photon sources.

One approach to this problem is monochromatization of the exciting radiation. An instrument capable of studying gases with monochromatized $AlK\alpha_{1,2}$ x-rays has recently been constructed by the Uppsala group.[1] It has an ultimate resolution of 0.22 eV (total contribution to the peak linewidth other than the inherent width of the electronic level).

It is also important to examine the possibility of using emitters other than magnesium or aluminum. In some instances, a higher-energy source is called for to reach the deep lying levels of a system. Thus chromium and copper are used occasionally for this purpose. (The $CrK\alpha_1$ energy is 5414.7 eV[2] and $CuK\alpha_1$ is 8047.8 eV.[2]) Unfortunately, the width of the $K\alpha_1$ line increases with atomic number, resulting in some loss of resolution with these two sources. By the same token, the $K\alpha_{1,2}$ line of sodium (1041.0 eV)[2] should be narrower than the $K\alpha_{1,2}$ x-ray of either magnesium or aluminum. Furthermore, the $2p_{1/2} - 2p_{3/2}$ spin-orbit splitting

should be less, leading to a yet narrower line. Siegbahn et al.[3] used sodium in combined form as an anode material. The peak corresponding to the carbon 1s of graphite was found to have a linewidth of 1.3 eV. Unfortunately, the corresponding linewidth with $MgK\alpha_{1,2}$ or $AlK\alpha_{1,2}$ was not reported, making it difficult to determine the degree of improvement with the sodium source.

Another emitter found suitable for use in XPS is yttrium. The linewidth of the $YM\zeta$ x-ray (M_VN_{III}, 132.3 eV[4]) may be as low as 0.47 eV.[5] The $M\zeta$ x-rays of the neighboring elements zirconium, niobium and molybdenum are also usable, but they are broader than $YM\zeta$.[5]

The question arises as to whether anything can be gained by probing the same level (or levels) with different-energy photons. It is common knowledge among photoelectron spectroscopists that the relative intensities of bands excited with the helium resonance lines (21.21 eV or 40.8 eV) are generally quite different from the relative intensities obtainable with $MgK\alpha_{1,2}$ or $AlK\alpha_{1,2}$. What is of great interest to chemists is that the patterns of intensity change with photon energy can be systematized and used as qualitative criteria for orbital assignment.[6]

The intensity of a photoelectron peak is related to the photoionization cross section, σ, the probability that a photon of energy $\hbar\omega$ will ionize an electron in one second. The XPS measurement can most directly be related to the differential cross section for producing photoelectrons in the solid and $d\Omega$ (see Section III for details), which is given in the dipole approximation by the following:[7]

$$\frac{d\sigma}{d\Omega} = \frac{\pi e^2}{m^2 c\omega} \left| \underset{\sim}{u} \cdot \langle A | \sum_n \underset{\sim}{p}_n | B \rangle \right|^2 \rho(E) \tag{1}$$

Here $\langle A|$ is the initial state, $|B\rangle$ the final state upon ionization, $\underset{\sim}{u}$ is a unit vector in the photon polarization direction, $\underset{\sim}{p}_n$ is the linear momentum operator for the nth electron and $\rho(E)$ is the density of final states with energy near E. For unpolarized radiation and a randomly oriented sample (such as a gas), the expression must be averaged over all directions. The final state $|B\rangle$ contains the continuum electron. Thus in the expression for $\frac{d\sigma}{d\Omega}$, both $|B\rangle$ and $\rho(E)$ depend on the energy of the photon. This makes clear the importance of experimental measurements at different photon energies: a good final-state wavefunction should be able to predict, through Eq. (1), the correct variation of the cross section with excitation energy.

The present work deals with the three x-ray sources magnesium, sodium and yttrium. In Section II.A we briefly describe the Berkeley Iron-Free Spectrometer, the instrument used to make all the measurements reported in this thesis. We next focus on the source housing (x-ray tube and sample chamber), since this is the part most heavily modified in the last four years. Three x-ray tube designs are discussed (Section II.B), corresponding to the three anode materials. We also discuss four different gas cells, including a device for vaporizing solids for study as gases. This is an important accessory to a photoelectron spectrometer, since it greatly expands the range of systems amenable to study by this spectroscopic technique. Some interesting results of high temperature experiments are discussed in Section V.

While the above modifications were specifically intended for the Berkeley Iron-Free Spectrometer, it is nevertheless hoped that many of the design principles expounded in this thesis would be of use to other workers attempting to make similar improvements on their instruments.

The NaKα and YMζ x-rays are discussed in Section IV. The merits of the $NaK\alpha_{1,2}$ line are explored in Section VI by comparing spectra recorded with the new source to previous measurements with $MgK\alpha_{1,2}$ or $AlK\alpha_{1,2}$.

The major part of this thesis deals with molecular orbitals, the binding energy region up to ∿ 50 eV. We examine the cross section variations when the exciting source is changed from magnesium to yttrium. It must be emphasized that only *relative differential* subshell cross sections, $(\frac{d\sigma}{d\Omega})_{90°}$, were measured (electron beam perpendicular to unpolarized photon beam). The reference peak in each case was one of the levels of the system under study. Binding energies are also reported in some cases.

Since only the rare gases have so far been studied with Mζ x-rays,[8-10] we deemed it appropriate to confine ourselves to small systems. The availability of cross section calculations was also a determining factor in the choice of some molecules, for example, the second-row hydrides (Section VIII), carbon monoxide, nitrogen and ethylene (Section IX).

II. INSTRUMENTATION

A. *The Berkeley Iron-Free Spectrometer*

1. General Description

The main components of the instrument are shown in Fig. 1. A (gaseous) sample, typically at a pressure of $\sim$ 100 microns, is irradiated with monoenergetic photons produced in a separately-pumped, hot cathode x-ray tube. Electrons are emitted via the photoelectric effect. Those with a velocity perpendicular to the direction of incident radiation may enter the analyzer through a rectangular slit (0.4" by .010") defining the electron-optical object. The two concentric solenoid coils shown in Fig. 1 create a magnetic field capable of focusing electrons with finite axial and/or radial departure angles from the 50 cm radius optic circle. In order to have this so called double focusing characteristic, the field must vary as $\frac{1}{\sqrt{r}}$ near the optic circle.[11] Another slit (.020" wide) is situated at $\pi\sqrt{2}$ radians from the first in order to admit the deflected electrons for counting by an electron multiplier (Bendix Channeltron). Repeated scanning of up to four kinetic energy regions is controlled by a Digital Equipment Corporation PDP-8 computer interfaced to the spectrometer system.

The resolution of the analyzer is determined by the widths of the two slits, and by the size (and location) of the baffle which selects the solid angle of electrons to be focused. Ideally, the geometry of the baffle should be the same as that of the source and detector slits (rectangular). The actual design, however, was determined empirically to be roughly "S"-shaped, following the contour of the iso-aberration lines. This departure from the theoretical geometry was caused by

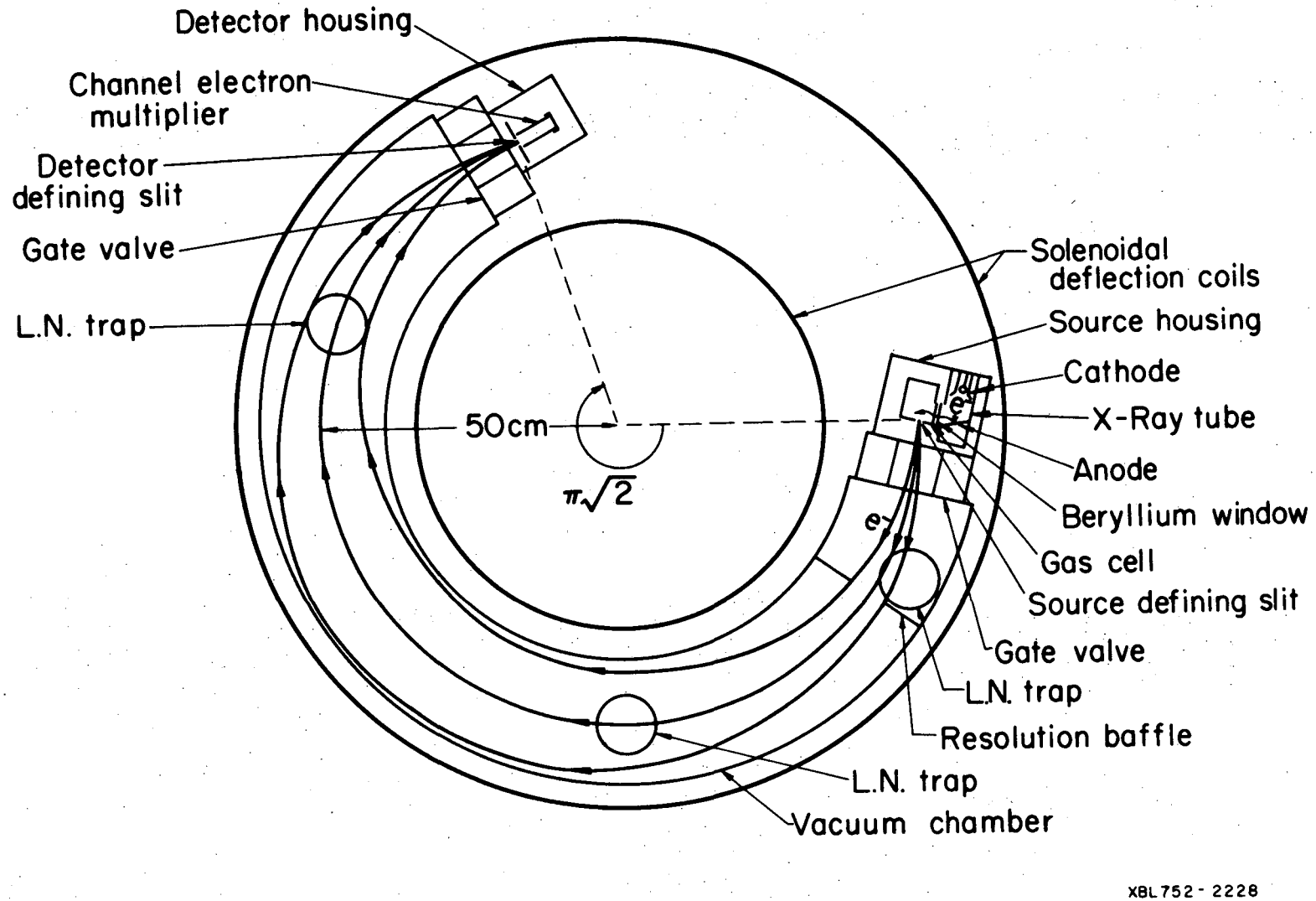

Fig. 1. The Berkeley Iron-Free Photoelectron Spectrometer viewed across the optic circle (mid-plane).

imperfections in analyzer construction and alignment. The energy resolution, $\Delta E/E$, was about .06% for all experiments reported in this work.

Gate-valves are provided in front of both the detector and source housing. This permits disassembling of the two chambers without bringing the analyzer up to atmospheric pressure. A liquid-nitrogen-trapped oil diffusion pump (7" I.D. port, 1520 liters/second of air pumping speed) maintains the latter at a pressure of $\sim 10^{-6}$ torr. To prepare the instrument for studying gases with low energy x-rays, the aluminum baffle plate and gas cell were reconstructed out of gold-plated copper. This eliminated possible charging effects. An important improvement on the existing set-up was the introduction of three liquid-nitrogen-cooled fingers into the analyzer chamber (see Fig. 1). Of course, these were terminated at a safe distance from the electron beam. The traps accomplished two purposes: 1) For condensible gases, both the intensity and peak-to-background ratio improved, sometimes dramatically, due to reduction of electron scattering in the analyzer. 2) They provided protection for the detector from corrosive gases. This made possible the study of a number of reactive species[12] known to be detrimental to detector surfaces. As a consequence, the pressure in the gas cell could now be varied over a wider range than ever before. This is important in the study of energy-loss peaks.

2. Calibration

To calibrate the spectrometer, a direct voltage technique was developed and used by Fadley et al.[13] For gas work, matters are

simplified by the existence of accurate and easily reproducible reference binding energy values.[14] Thus, for a certain sample arrangement, a level of a reference gas (with binding energy E_r) is scanned, using an x-ray of known energy $h\nu$. The coil current I at the peak position is measured accurately. The kinetic energy of the electrons, $(h\nu - E_r)$, corresponds to a certain value of $\beta\rho$, the magnetic rigidity, obtainable from standard tables.[3] In this manner, the spectrometer constant $C = \frac{\beta\rho}{I}$ can be determined. Frequently, a reference gas is bled in simultaneously with the gas under study, and the respective peak currents I_r and I_g are measured. The difference between the two kinetic energies is given by (in the nonrelativistic approximation):

$$\frac{(CI_g)^2}{2m} - \frac{(CI_r)^2}{2m} = \frac{C^2}{2m}(I_g + I_r)(I_g - I_r) \qquad (2)$$

where m is the electronic mass. Thus a linear drift in current δI introduces a correction to the energy difference equal to $2\delta I \frac{C^2}{2m}(I_g - I_r)$. δI can be determined from the known kinetic energy of the reference gas. In this manner, one can obtain absolute binding energies without measuring the current accurately.

3. Field Compensation System

In order to focus 1 keV electrons, a magnetic field of $\sim$ 2 gauss is required. This makes clear the need for eliminating the earth's magnetic field, as well as stray fields. For this purpose two sets of Helmholtz coils (20 ft diameter each) are employed. They provide compensation in the vertical and horizontal (north-south) directions.

In the past, the current in the coils was set prior to switching on the spectrometer magnetic field. Recently, however, large fluctuations in the ambient field (averaging 90 gamma peak-to-peak with a five second fundamental period) led to the development of a dynamic compensating system by Dols, Salz and Sorensen of this laboratory. Details of the design will be discussed in a future publication. Briefly, a magnetic sensor (HP Model 3529A) was placed in the optic plane of the spectrometer, 150 cm away from the center. The sensor comes equipped with an internal coil through which current can be passed. This current is adjusted so as to null the sum of the fields due to the spectrometer coils and to the difference in gain of the vertical Helmholtz system at $r = 0$ and $r = 150$ cm. Any remaining fields can now be compensated for by automatically adjusting the current in the Helmholtz coils. With this system a stability of ± 10 gamma was obtainable.

B. *The Soft X-Ray Tubes*

C. S. Fadley constructed the first x-ray tube for the Berkeley Iron-Free Spectrometer and used it to study solid samples. The essential features of the design were discussed elsewhere.[15] Such an x-ray tube would be unsuited for studying gases because it was not sealed off from the target chamber. This meant that both the anode and filament were exposed to the gas, resulting in anode poisoning and/or short filament lifetime. As a first step in alleviating this problem, Fadley used indium foil to seal the (demountable) anode, window and flange to the x-ray tube can (see Fig. 2 for the relative positions of these parts). A separate pumping system was also used. (Originally, the x-ray and the

rest of the source housing were both pumped by the analyzer diffusion pump.) These modifications made possible a number of studies on gaseous systems.[16] However, the arrangement had a number of drawbacks: 1) Indium foil was awkward to use routinely as a sealant since the gaskets had to be replaced every time the apparatus was disassembled. Furthermore, the foil had to be cut to the right shape to fit the sealing surface. Also, due to warping of the mating surfaces, the sealing was not always perfect. 2) The pumping speed was insufficient to maintain a clean anode for more than a few hours. The window (which was at $\sim$ 100°C during operation) frequently became coated with impurities, resulting in further intensity decrease. This state of affairs rendered the study of low-intensity peaks almost impossible.

Thus, with the stock of simple experiments on non-corrosive gaseous systems largely depleted, there was a pressing need to equip our spectrometer with a stable and sufficiently intense x-ray source. Clearly, there were two minimum requirements: 1) A completely sealed, easily demountable x-ray tube. Demountability is necessary to enable one to use different anode materials (magnesium being the most commonly used), and to replace the window and filament. 2) A pumping system fast enough to maintain a clean anode surface.

1. The X-Ray Tube Pumping System

We address ourselves to the second requirement first. A new pumping system was constructed and used to pump on all the x-ray tubes discussed in this work. Instead of the old liquid nitrogen cryopump, an oil diffusion pump (4" throat, 300 ℓ/sec) with a liquid nitrogen

right-angle trap was employed. Since the oil-heating element as well as the pumping jet were magnetic, the pump was placed approximately eight feet from the analyzer. Four-inch diameter stainless steel tubing (Alloy #304), totaling 9 ft in length, covered the distance up to the spectrometer inner coil. From that point to the x-ray tube, 40 inches of 1½" diameter connectors (knife-edge Varion flanges with copper gaskets) were used. The last 18 inches consisted of a segment of flexible tubing (stainless) with an "O" ring coupling connection to the x-ray tube. The diameter of the connection varied from 3/4" to 1½" depending on the x-ray tube in use. A relative indication of the pressure was obtained, using a glass ion gauge situated at the junction of the 1½" and 4" diameter lines (i.e., ∿ 40 inches from the x-ray tube).

A mechanical pump was connected to both the source housing and x-ray tube. A molecular sieve trap (ULTEK Model 50-009) was installed between the x-ray tube and the roughing pump to prevent back-streaming of oil from the pump into the clean x-ray tube system. To start from atmospheric pressure, the valves separating the source housing and x-ray tube must be open to prevent differential pressure on the x-ray tube window. Even then, the mechanical pump valve has to be opened slowly, since the difference in the conductance of the lines leading to the two chambers is enough to damage some thin windows if the vacuum is applied suddenly. When the pressure reaches the micron range, the diffusion pumps can be opened to the respective systems.

2. The Magnesium/Aluminum X-Ray Tube

(a) Design

The sealing of the x-ray tube was accomplished by D. W. Davis,[17] who modified the existing Fadley design as follows (see Figs. 2 - 4). The cooling block, on which the anode was mounted, was sealed to the stainless steel can by an "O" ring. Viton was used because it is capable of withstanding temperatures of $\sim$ 120°C. The other side of the can was welded to the accompanying flange (Fig. 2). The cathode assembly was still accessible, since it was originally mounted on a "butterfly" flange which was, in turn, "O" ring sealed to the circular flange. The beryllium window was also sealed to the can, a 1/16"-thick copper plate bolting to the x-ray tube being used to press it against a vitron "O" ring. The .0005" thick, 3/4" diameter beryllium disk (Kawecki Berylco Industries, Inc., Hazleton, PA) proved strong enough not to shear or wrinkle under these conditions, and a complete separation of the x-ray tube and gas cell vacua was achieved. (This mode of sealing the window was suggested by Professor D. A. Shirley.) In order to provide good cooling for the anode (1¼" in diameter), the magnesium (or aluminum) was connected to the copper cooling block (water flows continuously through the latter) by six 4-40 Allen-head screws lying on a 1" diameter bolt circle. The beryllium window was cooled somewhat by attaching the copper piece that clamps it in place to the anode-cooling block. The x-ray tube has two pumping ports totaling no more than one square centimeter in cross-sectional area. However, this proved sufficient for days of continuous operation. The pumping lines were welded to a valve, in order to allow for the use of air-sensitive anodes, since the x-ray tube could now be carried over

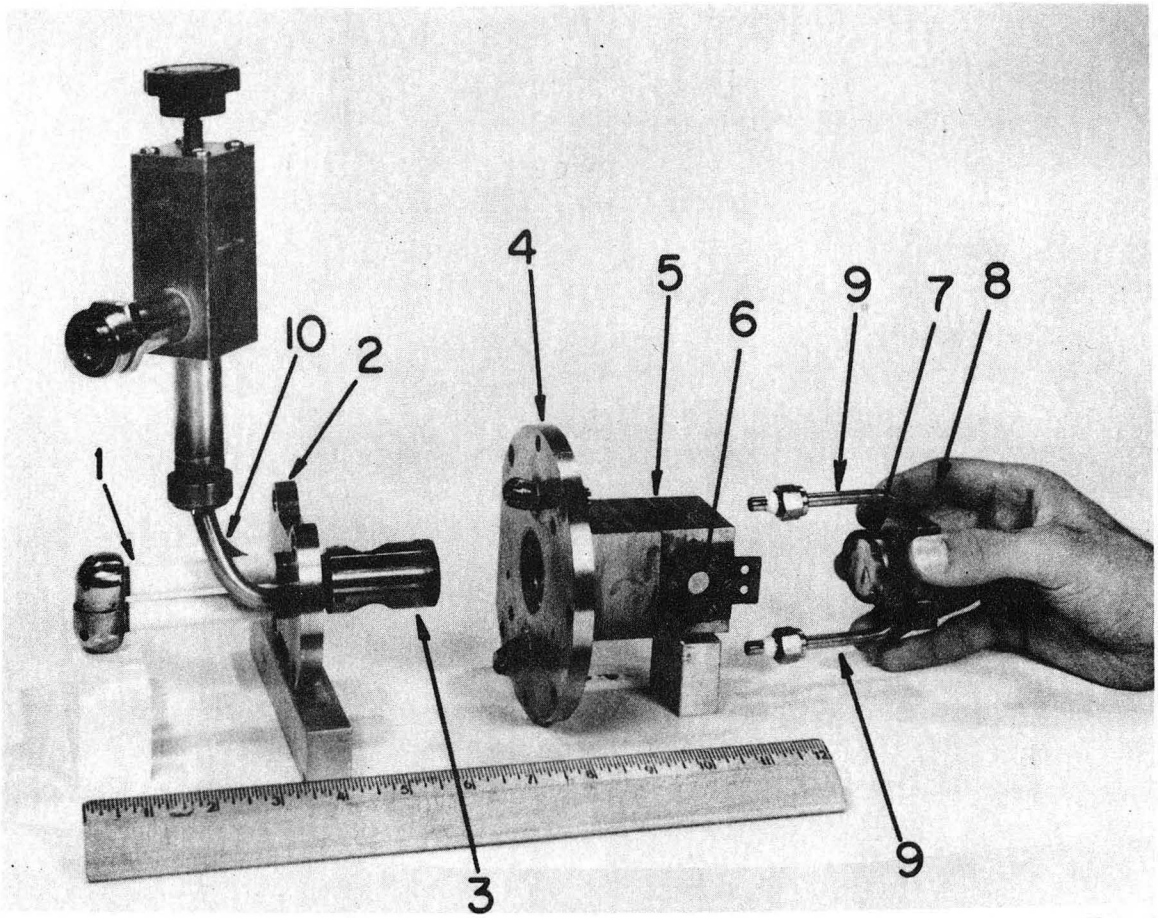

XBB 751-274A

Fig. 2. Exploded view of the magnesium (or aluminum) anode x-ray tube. From left to right: two high-voltage feed-throughs (1) with corona balls are welded to a "butterfly" flange (2). The cylindrical part (3) is the cathode assembly (see Fig. 3 for a closer view). It fits through the opening in the circular flange (4). This flange (stainless steel) is welded to a can (5) on which the (beryllium) window (6) is mounted. The anode (7) is bolted to a cooling copper block (8). The latter is sealed to the can by an "O" ring. The two water lines (9) mate to swage-lok fittings in the circular flange. Water supply and return lines (not shown) are connected to the fittings on the back side of the flange. The inside of the x-ray tube is pumped through two ¼" diameter lines (10). The valve is provided to allow for the use of air-sensitive anodes.

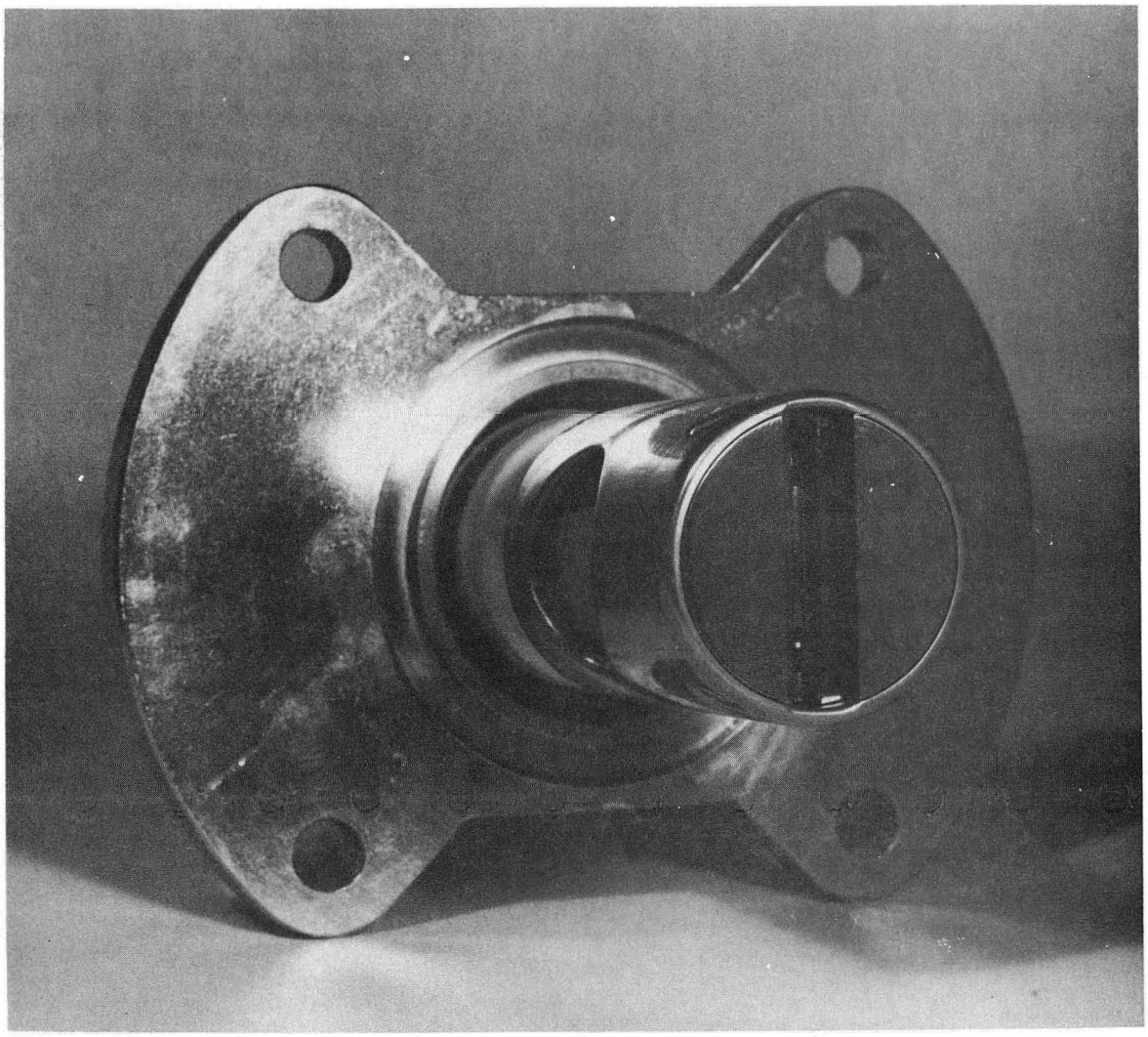

Chem 3998

Fig. 3. The cathode assembly. The filament is made of .005" diameter tantallum wire wound on a .018" diameter mandril (72 turns/inch). An "O" ring groove is machined in the "butterfly" flange for sealing to the x-ray tube. (Photo taken from reference 15.)

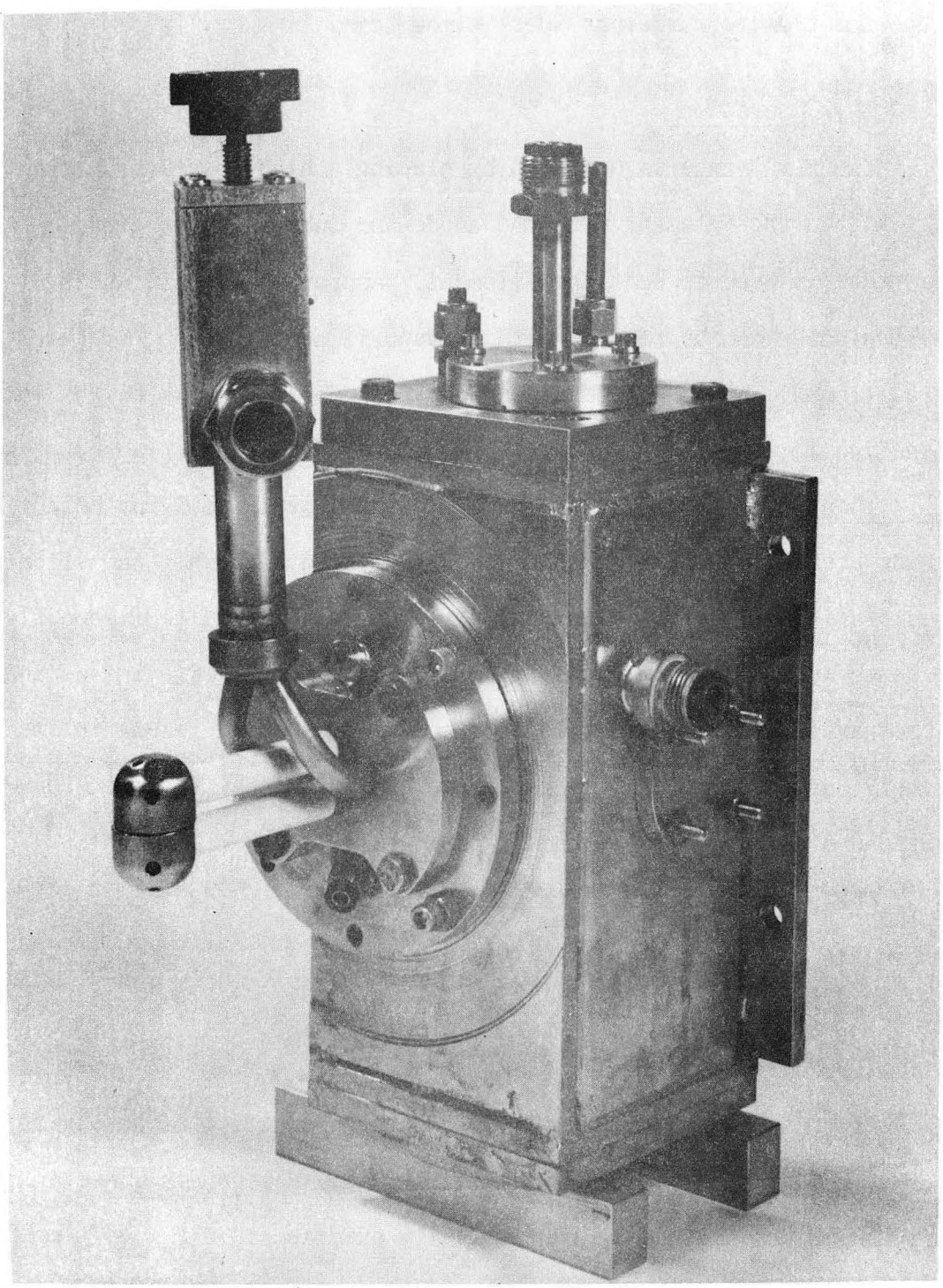

XBB 751-276

Fig. 4. The soft x-ray tube in position in the source housing. (See Fig. 1 for the location with respect to the rest of the spectrometer.)

to the spectrometer under an inert atmosphere.

(b) Operation

The x-ray tube is operated by placing a high negative voltage ($\sim$ 12 kV) on the filament with the anode and tube walls at ground. An ac current is used to heat the filament. Approximately 350 watts of emission power can be reached without vaporizing the anode, provided there is good contact between the anode and cooling block (oxides removed by sanding).

Thanks to the modifications discussed above, the x-ray output now remains steady for days. The anode is recovered with only the slightest discoloration. The filament, which used to burn out quite frequently in the past, now lasts for months. The beryllium window lifetime depends on the gases it is exposed to: some corrosive species result in its untimely destruction. In general, however, the window has been found to withstand a variety of compounds rather well.

The performance of the magnesium and sodium x-ray tubes is compared in part 3.(b) below.

3. The Sodium X-Ray Tube

By this we mean an x-ray tube for the production of NaKα x-rays. This was achieved by modifying the Davis-Fadley design discussed in the previous section. Since sodium is easily oxidized in air, anode mounting should be done in an inert and scrupulously dry atmosphere. This is a rather cumbersome procedure. There is also the problem of cooling the sodium efficiently, all of which leads one to consider alternative ways of making a sodium anode. One possibility might be to use sodium in

combined form where it is less (or not at all) susceptible to corrosion. In order to withstand electron bombardment, however, the compound should be an efficient heat conductor (or have a very high melting point). Thus Siegbahn et al.[18] found that NaCl quickly vaporized when used as an anode material. A further complicating factor in this approach is interference of the x-rays produced by the anion species, though these could conceivably be used to advantage to probe the sample simultaneously with different energy x-rays. In this work, this approach was not followed, however. Instead, the sodium target was produced *in situ* by vaporizing sodium metal onto the anode surface.[19]

(a) Design

A number of modifications were made on the existing x-ray tube to prepare it for a sodium target. At a later date, a separate x-ray tube was constructed exclusively for this purpose. This is shown in Figs. 5 and 6. The new features of the sodium x-ray tube are the following:

1) The pumping port was considerably enlarged. A 1½" diameter "T" with a 1½" port right-angle valve was welded to the butterfly flange. Faster pumping was found to be nonessential to obtaining the sodium line, but it doubtlessly improved the intensity and duration of the x-ray output.

2) Since the spatial extent of the x-ray tube arrangements in the horizontal direction was limited by the presence of the spectrometer coils, smaller high-voltage feedthroughs became necessary. (Ceramaseal, Cat. #808C2824-1, 10 kV rating.)

3) The cathode assembly was simplifed from that used by Fadley.

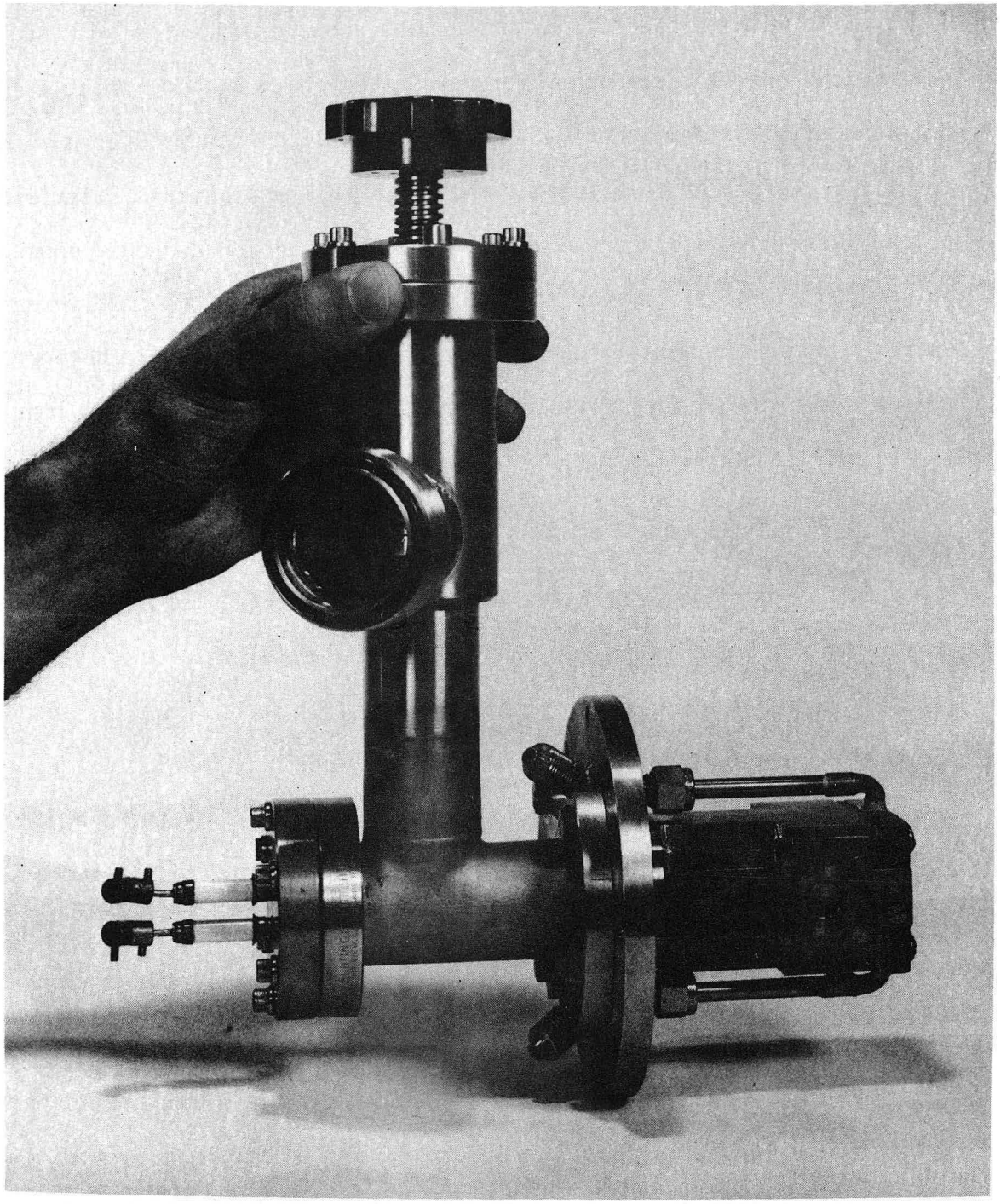

XBB 751-42

Fig. 5. The assembled sodium-anode x-ray tube. Note the large (1½" diameter) pumping port. The cathode assembly is mounted on 2¾" diameter Varian flange (shown in Fig. 6).

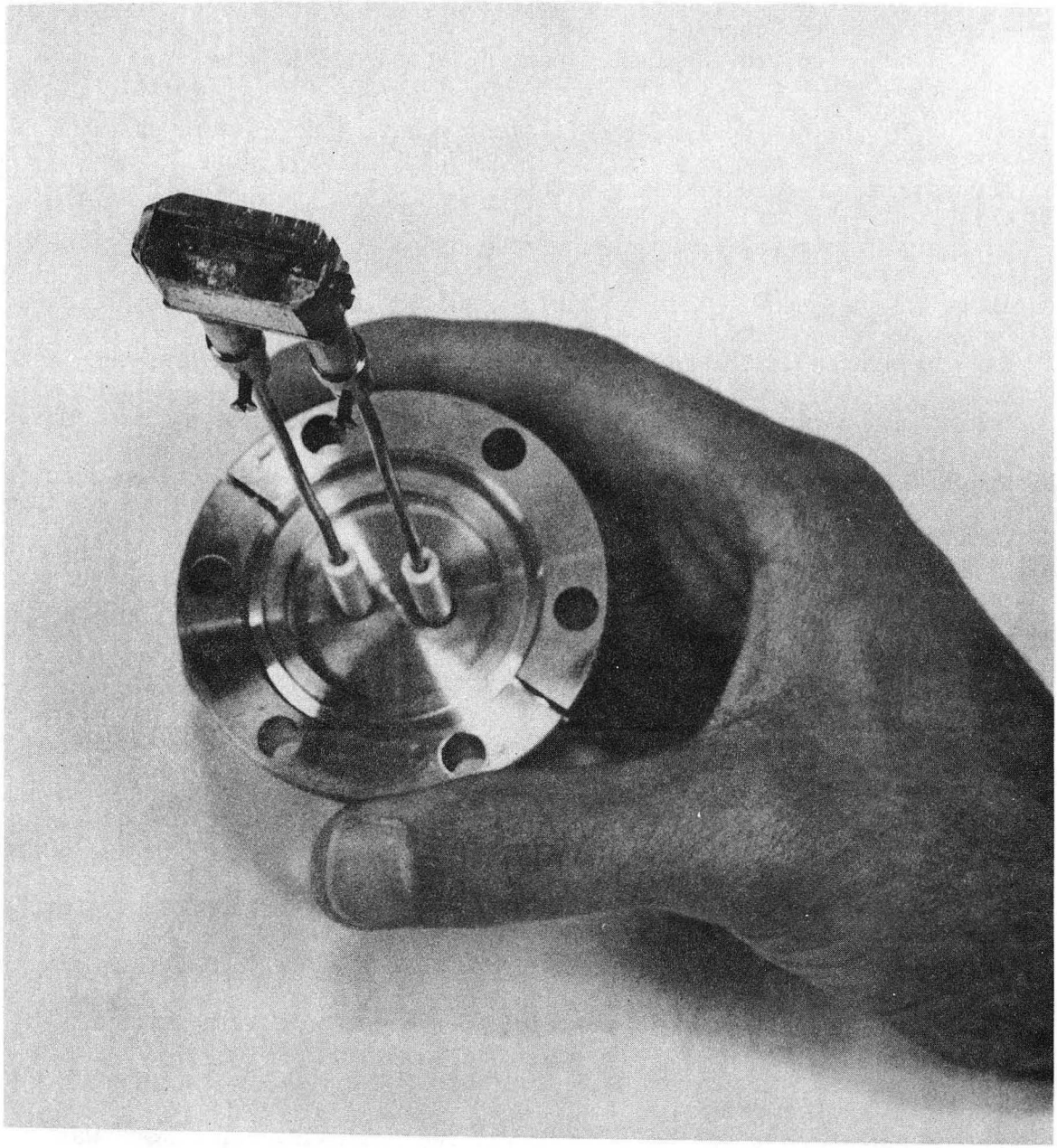

XBB 751-39

Fig. 6. The sodium x-ray tube cathode assembly. (Compare with the old design in Fig. 3.) The two holes in front of the filament are for loading the sodium charge. Note that the filament groove is shallower than in the old design (Fig. 3).

It was mounted on a Varian flange, and was cut into a rectangular shape to provide faster pumping at the anode site.

In the new design, the filament mounting poles were easily accessible, instead of being encased in a cylindrical shield. The filament groove was made shallower in order to diffuse the electron image on the anode. This probably resulted in some intensity loss, since a point source is the most highly desirable image. However, the idea behind it was to reduce overheating of the sodium layer and its subsequent evaporation. Two 1/16" diameter, 1/8" deep holes were drilled into the cathode block for loading the sodium.

(b) Operation and Performance

Sodium metal is cut under heptane and pressed into the two holes in the cathode block. The x-ray tube is then assembled and pumped down. When the filament is heated, the sodium vaporizes and coats the anode surface (copper or gold-plated copper). The sodium oxide formed during handling remains behind, since it would require a higher temperature to sublime.

A rough measurement was made of the photoelectron intensity attainable with the x-ray tube described above. Our point of reference is the MgKα photoelectron intensity. The following experiment was performed: Ne1s was scanned with MgKα, using ∿ 14 kV and 20 mA emission current in the old (small pumping port) x-ray tube. The (relative) pressure of neon in the gas cell was noted. Next, a sodium anode was made in the manner described above and the x-ray tube now operated at ∿ 7 kV and 20 mA. Otherwise, the conditions were the same during both experiments, i.e., the geometry, beryllium window and neon pressure

were not changed. The resulting count rates on the Ne1s peak are plotted against time in Fig. 7. Each experimental point represents the average number of counts per second over a half-hour interval. The peak-to-background ratio was 65.5:1 with magnesium, and 60.5:1 with sodium. The plot shows that the MgKα intensity stays constant essentially indefinitely, while the NaKα intensity drops continuously. The rate of decrease was greatest during the first hour of operation. The FWHM of the Ne1s peak increased by 0.1 - 0.2 eV after the first half-hour or so; thereafter it stayed essentially constant. This was probably due to x-ray line broadening through oxidation of an outer sodium layer. Oxidation was probably also responsible for some of the intensity decrease with time, along with evaporation of sodium off the anode surface.

To convert the photoelectron intensity to x-ray intensity we correct for the spectrometer transmission and for the transmission of beryllium at 1254 and 1041 eV.[20] We also take into account the change in the differential cross section $(\frac{d\sigma}{d\Omega})_{90°}$ of neon 1s with x-ray energy. This has been tabulated by Wuilleumier.[21] In this manner, we arrive at a NaKα/MgKα ratio of 1.0. This value has been corrected for the fact that different x-ray tube powers were used in the two runs. This correction is not precise, since the efficiency of core-hole production in the anode is probably not a simple linear function of exciting electron energy. Another source of error is window coating with sodium and the subsequent oxidation of the latter, which has the effect of reducing the transmission of NaKα, hence lowering the NaKα/MgKα value. Still, the result certainly shows that sodium is a good emitter and is well suited for use in photoelectron spectroscopy. It is also interesting to compare

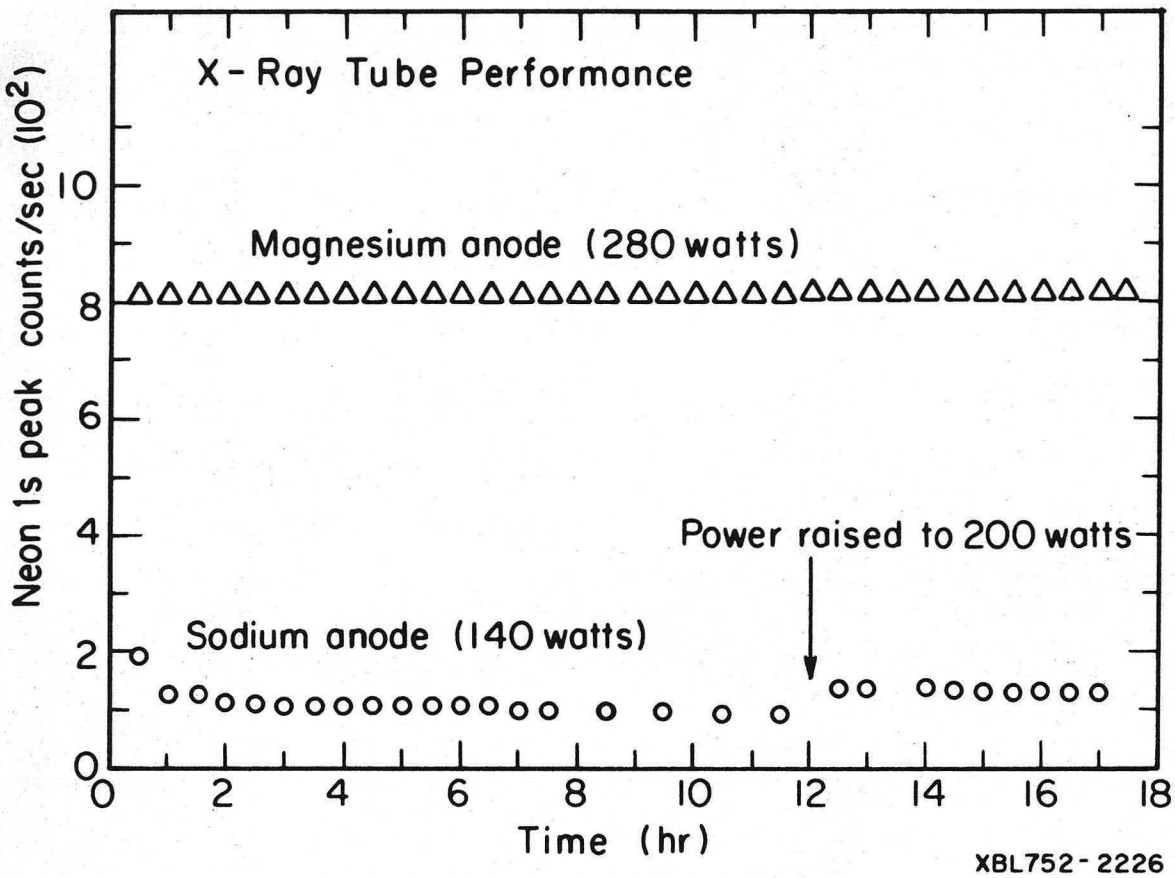

Fig. 7. Ne1s count rate versus time for magnesium and sodium anode sources. The peak-to-background ratio is 65.5:1 and 60.5:1 respectively.

our experimental ratio with theoretical values of the K-fluorescence yield ratio $\omega_{NaK}/\omega_{MgK}$. From the compilation of Bambynek et al.,[22] we quote the results of calculations by three different workers: 0.774, 0.88, and 0.744.

(c) Possible Improvements

As always, the above x-ray tube design can be improved. One highly desirable feature is to have a separate heater for the sodium. The sodium layer on the anode can then be replenished periodically instead of all being deposited in one step. Furthermore, the first evaporation can be used to getter the ambient oxygen. An x-ray tube with this feature has been constructed by Miner.[23] The sodium evaporator in the Miner design has the added feature of collimating the sodium beam, thus preventing it from coating the rest of the x-ray tube. Another possible improvement is the use of a higher transmission window. This point is discussed further in Section C.4 below. Of course, better handling of the sodium charge is also desirable, since it reduces the amount of impurities reaching the anode before the sodium is deposited. Baking the x-ray tube (except for the sodium containing part) may also reduce degradation of the sodium layer. Finally, the question of substrate materials should be examined to determine the surface best able to retain sodium.

C. *The Ultra-Soft X-Ray Tube*

This section deals with the design and construction of an x-ray tube that differs in several important respects from the ones described so far. The significance of the design improvements can be understood best by discussing some of the limitations of the old x-ray tube. We

examine this question next.

1. Motivation

The Davis-Fadley x-ray tube should be capable of accommodating a number of anode materials. Magnesium and aluminum, of course, are used routinely. In addition, copper and chromium anodes (the latter made by plating onto copper) are perfectly feasible. Many other examples can be given. However, a number of interesting x-ray sources are excluded, primarily because the design places rather severe limitations on possible window materials. In order to qualify, a window has to be pin-hole free, since electrons leaving the filament or deflected by the anode would otherwise be capable of penetrating it in large numbers. The result is a high background obscuring the photoelectron signal. Furthermore, an acceptable window should be able to withstand electron bombardment and the resulting high temperatures. Some windows are thin enough to be penetrated by electrons from the x-ray tube. As a result of the harsh operating conditions, even .0001" thick aluminum turns out to be unsatisfactory as a window material.

Faced with these restrictions, and the necessity of using fragile windows to transmit YMζ x-rays (132.3 eV), a new design seemed inevitable.

2. Description of Components

The above considerations led to the x-ray tube shown in Figs. 8 to 15. Also shown are the gas cell and source housing, which were totally rebuilt to conform to the new design. Perhaps the most radical departure from the old design was the "floating" of the anode at a high positive

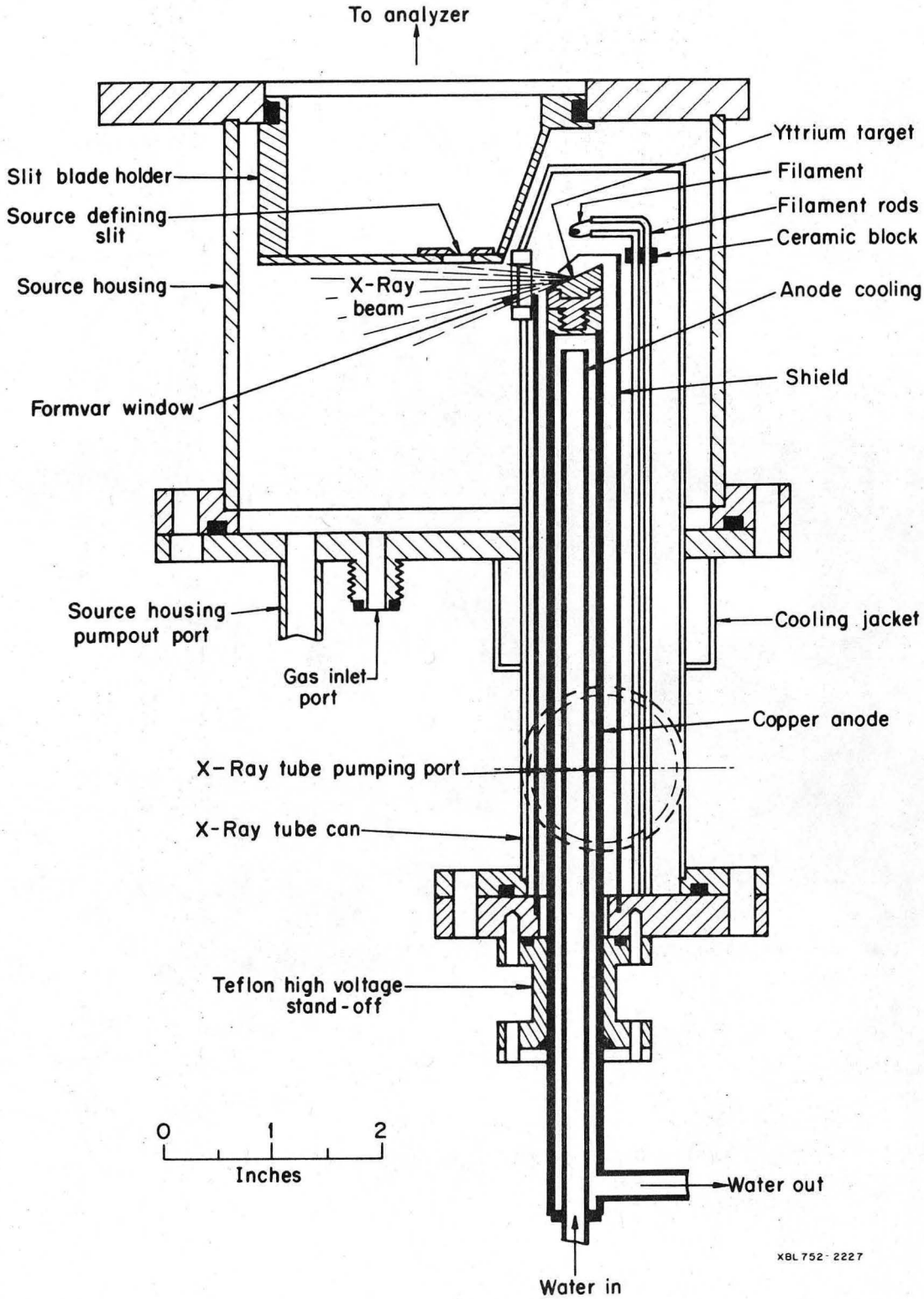

Fig. 8. The ultrasoft x-ray tube and gas cell design.

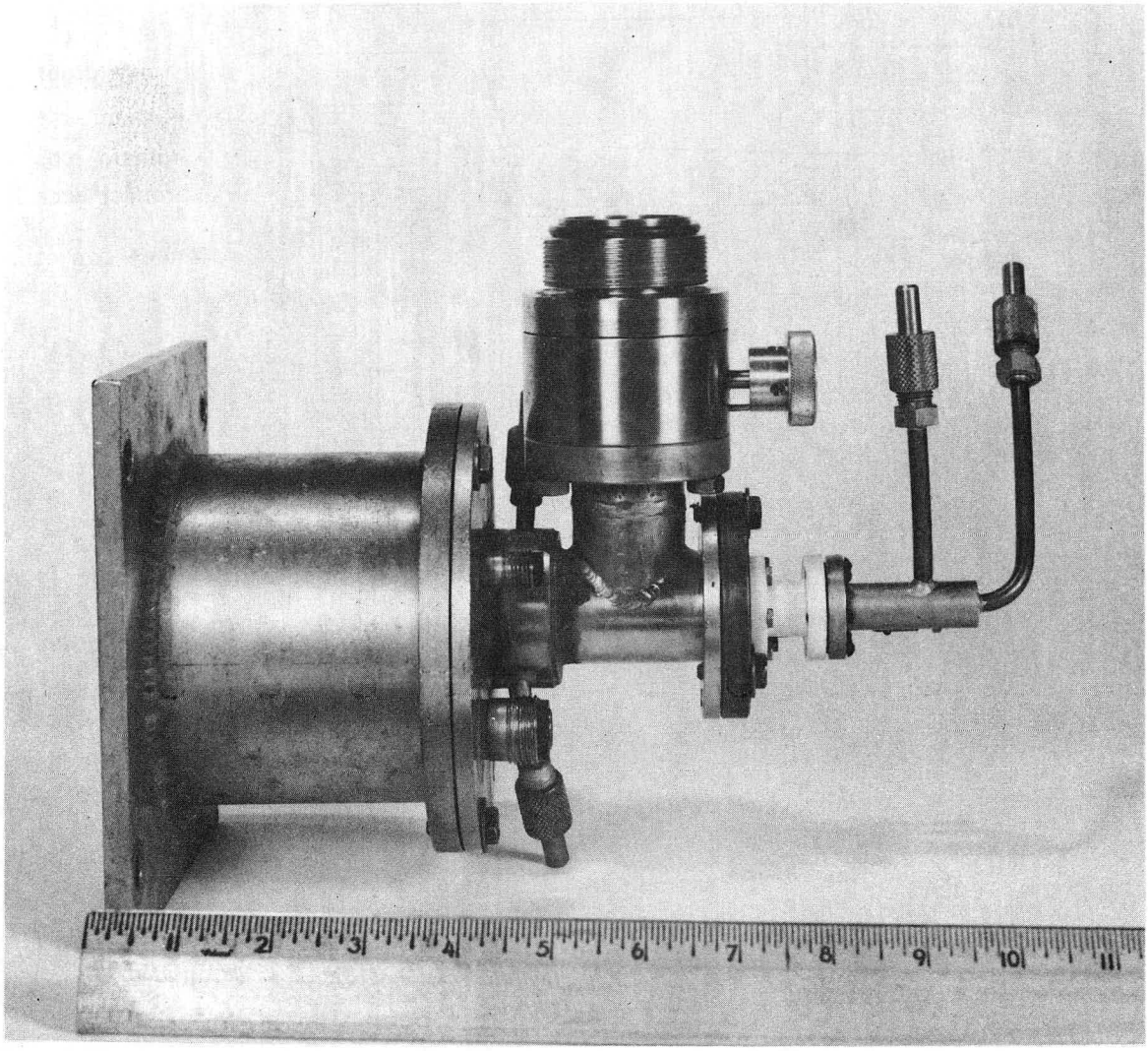

XBB 751-43

Fig. 9. Assembled ultrasoft x-ray tube and source housing.

0 0 0 0 4 2 0 6 0 1 2

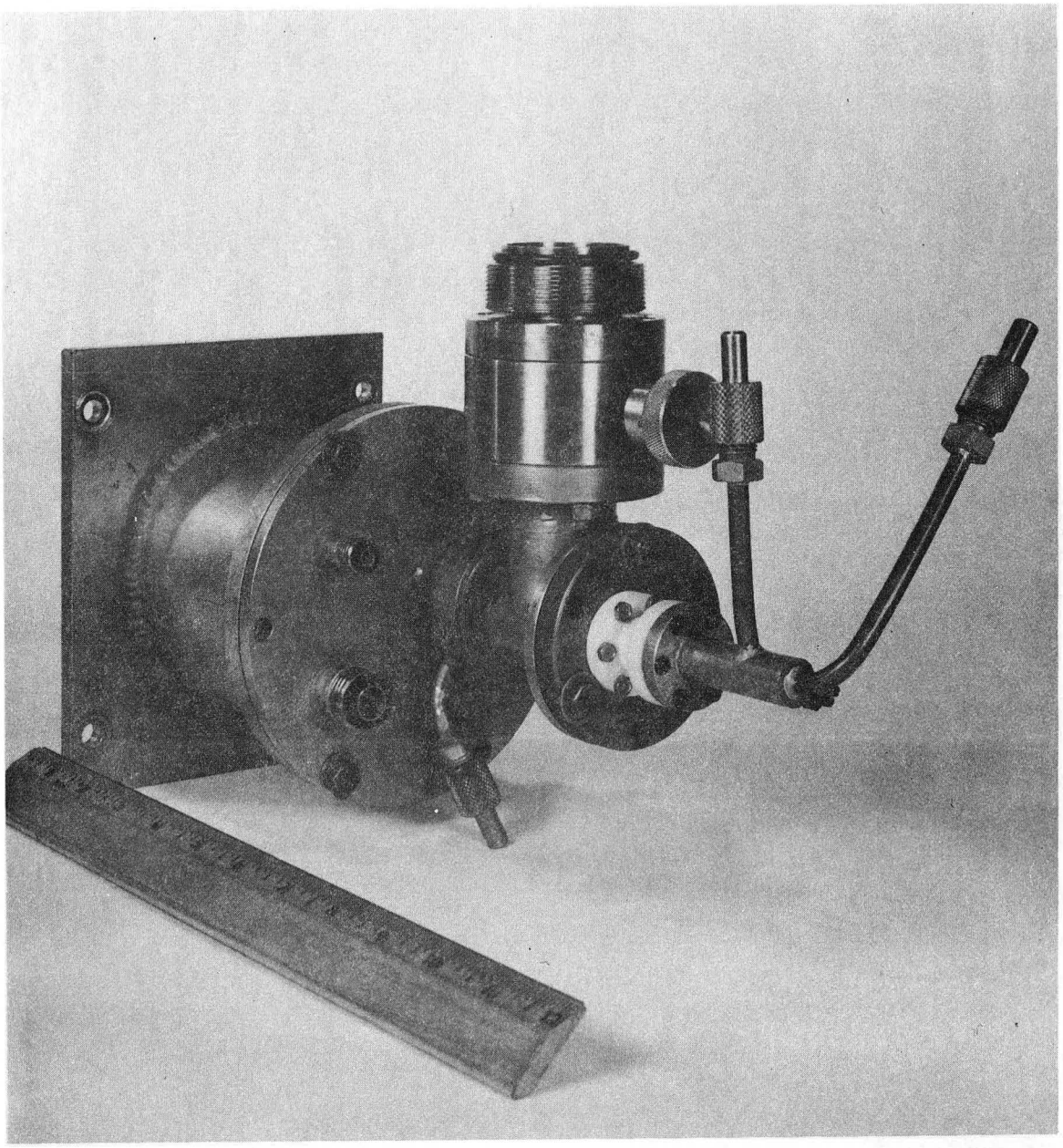

XBB 751-35

Fig. 10. Another view of assembled apparatus.

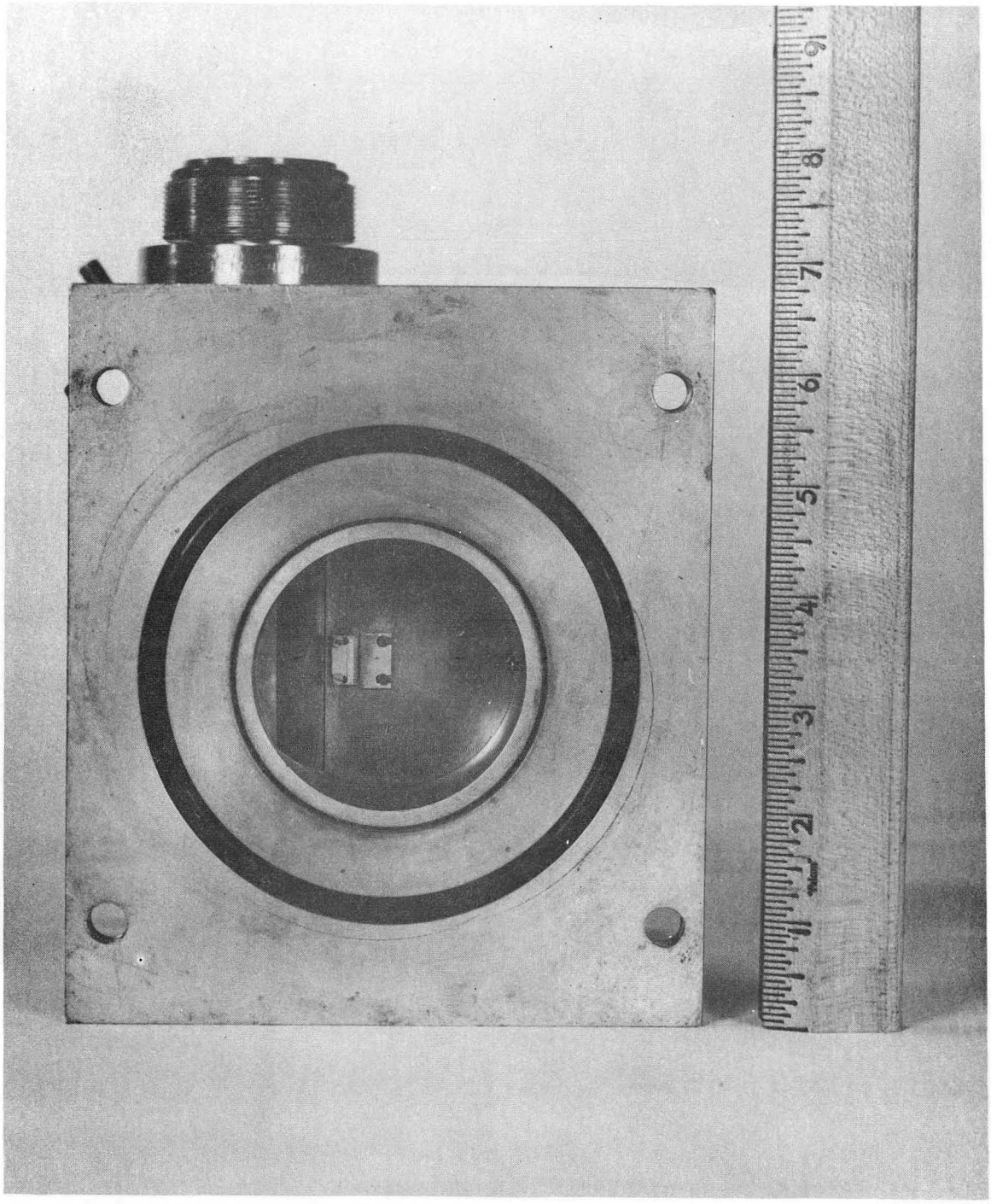

XBB 751-40

Fig. 11. The source housing viewed from the analyzer, showing the slit design. The "O" ring is for sealing to the gate valve (see Fig. 1).

0 0 0 0 4 2 0 6 0 1 3

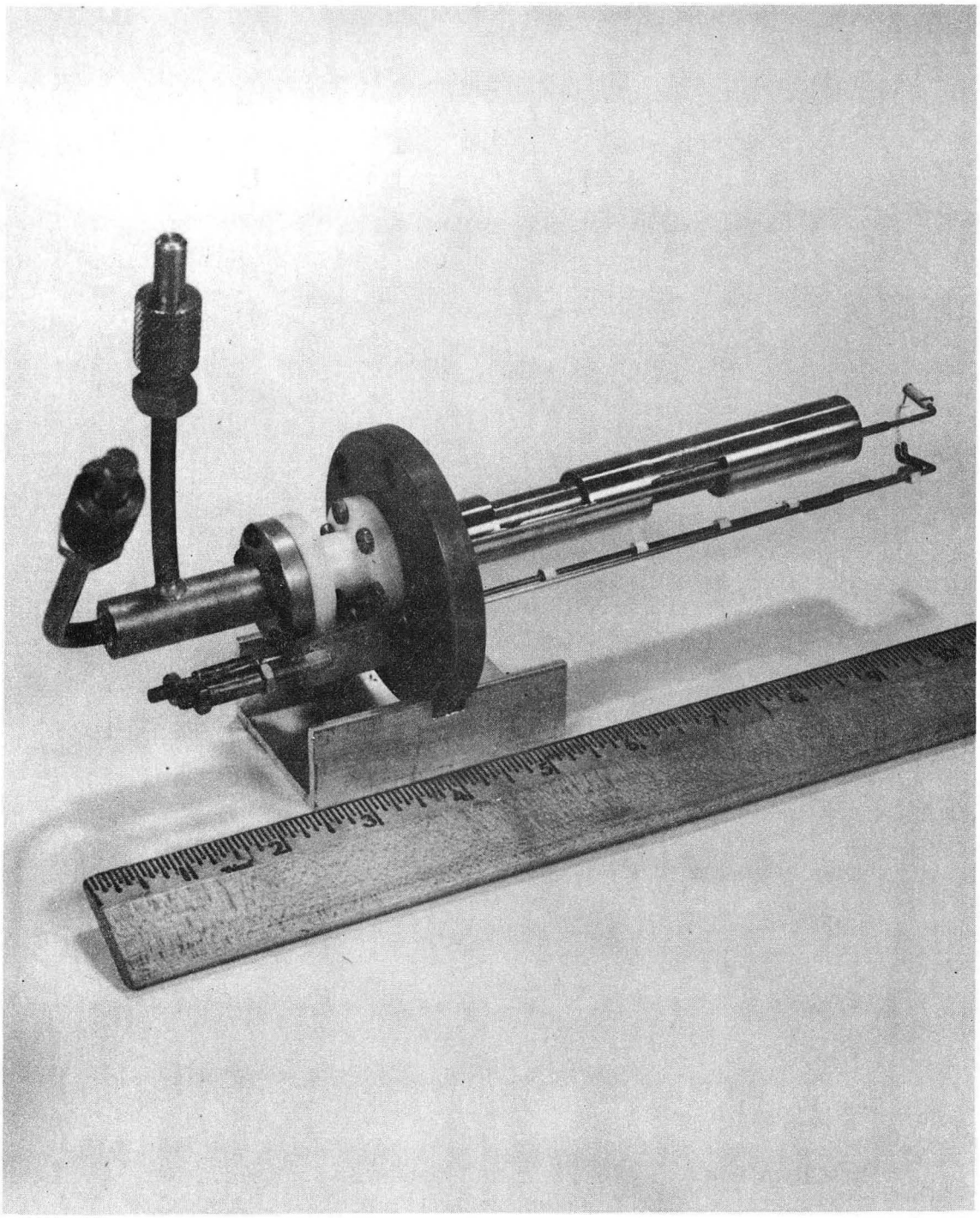

XBB 751-37

Fig. 12. The interior of the x-ray tube. The filament connectors (threaded part on the left) are clearly visible. The anode tubing is covered partially by the shield.

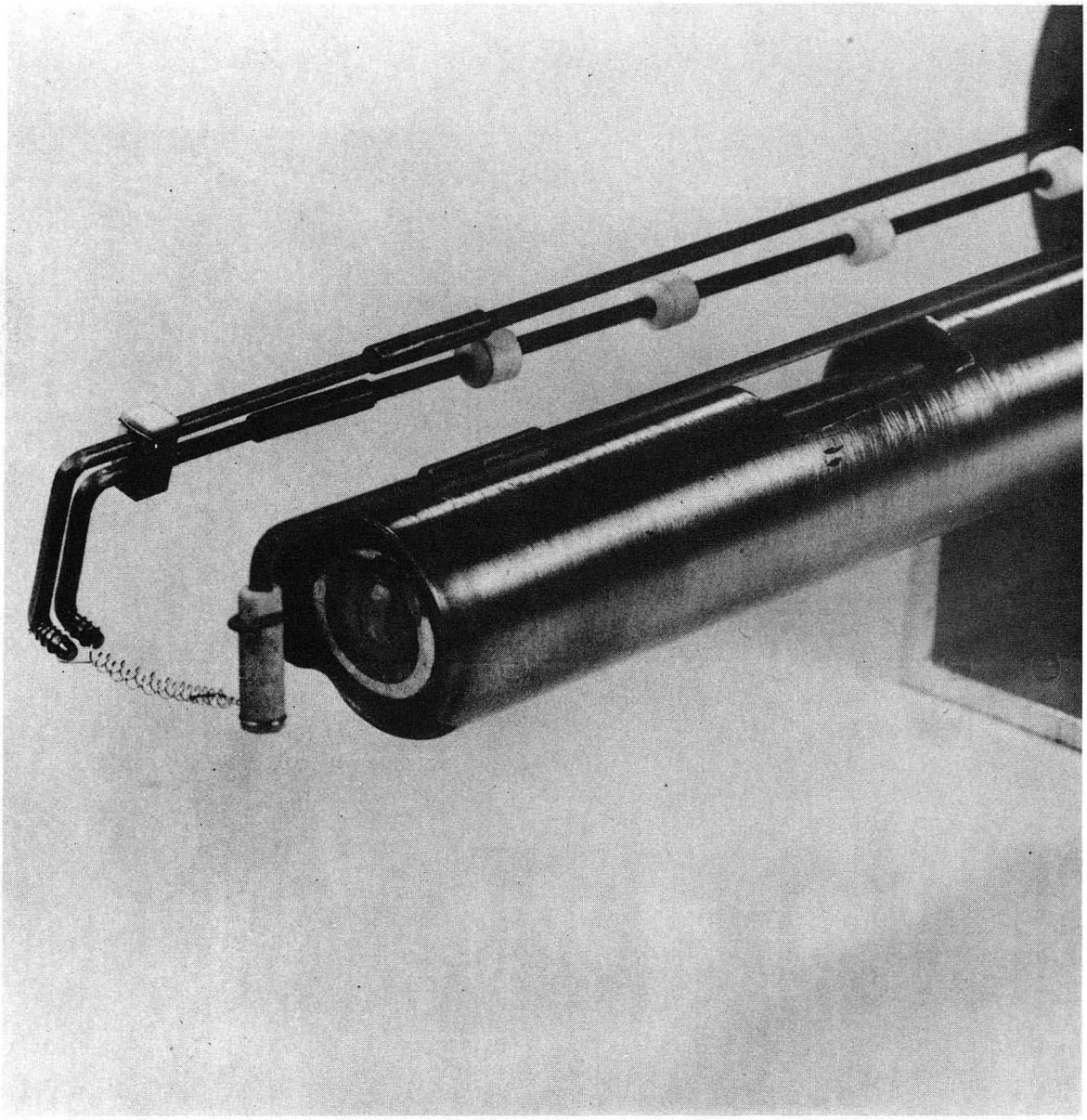

XBB 751-41

Fig. 13. Close view of the filament, anode and shield. Note the bifilar winding of the filament and its insulated support on the right.

0 0 0 0 4 2 0 6 0 1 4

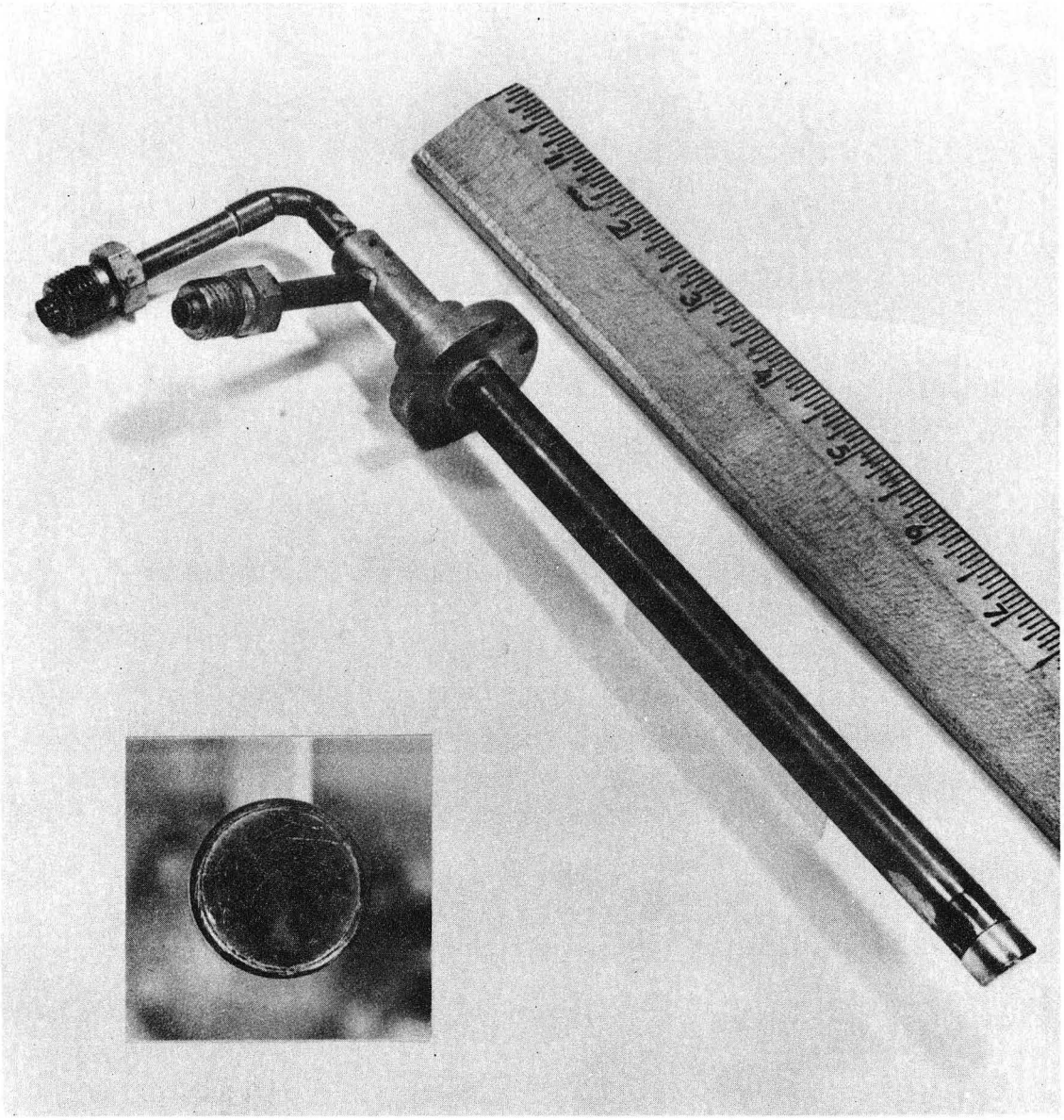

XBB 752-1125

Fig. 14. The anode (½" O.D. copper tubing). The water inlet and outlet connections are also shown. The inset shows the electron image on the anode surface.

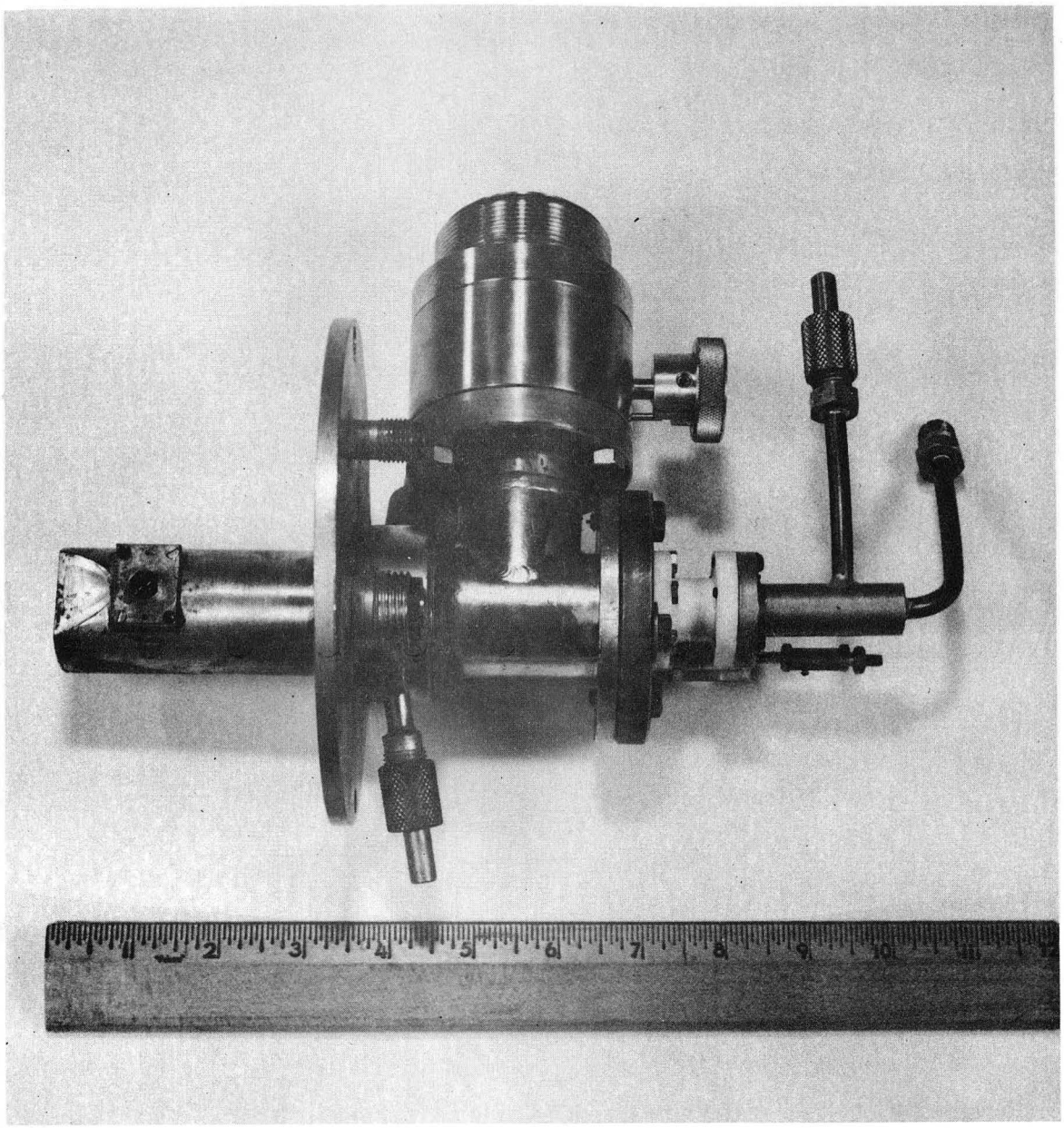

XBB 751-36

Fig. 15. The x-ray tube removed from the rest of the source housing. Note the window on the left.

potential while maintaining the filament at ground potential (although a minor modification should allow one to raise it to any desired *negative* voltage). The x-ray tube can (Fig. 8) was constructed out of 1/16" wall copper tubing so that it could be cooled by water flowing through a jacket approximately 2" from the window. The source housing was made out of 1/8" thick aluminum tubing for lightness, and was gold-plated to prevent charging. It defines the boundaries of the gas cell as well, since to use a separate chamber would have necessitated a second window with added loss of x-ray intensity. The gas cell (or source housing) has a demountable slit-blade holder (see Figs. 11 and 18) fitting into the circular opening on the analyzer side of the source housing and captured in position by an "O" ring, the resulting quasi-seal forming a conductance barrier so the gas can effuse only through the slit. The slit-holder is grounded to the source housing.

The x-ray tube is connected to a 1" diameter "butterfly" valve (see Figs. 9 and 15). This enables the operator to carry it to the spectrometer under an inert atmosphere. "O" rings were used throughout except in connecting the valve to the x-ray tube where a knife-edge (copper gasket) was employed. The major components of the x-ray tube are discussed separately below.

(a) The Cathode Assembly

Both the filament and anode were mounted on the same flange (see Fig. 12). The filament was made from .005" diameter tantalum wire by winding over a 0.040" diameter mandril (40 turns/inch). Since, in this design, the filament is close to the photoelectron source, it was wound bifilarly, and hence, noninductively[24] (see Fig. 13). In this fashion,

both filament terminals are on the same side and can be tack-welded to 1/16" diameter tantalum poles no more than 1/8" apart. The tantalum rods are in turn connected to stainless steel rods of the same diameter (1/16"). One end of the filament is grounded to the supporting flange, which is connected to one of the terminals of the power supply. This method of mounting the filament leaves one of its ends unsupported. Therefore, in order to prevent distortion upon heating, an electrically insulated "hook" was looped around the free end (see Fig. 13).

(b) The Anode

As mentioned earlier, the anode was floated to a positive potential of several kilovolts. A teflon standoff (Fig. 12) was used with "O" ring seals to the anode on one side and the flange on the other. Plastic screws were used to connect the anode, in order to prevent stripping of the teflon threads and/or voltage breakdown. A mylar sheet was inserted between the anode flange and filament feedthrough for the same purpose. The anode (Fig. 14) was water cooled, the water being delivered to the copper backing of the target by 1/4" diameter tubing (see Fig. 8). The house water pressure is 70 psi, probably more than is needed for such a low power x-ray tube. Since filtered tap water was used (as opposed to deionized water), it was necessary to have a long ($\sim$ 20 feet) rubber or tygon cooling line to prevent shorting to ground.

The yttrium target was machined (copious amounts of oil were necessary to prevent it from catching fire) into a disk no more than 1/4" thick and pressed into a copper "cup" of slightly (.001") smaller inside diameter. The other end of the copper cylinder has a screw-thread for connecting to the anode (see Fig. 8). A 10 - 20° x-ray take-off angle

was used. The anode is concentric with a grounded, 3/4" o.d. stainless tube (Figs. 12,13). The latter is necessary to ensure that no electrons can reach the back side of the anode, since x-rays produced there cannot be transmitted through the window.

(c) The Window (Fig. 15)

A number of window materials are available for transmitting in the $YM\zeta$ range.[25] Thus Krause[5] used $\sim$ 20 $\mu gm/cm^2$ polystyrene. Carbon films down to 600 Å or less are also available. We chose Formvar because it adheres to a copper surface better than either polystyrene or carbon, thus forming a better seal. The disadvantage of using Formvar is that it is 15% less transmitting than polystyrene at 132 eV. The windows are prepared as follows: Formvar powder is dissolved in dichloroethylene (20 grs/liter). Microscope slides (3" × 1") are dipped in the solution, then suspended in the dichloroethylene vapors for 1½ minutes to thin out. The film adhering to the slide is dried in air and subsequently floated off over a water surface. Finally, a copper plate (window piece) with a 3/8" diameter opening is used to lift the film out of the water. After drying, a second film can be spread over the first in the same manner. A good separation of the x-ray tube and gas cell vacua is achieved, provided the copper surface is clean and free from scratches. The copper piece was conventionally sealed to the x-ray tube by a Viton "O" ring. Formvar proved capable of withstanding a variety of gaseous species.

When using such fragile windows, it is advisable to have a protection mechanism for the x-ray tube pumping system since a gas pressure of several hundred microns can be present in the gas cell. A convenient protection device in our particular geometry is a miniature

pneumatic valve (Nupro Company, Cleveland, Ohio; Cat. #SS-4BK-NC) placed in series with the gas inlet port. When the window ruptures, the rise in pressure registers on the x-ray tube pumping system ion gauge. The ion gauge power supply was modified so that a pressure rise beyond a set safe limit activates a solenoid valve (as well as an audible alarm). The valve controls the air pressure reaching the pneumatically operated valve at the end of the gas inlet manifold. The result is the interruption of the gas flow into the spectrometer.

3. Operation

The yttrium surface is filed clean inside a nitrogen-filled glove bag. The butterfly valve is then closed and the entire assembly (x-ray tube and source housing) is carried over to the spectrometer. Both the x-ray tube and gas cell are pumped simultaneously to prevent differential pressure on the window. At a pressure of $\sim$ 100 microns the pumping system described in Section B.1 is opened to the x-ray tube. After about two hours (when the x-ray tube pressure reaches the 10^{-7} range) the filament and anode voltages are turned up slowly. A dc current of $\sim$ 2 A is needed to obtain $\sim$ 20 mA of emission current from the filament. No systematic study was made of power versus intensity; however, a few observations are worth noting. At +4.5 kV anode voltage and 16 mA emission current the Ne2p peak quickly broadens to $\sim$ 2 eV FWHM (Krause reported 0.6 eV with YMζ for the same peak.[5]) This is probably due to oxide build-up over the yttrium surface. When the voltage is increased to 5.5 kV, both the intensity and line width improve dramatically. The explanation probably lies in the fact that more energetic electrons

sample more of the bulk yttrium and less of the surface. However, even at 5.5 kV the 0.6 eV Ne2p linewidth was rarely achieved. Electron bombardment may be responsible for the creation of reactive ions. Thus a bakeable x-ray tube would be highly desirable in order to eliminate ambient impurities. Interestingly, when the yttrium is heated to the point of evaporation, a fresh layer is exposed resulting in excellent intensity and resolution. Unfortunately, this is detrimental to the window and hence was not done routinely. The electron beam is very well collimated by the bias tube resulting in an electron image on the anode *perpendicular* to the filament direction (see Fig. 14).

Most windows lasted anywhere from 24 hours to several days. The lower part of the 3/8" diameter x-ray port was masked off to prevent direct irradiation by the filament. A grounded mesh was placed over, but not touching, the outer (gas side) surface of the Formvar. This was necessary to prevent charging of the Formvar layer. Instead of narrow peaks, only a band several electron volts wide is obtained without the mesh.

Essentially constant intensity and linewidth can be maintained for days when the anode voltage is +5.5 kV or above. The emission current was never allowed to exceed 20 mA. Scanning times of 24 hours or more were sometimes necessary for an entire molecular orbital region (up to $\sim$ 50 eV binding energy).

4. Advantages

Although the above x-ray tube has so far only been used with an yttrium target, it is important to emphasize its flexibility as to

permissible anode sources. The electrostatic field lines resulting from a positive bias on the anode are such that the electrons are repelled by the x-ray tube walls instead of being attracted by them as in the old design. It is therefore no surprise that when the x-ray tube is operated without a window (such an arrangement would be feasible for studying solids) no electrons can be detected by the electron multiplier in the analyzer. Cooling of the x-ray tube walls is another factor in ensuring a reasonable lifetime for fragile windows. Altogether, these modifications should allow for a number of different anode-window combinations. For example, polypropylene trimmed down to 1 μ[26] can be used with a magnesium or aluminum anode, yielding ∿ 80% transmission of AlKα x-rays. An added intensity gain should result from the shorter distance of anode-to-gas-target (∿ 1" compared to > 1½" in the old design).

Possible improvements in the design of ultrasoft x-ray sources were cited by Krause.[5] For example, a hidden filament geometry (no direct line-of-sight between anode and filament) would be desirable, since it prevents evaporation of impurities from the hot filament onto the anode surface. This so-called Henke design can be incorporated in the present x-ray tube by placing the filament behind the bias tube instead of above it. This would probably result in a space-charge-limited power output, a problem that can be overcome by raising the filament to a negative potential of several hundred volts.

D. *Gaseous Sample Arrangements*

The sample chambers discussed in this section are all compatible with the old (magnesium) x-ray tube source housing (shown most clearly

in Fig. 4), but not the yttrium source design. The gas sample arrangement for the latter was discussed in the previous section. Here we describe four sample holders: 1) the old (Fadley) design, 2) a new room temperature arrangement, 3) two high-temperature gas cells. The first is designed for pyrolyzing a gas into another gas, the second is capable of vaporizing solids as well as heating gases.

1. The Old Room Temperature Gas Cell

This is discussed in Fadley's thesis[15] from which Fig. 16 is taken. It was rebuilt out of gold-plated copper to prevent possible charging in aluminum, although none had been observed in the past. The gas is bled continuously and randomizes inside a box with a rectangular 0.4" by .010" slit and a window facing the x-ray tube. The assembled gas cell and x-ray tube are viewed from the analyzer side in Fig. 17.

2. The New Room Temperature Gas Cell

One disadvantage of the old gas cell is the necessity of having a window to prevent excessive gas losses. Fortunately, the window does not need to be as durable as the one on the x-ray tube since it is not subject to the same harsh conditions of high temperature and electron bombardment. Thus B. E. Mills found that 20 $\mu gm/cm^2$-thick Formvar can be used (these films are essentially 100% transmitting at MgKα and AlKα energies). However, even with no gas inside the cell, background counts can still be obtained. Their origin is probably either the outer wall of the gas cell facing the x-ray tube and subject to irradiation, or the gas cell window itself. This problem was overcome in a new design, similar to the

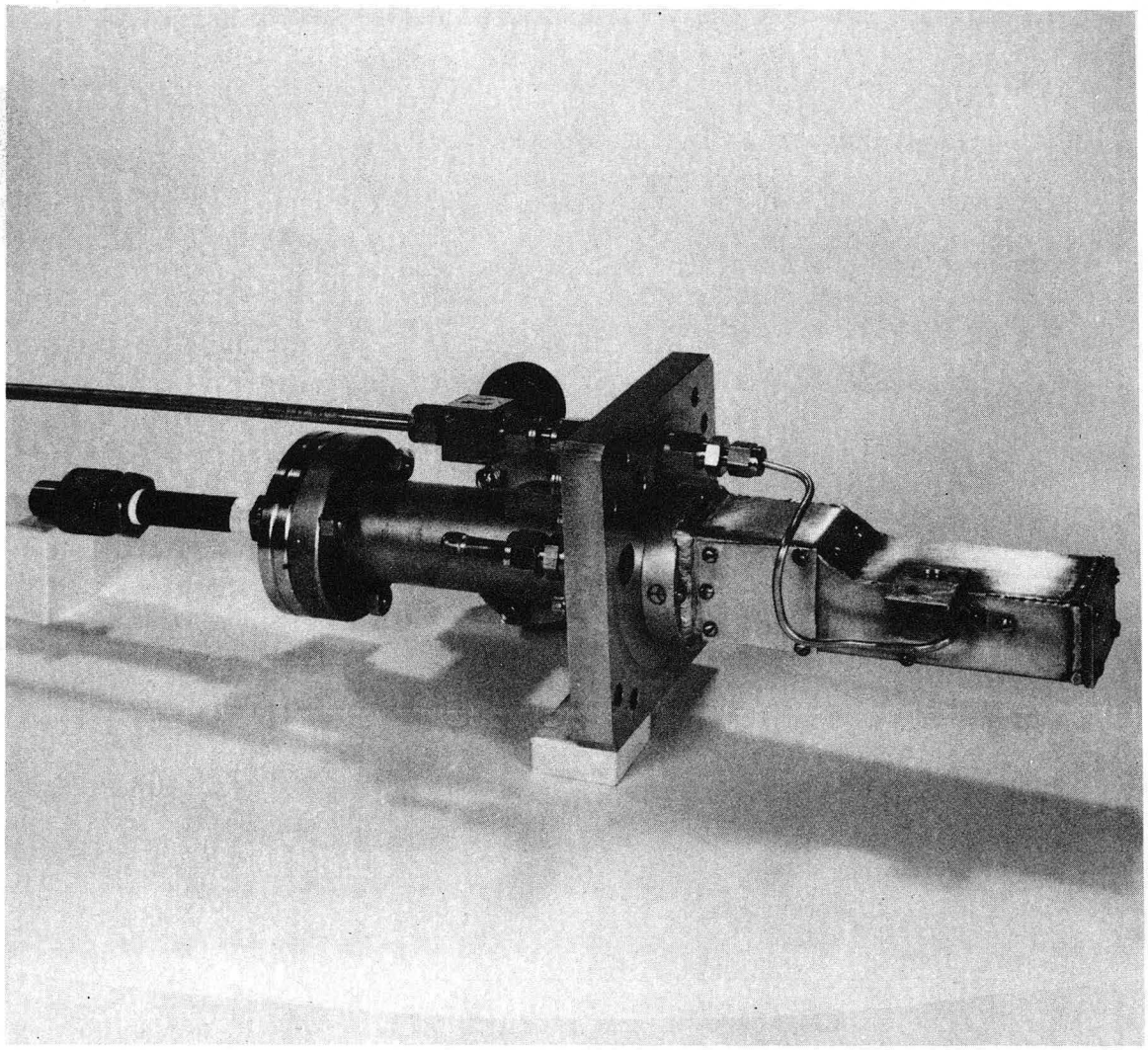

XBB 702-839

Fig. 16. The old room temperature gas cell.

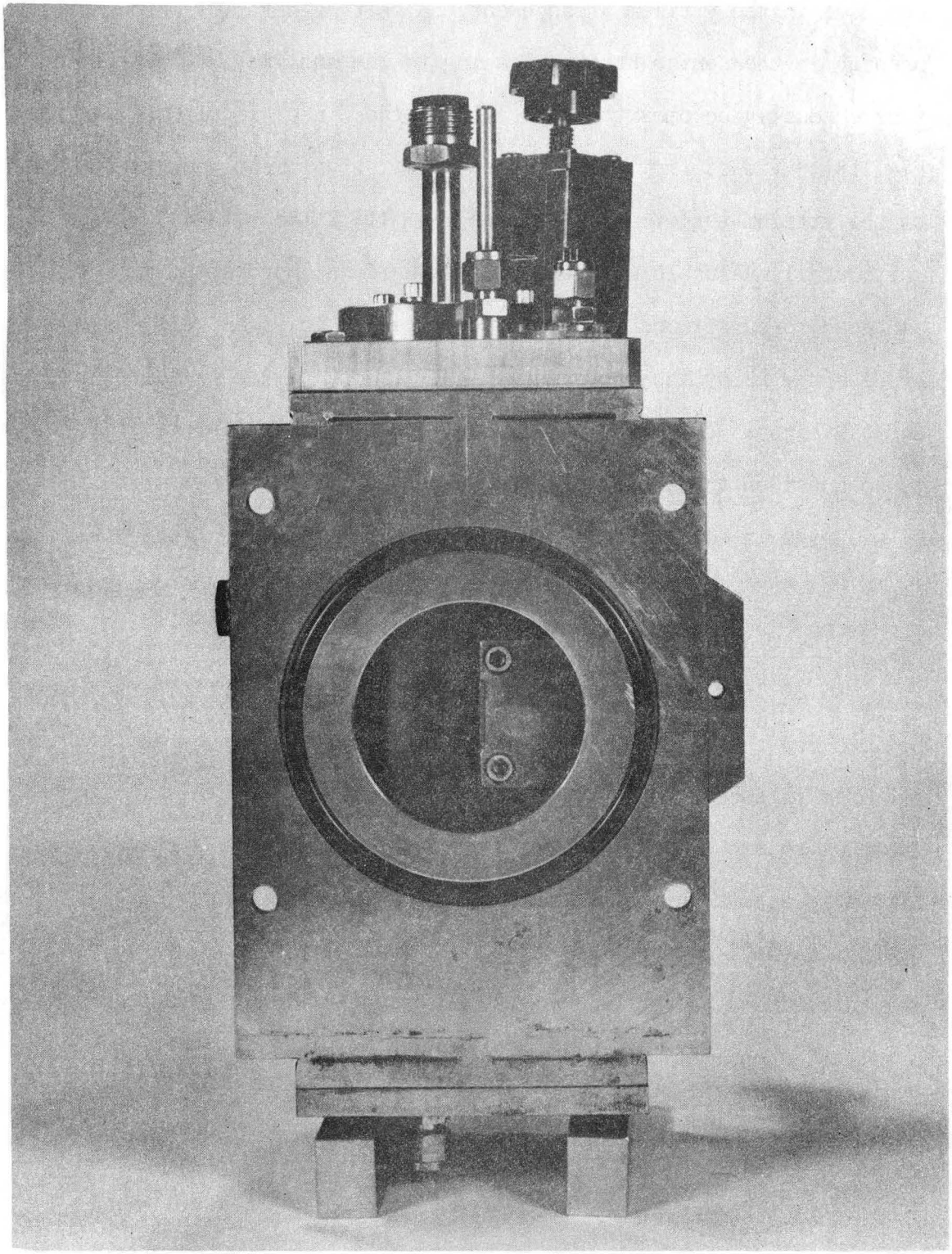

XBB751-275

Fig. 17. The magnesium x-ray tube (right) and old gas cell (left) viewed from the analyzer.

one used in the yttrium arrangement. A slit holder fits into the circular opening in the source housing leading to the analyzer. Thus the whole source housing becomes the gas cell and the window is eliminated (see Fig. 18). Viewed from the analyzer, this arrangement looks very similar to the yttrium target assembly (see Fig. 11). The new gas cell is particularly valuable with weak peaks where an improvement in intensity and peak-to-background ratio can be crucial. This gas cell, however, exposes the x-ray tube to a much higher ($\sim$ 100 μ) gas pressure than before. Corrosive gases can thus conceivably reduce window lifetime. Still, there is no question that, overall, the new design is far superior to the old. It was used in all the sodium experiments described in this work.

3. The Old Heated Gas Cell

C. S. Fadley et al.[15] were the first to construct high temperature devices for the Berkeley Spectrometer. For example, they built an oven and used it successfully to vaporize europium and ytterbium. The basic idea was to employ non-inductively wound tantalum wire encased in boron nitride plates to heat the solid sample. The same manner of heating was used by Davis[17] in another heated cell design. This is shown in Fig. 19. The intent here was to heat a gas and dissociate it before reaching the irradiation chamber. To achieve this the gas was first passed through a preheater compartment. Heating plates were bolted onto the outer walls of the (stainless steel) container. They are not shown in the figure.

4. The New Heated Gas Cell

The flat boron nitride heaters are expensive to make and awkward to use because of their fragility. Furthermore, part of the heating

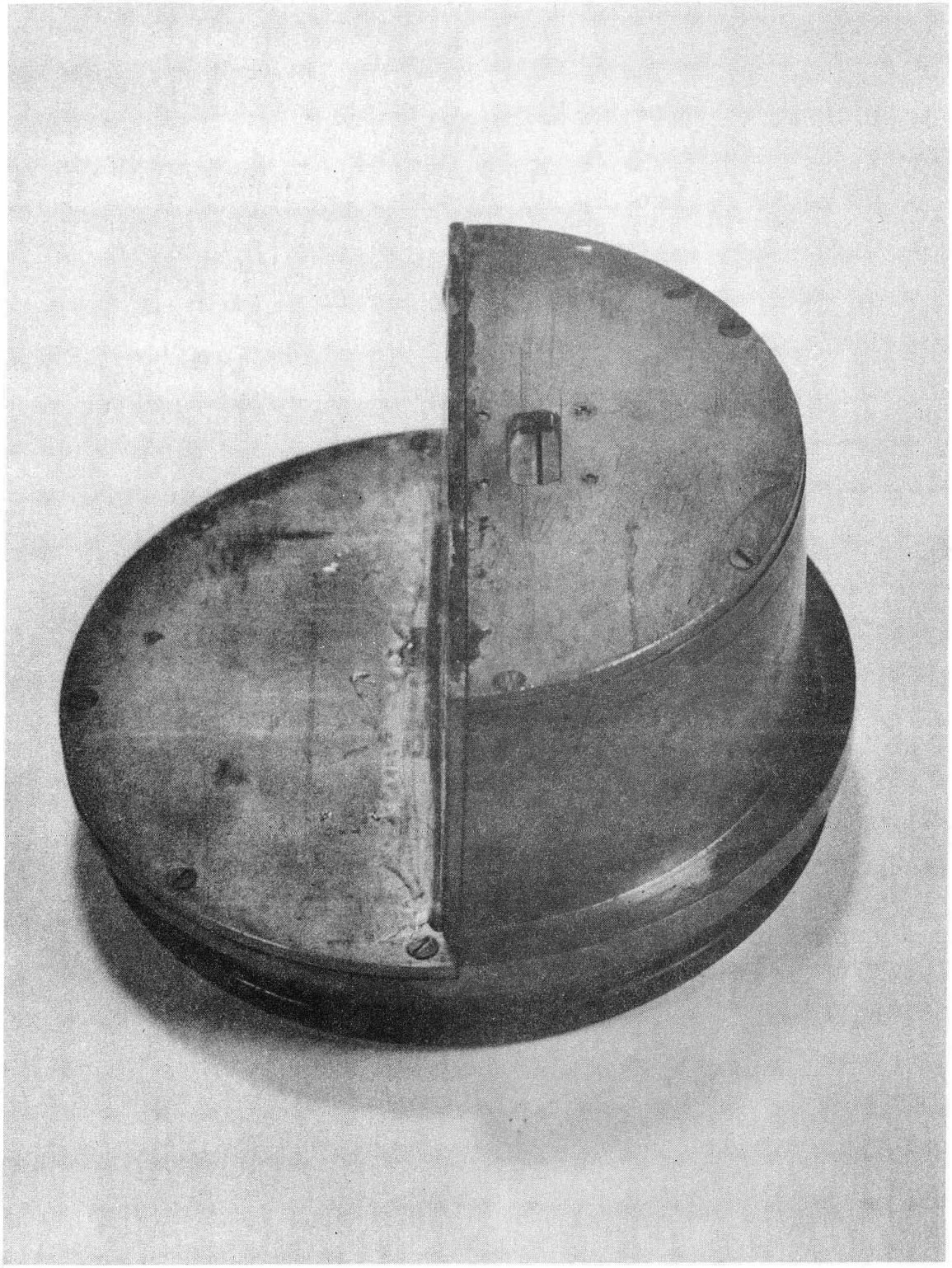

XBB 751-46

Fig. 18. The new slit-blade holder, very similar in appearance to the corresponding part in the ultrasoft x-ray tube assembly (Fig. 11). Note "O" ring on the lower side for sealing the gas target chamber.

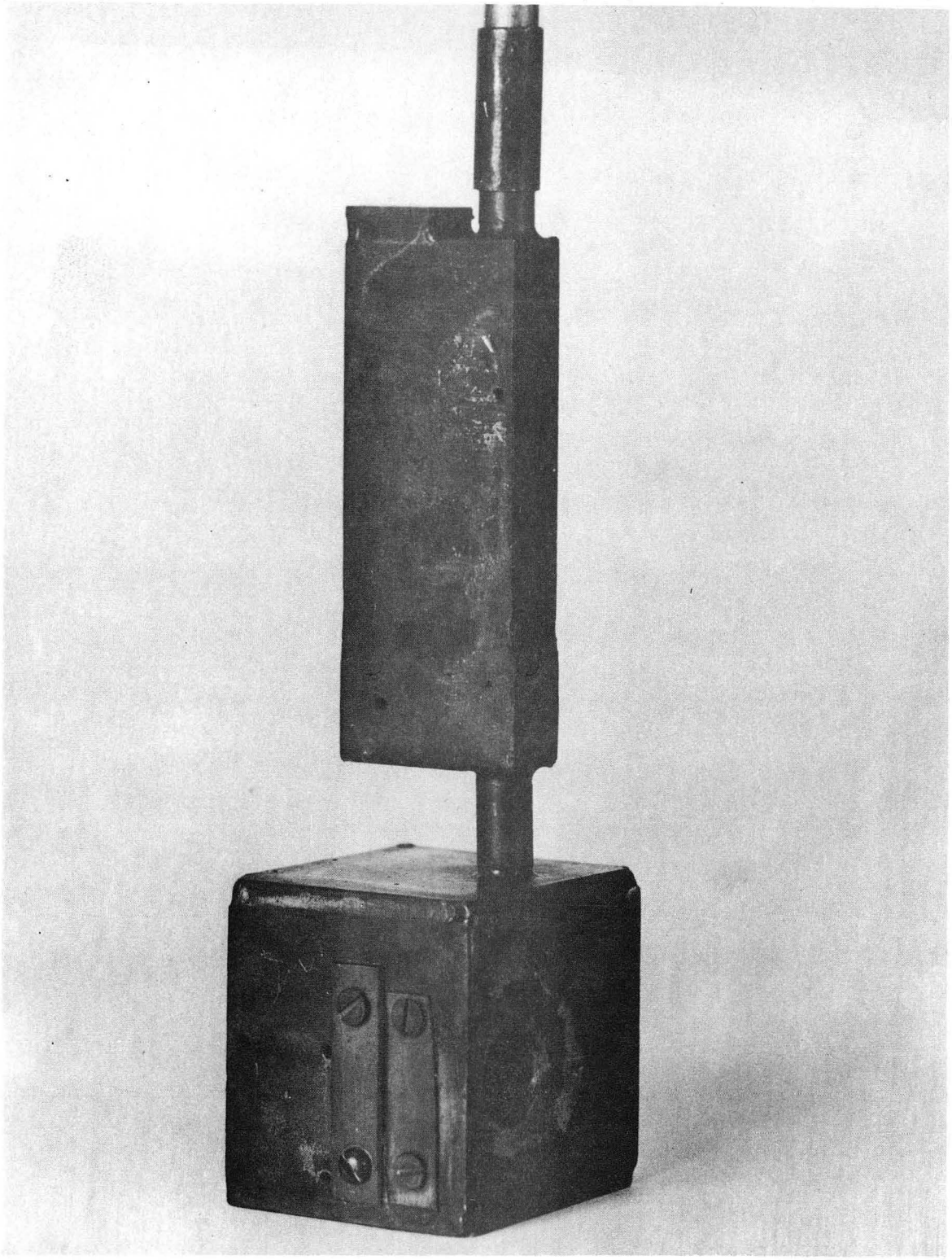

XBB 751-45

Fig. 19. The heated gas cell designed by D. W. Davis. Gas is admitted from the top and heated inside the upper portion prior to reaching the target chamber (lower box). The circular opening is covered by a beryllium window during operation. The heating plates are not shown.

element is invariably exposed to the gas resulting in quick deterioration. The new design, shown in Fig. 20, obviates these problems. In this case, the heater is a ceramic cylinder with an outside thread. Platinum wire is wound bifilarly into the thread grooves. The heater slips around copper tubing through which gas can be passed, resting on the upper wall of the gas box. The latter is welded to the copper tubing and to thin (.020" wall) stainless tubing, which in turn is silver-soldered to the mounting flange. In this fashion the gas cell can be heated by conduction from outside the vacuum, the stainless tubing providing thermal insulation from heat sinks. The brass supporting flange is water cooled to prevent damaging the "O" ring seal to the source housing. The heater can operate continuously in air for a long time. The bottom of the gas cell is demountable for loading solid samples to be heated. Thus this device is capable of heating a gas or a solid. By filling the heater compartment with the appropriate bath, it can even be used as a *cooled* gas cell. Examples of species studied at high temperatures are given in Section V.

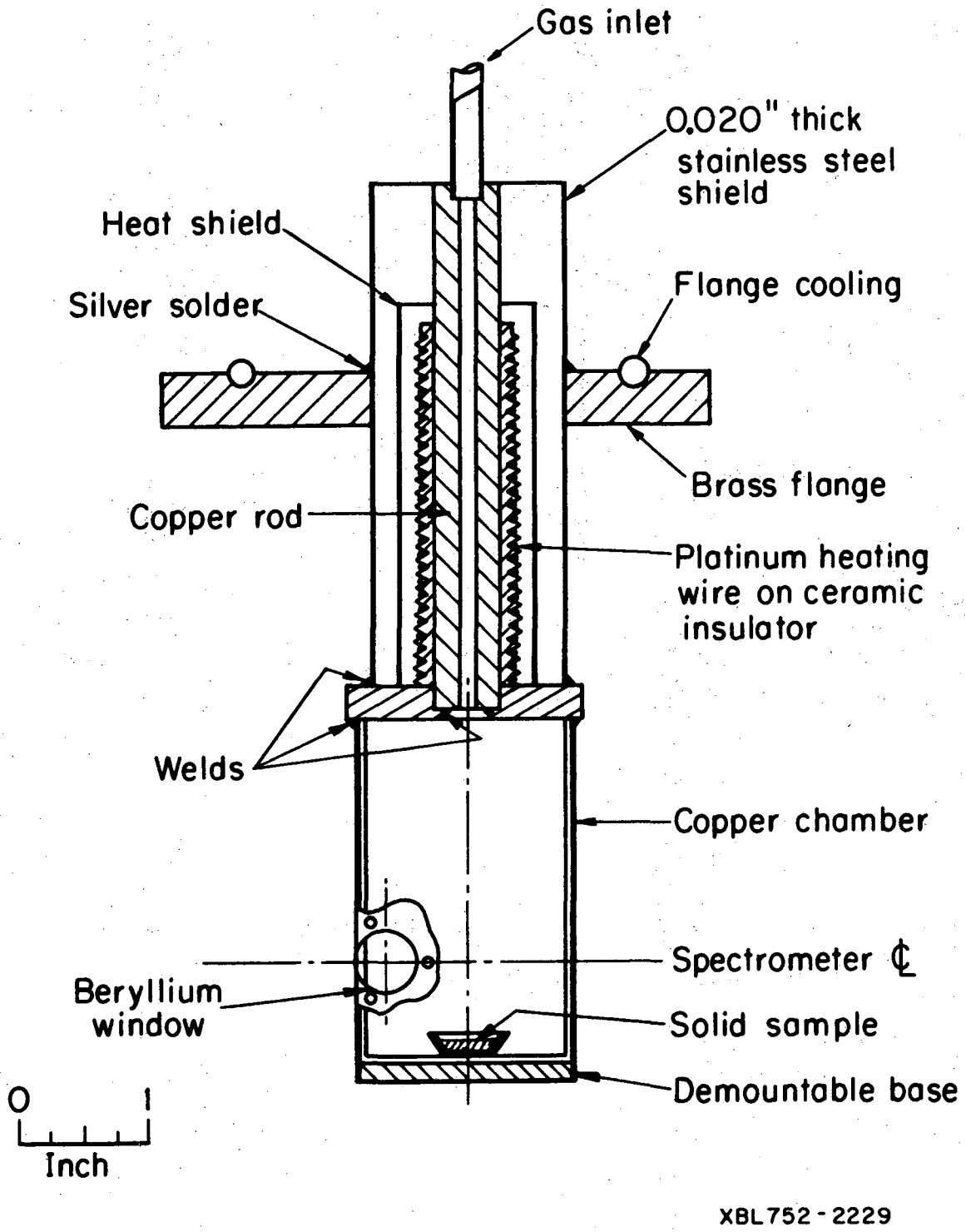

Fig. 20. The new heated gas cell.

III. ENERGY AND INTENSITY MEASUREMENT

A photoelectron spectrum can be used to calculate a number of physical quantities provided the relationship between these quantities and the raw data is known and understood. This chapter examines the theoretical basis of all the "experimental" quantities reported in this work.

A photoelectron spectroscopy experiment measures two quantities directly: the kinetic energy and number of electrons emitted by the sample in a certain direction. The source of the electrons is a level in an atom or molecule subjected to irradiation by x-rays. Traditionally, the energy measurement has been used to obtain binding energies ($E_{n\ell}$'s) of electrons in molecular orbitals via the relationship

$$E_{e,kin} = h\nu - E_{n\ell} \tag{3}$$

where $h\nu$ is the energy of exciting radiation. Some minor terms have been disregarded in the above equation. This approach is used frequently in this thesis, in particular with regards to the fluoromethane series discussed in Section X. A novel way of looking at (3) is to note that $h\nu$ and $E_{n\ell}$ are equivalent.[27] This implies that the x-ray energy can be measured if the levels of the system (called the converter by Krause since it converts x-rays to electrons) are well known.[27] This approach is adopted in the next chapter. Note that in some cases an x-ray energy can be referenced to a standard x-ray line, in which case the energy of the converter level need not be known.[27]

The intensity measured can also be related to other physical quantities. For a magnetic analyzer and non-relativistic electrons we

have:[27]

$$N(e) = GNT(h\nu)\,\eta\,(1 - \alpha)\,E_{e,kin}\left(\frac{d\sigma}{d\Omega}\right)_{\theta} N(h\nu) \qquad (4)$$

where $N(e)$ is the number of photoelectrons with a certain kinetic energy spread dE, $N(h\nu)$ is the number of x-ray photons, G is a constant containing the various solid angles, N is the density of gas particles, $T(h\nu)$ is the window transmission, η is the detector efficiency (which is a function of electron energy), α is the fraction of electrons scattered out of the beam, and $\left(\frac{d\sigma}{d\Omega}\right)_{\theta}$ is the differential photoionization cross section of the level $n\ell$ at the angle θ between the unpolarized x-ray beam and observed electrons (90° throughout this thesis). Relative values of any of the variables in Eq. (4) can be obtained without knowledge of either G or N, provided the energy dependence of the remaining terms can be determined. A major part of this work deals with relative $\left(\frac{d\sigma}{d\Omega}\right)_{90°}$ values. $N(h\nu)$ ratios are the subject of the following section. η was assumed to be the same at all energies, which is reasonable since no appreciable decrease in background counts could be detected even at energies below 100 eV. Ignorance of α is probably the largest source of error in computing cross section ratios. Ideally an auxilliary experiment should be carried out using an electron gun to determine the degree of scattering at the photoelectron energies of interest.

In order to determine photoelectron peak areas and positions accurately, Lorentzians (or in some instances Gaussians) were nonlinear least-squares fitted to the data points. A computer program (SUNDER) was written for this purpose by Claudette Lederer[28] of this laboratory. In addition to performing the fit, the program corrects the data for

the change in spectrometer transmission with electron energy. It also converts the current (momentum) distribution to an energy distribution. Counts due to x-ray satellites (for example $K\alpha_3$ and $K\alpha_4$ of magnesium) are determined by supplying the program with the satellite positions and intensity relative to the main exciting line. (Up to 39 satellites may be included.) However, all x-ray lines must have equal FWHM.

In order to account for scattered electrons, the program provides an option for adding a tail to the left (low kinetic energy) half of the peak. This tail can be constant or can decrease exponentially. A linear background is subtracted out from the spectrum. Its slope can be specified or optimized by the program.

The fitting program is particularly valuable when more than one level is thought to lie under a single experimental peak. In these instances, fixing the area ratios and separations of the underlying peaks may aid in obtaining the fit. In more favorable cases this information is determined by the program itself.

IV. X-RAY EMISSION WITH NEON AS THE CONVERTER ATOM

We begin by taking a brief look at some of the x-rays employed in this work. Our primary purpose is not so much to assign the different x-ray emission transitions as it is to determine the energy and relative intensity of the satellite lines accompanying the main x-ray. Knowledge of interfering x-ray lines is important in calculating intensity ratios in photoelectron spectra.

A. *The K X-Ray Spectrum of Sodium*

Figure 21 shows the Ne1s photoelectron spectrum taken with $NaK\alpha_{1,2}$ and its satellites up to $\sim$ 10 eV higher energy. The spectrum has been corrected for the change in spectrometer transmission with energy by multiplying the counts in the nth channel by $(I_1/I_n)^2$, where I_1 and I_n are the spectrometer currents needed to focus electrons in the first (lowest K.E.) and n^{th} channels respectively. Due to the small size of the energy range scanned, Fig. 21 can immediately be viewed as an x-ray spectrum. (The change in σ_{1s} over the entire spectrum is small.) The transitions are readily identified as shown in the figure. As mentioned earlier, $K\alpha_1$ is the transition $2p_{3/2} \rightarrow 1s$ and $K\alpha_2$ is $2p_{1/2} \rightarrow 1s$. In order to reproduce the slight asymmetry on the low kinetic energy side better, subsequent least-squares fits of peaks obtained with $NaK\alpha_{1,2}$ x-rays were made assuming two x-ray lines with a separation of 0.18 eV (chosen somewhat arbitrarily) and an area ratio of 2.2:1 (the smaller peak is on the low kinetic energy side), determined empirically for a fixed separation of 0.18 eV. It was not considered meaningful to obtain the spin-orbit splitting from atomic data, since four states exist instead

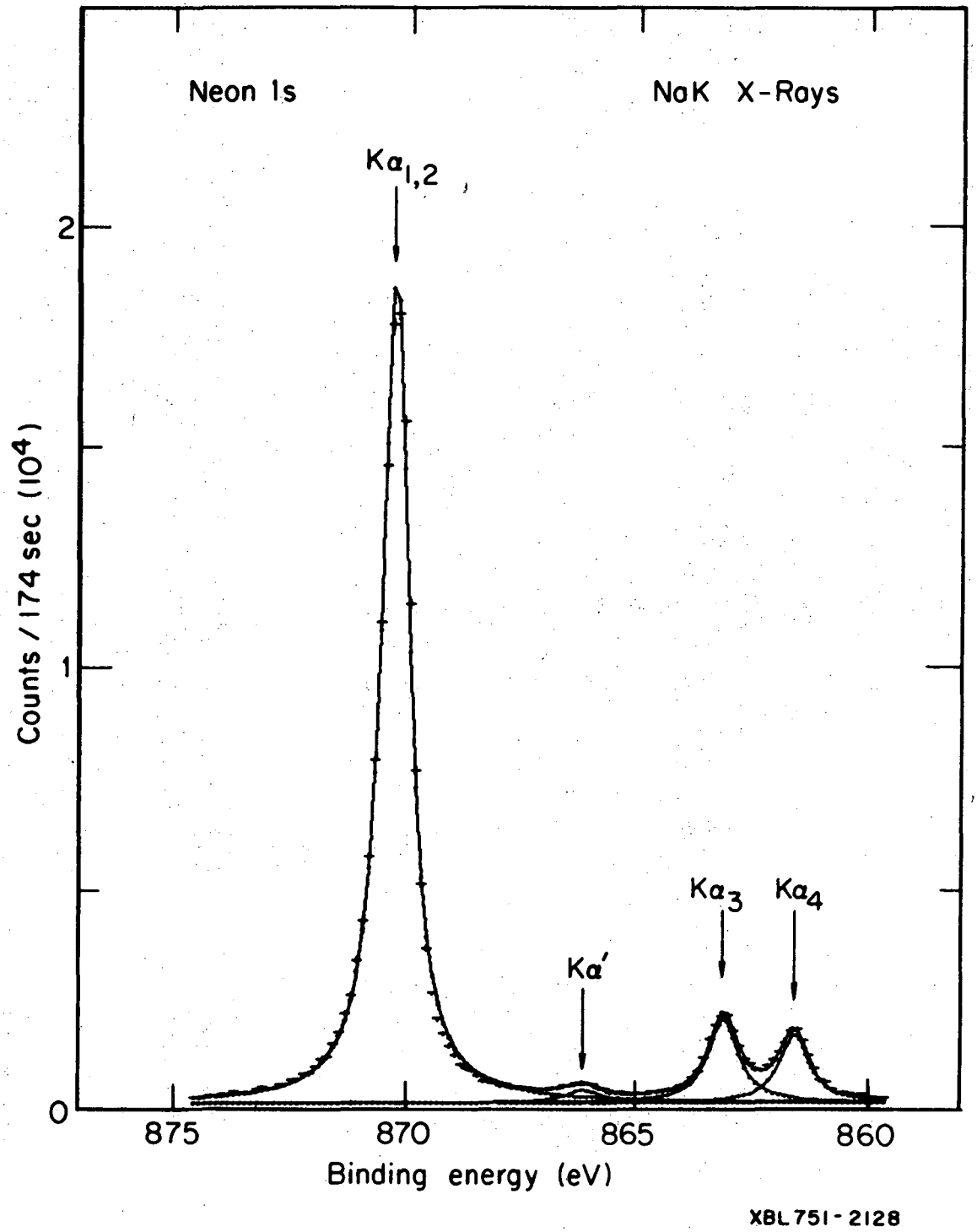

Fig. 21. Ne1s photoelectron spectrum taken with $NaK\alpha_{1,2}$ x-rays and neighboring satellites.

of two.[29]

The remaining lines in Fig. 21 correspond to transitions in doubly-ionized sodium (a hole in each of the K and L shells). Double ionization results from shake-off accompanying the ionization of the K shell, induced by electron impact.

It is interesting to compare satellite ratios and separations in sodium to those of the two neighboring atoms aluminum and magnesium. This is done in Table I. Seven kV electrons were used in the sodium-x-ray tube (vs. ∿ 13 kV with magnesium and aluminum). The shake-off probability should not change with electron energy in this range.[30]

TABLE I. Kα x-rays of sodium, magnesium and aluminum. (Ratio/Separation eV)

Element	$K\alpha_{1,2}$	$K\alpha'$	$K\alpha_3$	$K\alpha_4$
Na	1.00/0.00	0.02/4.00	0.12/7.00	0.094/8.52
Mg	1.00/0.00	0.006/5.00	0.063/8.41	0.030/10.14
Al[a)]	1.00/0.00	--	.075/9.77	.035/11.77

[a)] B. E. Mills, private communication.

Recently, Wuilleumier and Krause[9] determined shake-up intensities in neon. The intensity ratios of transitions with the same final states as those of $K\alpha_3$, $K\alpha_4$ and $K\alpha'$ were found to be 9:(17 - 22): ≲ 6.

When a fresh sodium charge is used in the x-ray tube, the linewidth improves, since oxidation is the probable cause of line broadening. The best Ne1s spectrum we have obtained is shown in Fig. 22. To our knowledge, 0.58 eV is the narrowest Ne1s peak ever recorded without monochromatized

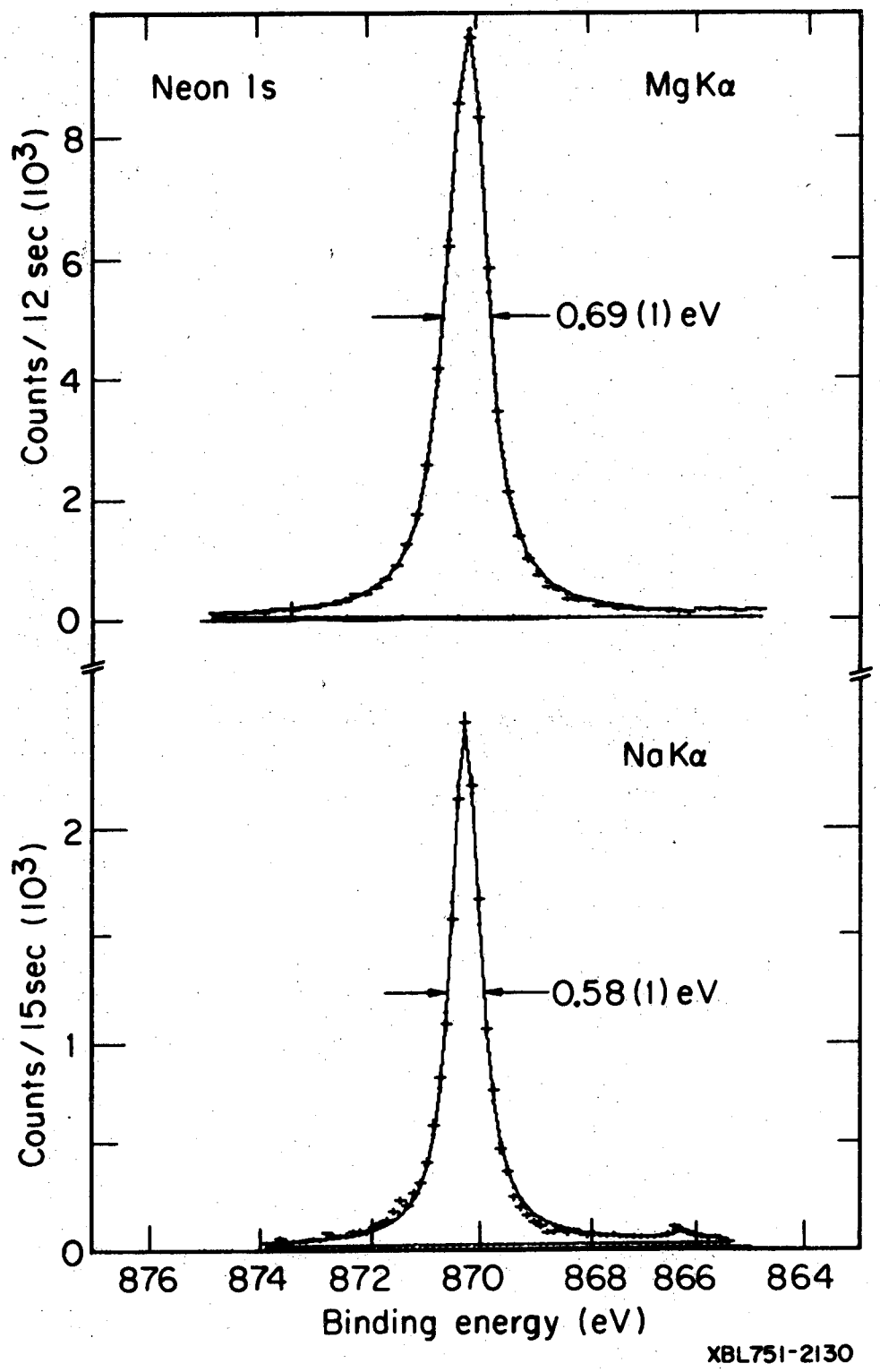

Fig. 22. Ne1s XPS spectrum with $MgK\alpha_{1,2}$ and $NaK\alpha_{1,2}$.

x-rays. (A FWHM of 0.39 eV was obtained by Gelius et al.[1] with monochromatic AlKα.) Furthermore, a yet narrower line should be attainable if the resolution of the instrument is pushed to the limit (approximately 0.1 eV was contributed by the spectrometer in the above experiment). The Nels FWHM with MgKα is .69 eV under similar conditions. Gelius et al.[1] obtained the inherent width of the neon 1s level by deconvoluting the photoelectron peak. Using their value of 0.23 eV we can determine the $K\alpha_{1,2}$ x-ray linewidth for magnesium and sodium. Neglecting contributions from the spectrometer resolution we obtain a FWHM of 0.65 eV for $MgK\alpha_{1,2}$ and 0.54 eV for $NaK\alpha_{1,2}$. These values should be regarded as upper limits to the corresponding linewidths.

From the experiment described in Section II.B, part 3.(b), it is possible to calculate an approximate value of the $NaK\alpha_{1,2}$ x-ray energy. Since both the magnesium and sodium runs were made without changing the slit position, the kinetic energy difference is given by Eq. (2), where the currents now correspond to the neon 1s peak position with $MgK\alpha_{1,2}$ and $NaK\alpha_{1,2}$. A value of 212.21 eV was obtained. This yields a $NaK\alpha_{1,2}$ energy of 1041.4 eV from the known $MgK\alpha_{1,2}$ energy of 1253.6 eV, in good agreement with the literature value of 1041.0 eV.[2]

B. *The M X-Ray Spectrum of Yttrium*

Using Ne2p as the converter level (since it is probably the most intense single level at the YMζ energy) we have obtained the satellites at energies higher than the main YMζ line. They are shown in Fig. 23 with the assignments taken from a similar spectrum reported earlier by Krause.[5] In order to convert Fig. 23 to an x-ray spectrum two major corrections must be applied. The first is due to the increase in

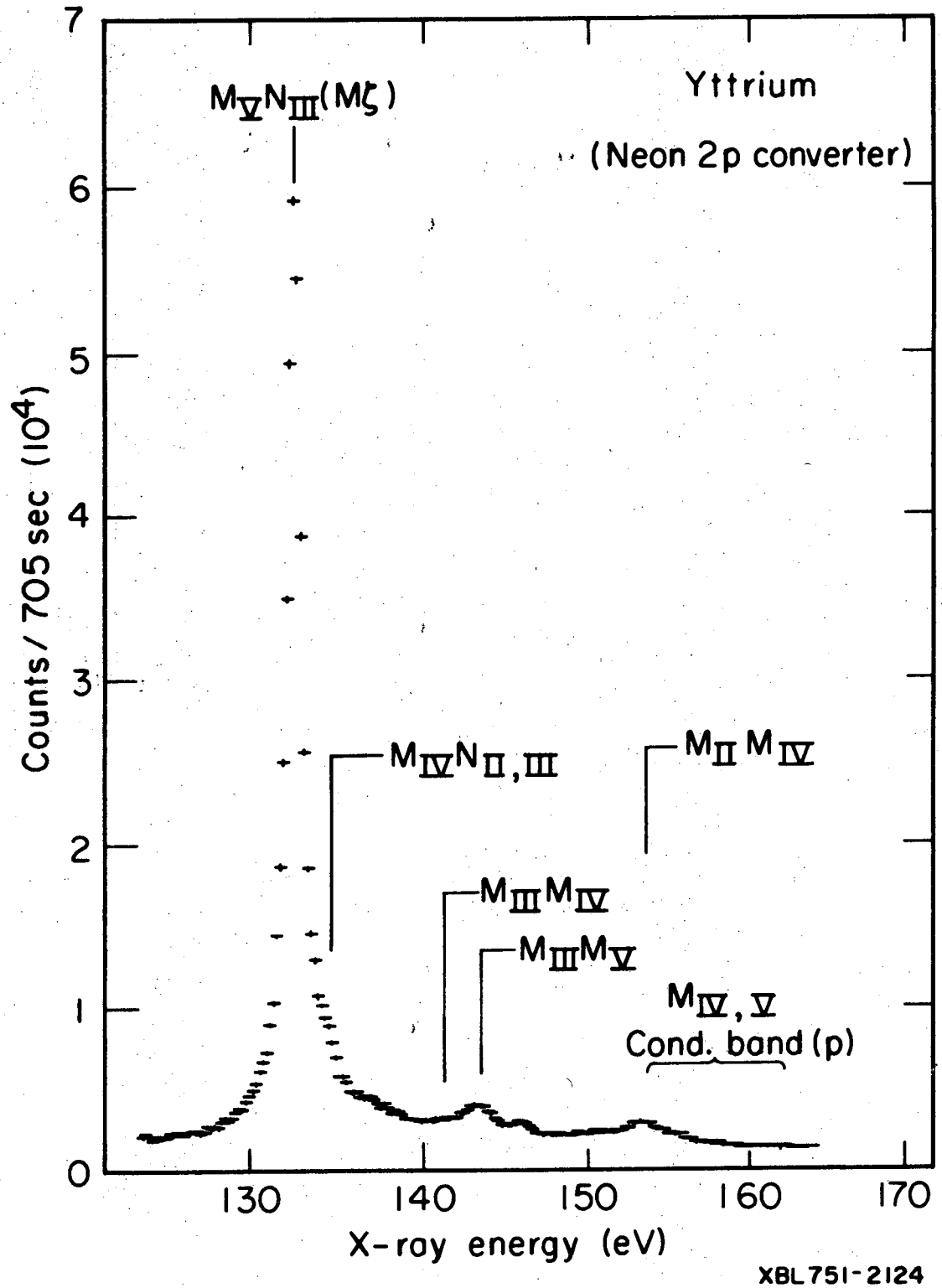

Fig. 23. The M x-ray spectrum of yttrium. The spectrum is not corrected for the change in spectrometer transmission or Ne2p photoelectric cross section with energy.

spectrometer transmission with photoelectron energy. (This correction results in a 30% decrease in count rate at the high energy end of the spectrum.) The second correction is opposite to the first, and is necessary because the differential photoelectric cross section of Ne2p, $(\frac{d\sigma}{d\Omega})_{90°}$ *decreases* with photon energy in the yttrium M energy range. According to Wuilleumier,[21] the count rate at the high energy and of Fig. 23 should be increased by ∿ 80%. The overall result is that Fig. 23 underestimates the intensities of the YMζ satellites. For the purposes of subtracting out the interfering x-rays in a photoelectron spectrum taken with YMζ, eight Lorentzians with equal FWHM were fitted to the raw data in Fig. 23. The separations and area ratios relative to YMζ are shown in Table II, after correcting for spectrometer transmission (but not for changes in $(\frac{d\sigma}{d\Omega})_{90°}$). These values were used in all the fitted YMζ spectra reported in this work. The reason for the neglect of the cross section correction (large as it may be) is the lack of information about the exact changes of the photoelectric cross section with energy for the systems considered in this thesis. In effect we are assuming that in the neighborhood of the YMζ energy, $(\frac{d\sigma}{d\Omega})_{90°}$ for a given MO decreases with energy in the same manner as $(\frac{d\sigma}{d\Omega})_{90°}$ for Ne2p.

TABLE II. X-ray satellites used in fitting YMζ spectra. (Satellite/ratio/separation [eV])

1	2	3	4	5	6	7	8
1.00	0.058	0.018	0.025	0.018	0.018	0.038	0.013
0.00	1.90	3.24	4.45	5.95	8.69	10.65	13.09

Krause and Wuilleumier[4] obtained a YMζ photon energy value of 132.29 eV by measuring the energy difference, ΔE, between photoelectrons $XeN_{IV,V}$ (YMζ) and Auger electrons $N_V - O_{II,III}O_{II,III}$ of xenon (see Ref. 4 for details). This result is in good agreement with the results of other workers.[31] The exact photon energy was not needed in this thesis since no measurements of absolute binding energies were made with YMζ.

V. EXAMPLES OF HIGH TEMPERATURE GAS-PHASE SPECTRA

The study of the species discussed in this chapter required the use of one of the two heated gas cells described in Section II.D. NF_2 was produced by pyrolyzing N_2F_4. The remaining compounds are solids at room temperature with insufficient vapor pressure for study as gases (under ∿ 10 microns) in our apparatus. They were therefore heated in the new gas cell.

A. *NF_2 Radical*

N_2F_4 was heated to ∿ 200°C at a pressure of approximately 50 microns. Under these conditions it should be essentially completely dissociated into NF_2.[32] Since NF_2 is paramagnetic, the core-ionization spectrum should show two peaks depending on whether the remaining core electron is coupled parallel or antiparallel to the valence spin.[12] This expectation is borne out in Fig. 24 showing the core spectra of NF_2 and N_2F_4. The N1s splitting of 1.93 eV in NF_2 is the largest observed to date in a gaseous species. The intensity ratio of the multiplet-split N1s peak is 3.4 to 1, in excess of the simple multiplet ratio $(S+1)/S = 3$. Positive departures from the multiplet ratios have been observed in NO and O_2.[33] According to Bagus et al.,[33] these departures are at least partially caused by differences in charge distribution between the high- and low-spin final states. A detailed discussion of NF_2 and N_2F_4 is given in Ref. 12.

B. *Paranitroaniline*

Paranitroaniline powder was heated to ∿ 50°C (temperature was not monitored carefully). The N1s and O1s spectra are shown in Figs. 25 and

0 0 0 0 4 2 0 6 0 2 8

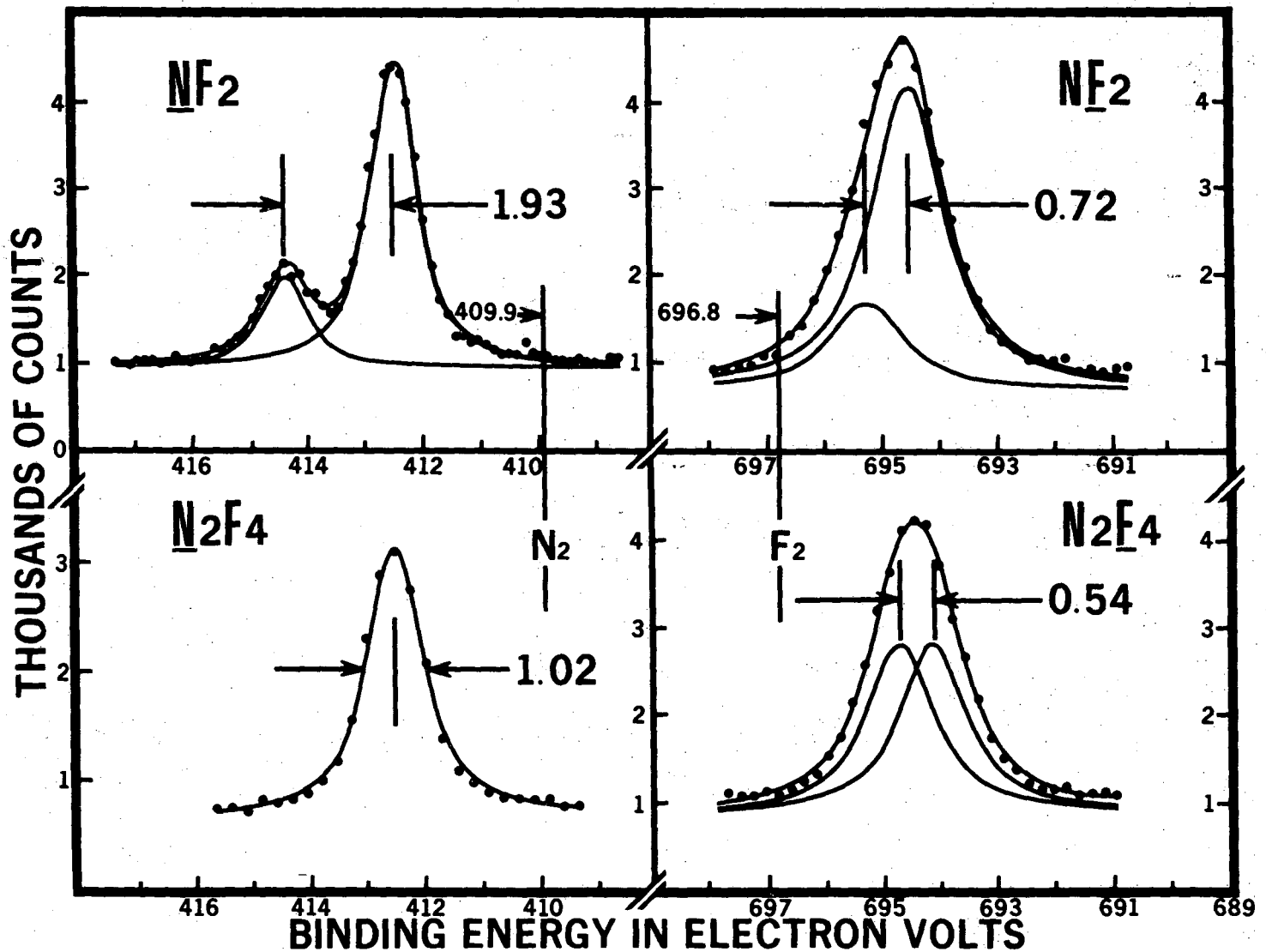

XBL 736-753

Fig. 24. The 1s-core photoelectron spectra of NF_2 (∿ 200°C) and N_2F_4 (room temperature). Figure is taken from reference 12.

26, respectively. The choice of this compound was motivated by a study of a number of nitroanilines in the solid phase.[34] One interesting feature of this series is the occurrence of extra peaks in the core spectrum. For example, the NO_2 nitrogen 1s of solid nitroaniline shows two components of nearly equal intensity separated by 1.8 eV.[34] The corresponding peak in the gas-phase (Fig. 25) does not show any visible splitting. It is broader than the NH_2 nitrogen peak, however, and a fit of two equal intensity peaks gave a separation of 0.6 eV. In both the solid and gas phase spectra the NO_2 nitrogen peak area is larger than that of NH_2 (the ratio is 1.16 in the gas phase).

The oxygen 1s spectrum has a definite extra peak in both solid and gaseous nitroaniline. The separation is 2.38(3) eV in the gas, in good agreement with the 2.2 eV obtained in the solid.[34]

It is possible to understand the occurrence of multiple peaks in the core spectra of some nitroanilines in terms of shake-up theory[35] (double excitation). As noted by Gelius,[36] the sudden change in potential due to the removal of a core electron is felt most strongly by the electrons in molecular orbitals with a high degree of localization on the ionized atom. Furthermore, charge transfer to the ionized center, both in the neutral molecule and in the ion, should favor high shake-up probabilities.[33]

Using paranitroaniline as an example, Pignataro and Distefano[34] argue that charge transfer from the amino nitrogen to the nitro nitrogen occurs via the resonance structure

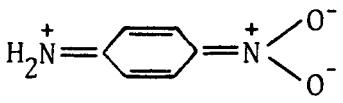

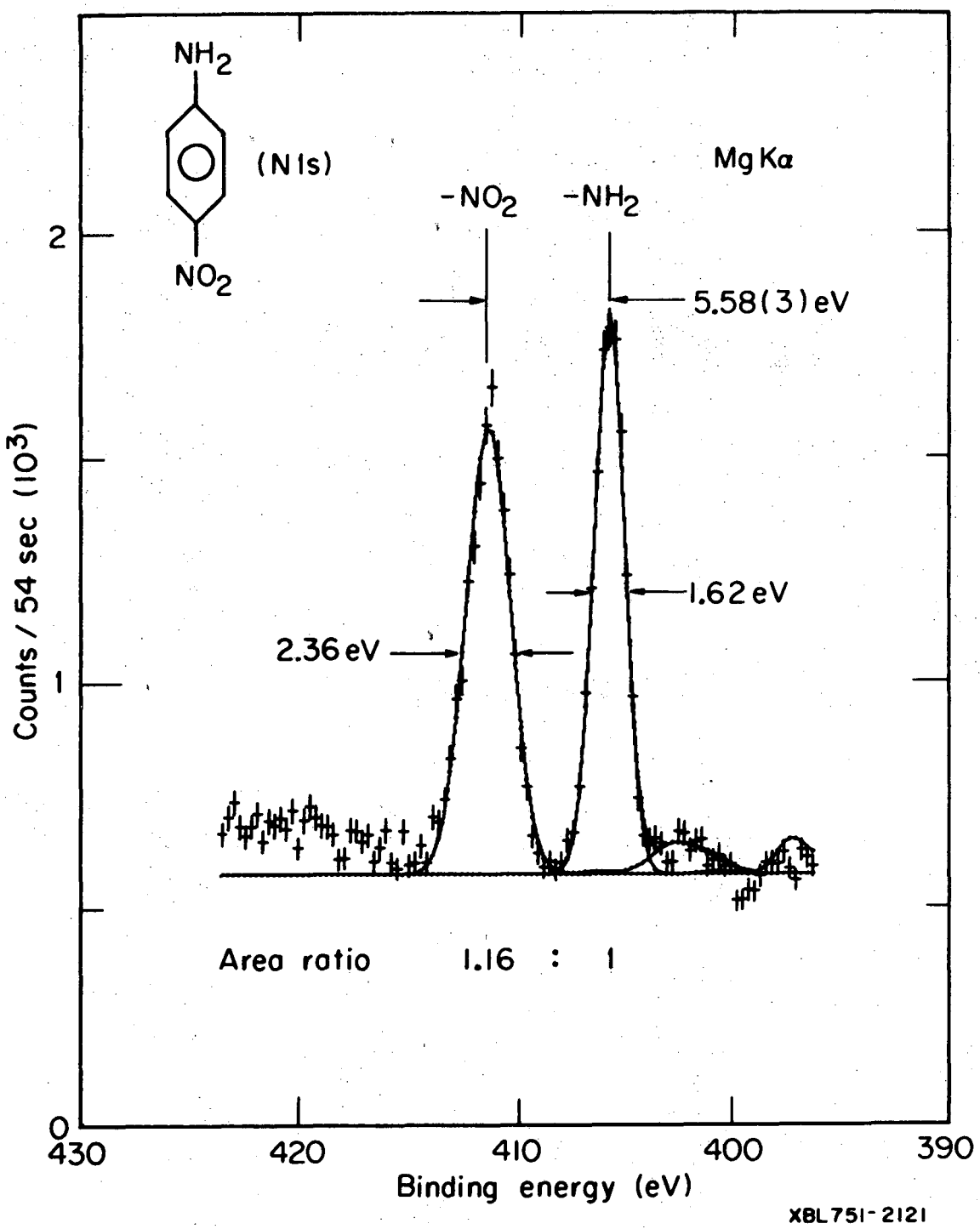

Fig. 25. The N1s spectrum of p-nitroaniline run in the new heated gas cell.

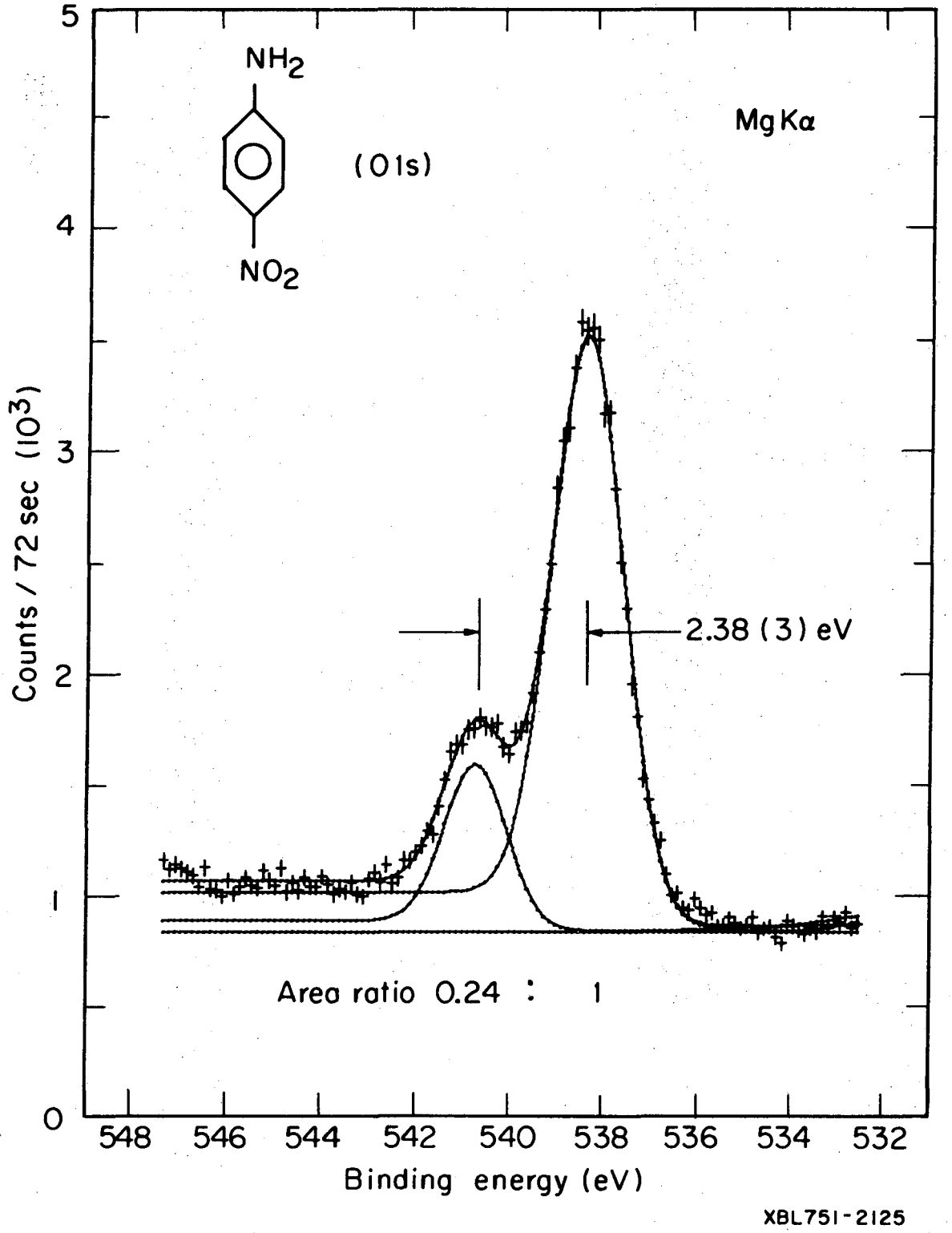

Fig. 26. The O1s spectrum of p-nitroaniline. The extra peak is probably due to double excitation (shake-up).

This claim is supported by the decrease in the binding energy difference between the two nitrogens (the difference is 5.5 eV in the solid[34] and 5.3 in the gas), compared to the nitrogen binding energies in aniline and nitrobenzene (6.9 eV separation[34] in the solid and 6.1 eV[37] in the gas). When the nitro N1s is ionized, charge flow is enhanced by the presence of the positive hole, resulting in high shake-up intensity. Similarly, ionization of the oxygen 1s is accompanied by intense shake-up, but the charge flow in this case is impeded by the presence of a negative charge on the oxygen.

Pignataro and Distefano compared the separation of the double excitation peak from the main peak with the energy of the $V \leftarrow N$ ultraviolet transition. (N denotes the ground state and V the lowest excited singlet state of the neutral species. This transition requires an energy of 3.3 eV[34] in paranitroaniline.) It is not surprising that the separation in oxygen seems to agree better with the uv transition energy than does the nitrogen separation: more orbital reorganization and contraction takes place in the latter case due to electron flow. The discrepancy between the solid and gas phase measurement of the separation in nitrogen (1.8 eV versus 0.6 eV) is intriguing. It may well be due to differences in relaxation mechanisms in the two phases.

As noted earlier, the intensity ratio of the nitro N1s plus shake-up to the amino N1s is not unity. In terms of the sudden approximation (overlap) picture pursued by Bagus et al.,[33] this departure should come as no surprise. For example, for molecular oxygen 1s ionization, a probability of 0.406 was predicted for $^4\Sigma^-$, 0.178 for $^2\Sigma^-$, and 0.417 for multiple excitation. In this approach, there is no *a priori* reason to

expect equal intensities for the two nitrogens.

C. *Other Systems*

The new heated gas cell was used by S. A. Avenzino to run the recently synthesized bis[N,N,-bis(trimethylsilyl)amino]tin(II), for which the binding energy of the Sn $3d_{5/2}$ level (using argon $2p_{3/2}$ as the reference level) was found to be 491.93 eV. The spectrum is shown in Fig. 27.

T. F. Schaaf studied the aluminum 2p, oxygen 1s and carbon 1s levels of the following derivative of aluminum acetyl acetonate:

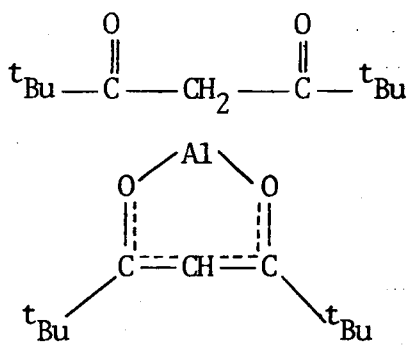

where ^{t}Bu stands for the tertiary butyl group.

The above two species, together with a number of other systems currently under study, will be discussed in future publications.

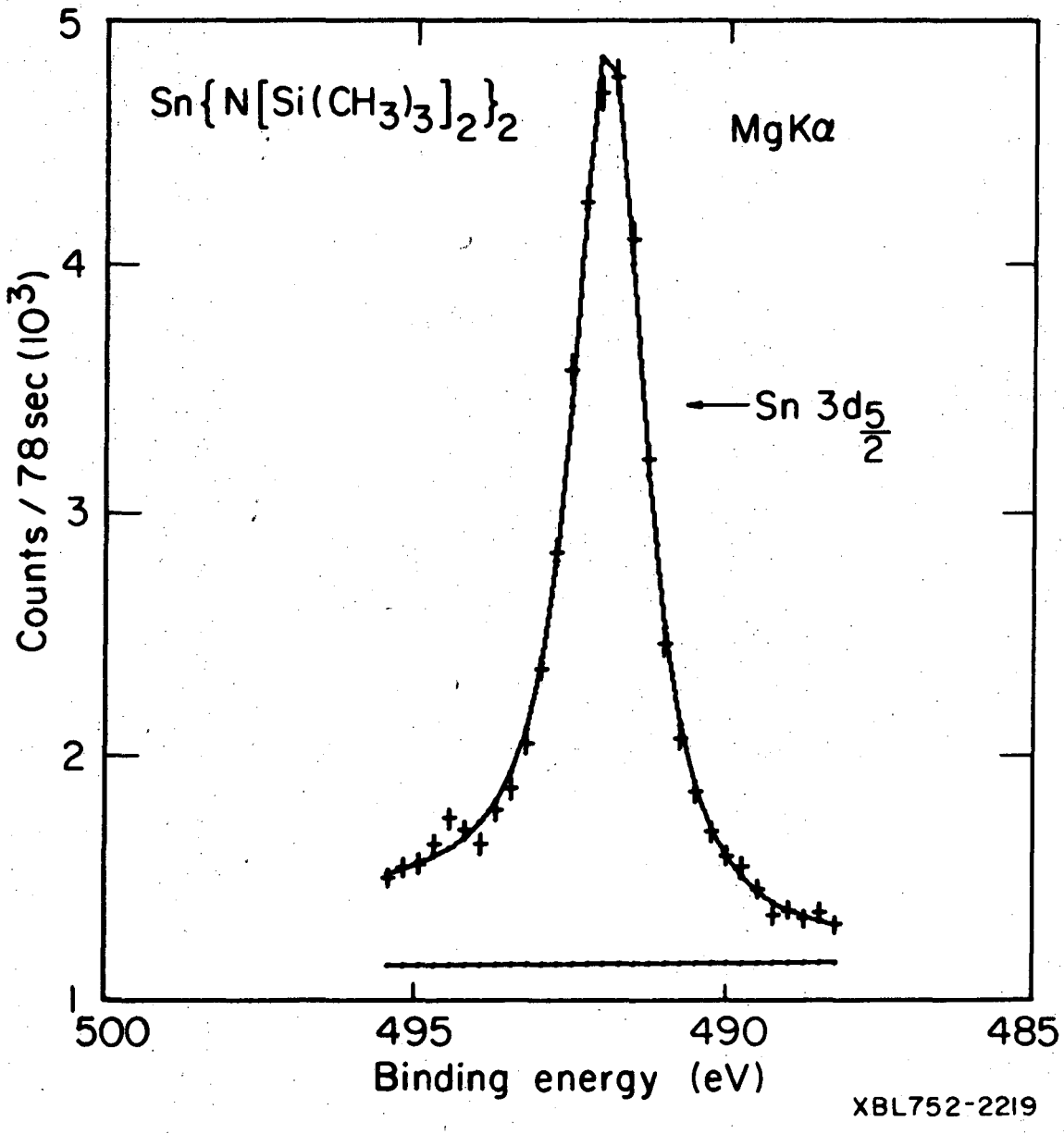

Fig. 27. Tin $3d_{5/2}$ level of bis[N,N,-bis(trimethylsilyl)amino]tin(II). The binding energy is 491.93 eV.

VI. EXAMPLES OF SPECTRA OBTAINED WITH SODIUM X-RAYS

All the systems discussed in this chapter have been investigated earlier by other workers using conventional MgKα or AlKα x-rays. Some were recently studied with monochromatized AlKα x-rays (by the Uppsala Group). The measurements on these molecules are repeated here with NaKα x-rays in order to assess the advantages, if any, of the new photon source.

A. *Oxygen (1s)*

The oxygen core spectrum has been reported by a number of workers.[38] It is shown again in Fig. 28, as obtained with both magnesium and sodium x-rays. The sodium spectrum shows some improvement in resolution over magnesium (0.66(2) eV versus 0.81(1) eV FWHM when the two multiplet peaks are constrained to have the same linewidth), but is still inferior to the monochromatized x-ray spectrum[1] (0.46 eV). The multiplet peak separation of 1.13(2) eV is in excellent agreement with previous measurements.[38] Under the constraint of equal linewidths for the two multiplet peaks, the intensity ratio is 2.51(3) with magnesium and 2.48(5) with sodium, again in very good agreement with the mean ratio measured by Davis et al.[33] (2.47(3)). Interestingly, when the linewidths are allowed to vary, the above ratios change. With magnesium, one now gets 2.16(7) (the new linewidths are 0.90(5) eV and 0.78(2) eV for $^2\Sigma^-$ and $^4\Sigma^-$ respectively), and with sodium the ratio changes to 2.3(1) (FWHM of 0.71(7) eV and 0.65(3) eV respectively). This result is in excellent agreement with the calculated value of Bagus et al.[33] (2.28). Bagus calculated ground state wave functions as well as hole state wave functions for the two final states, finding that the valence shell charge distributions changed considerably in going

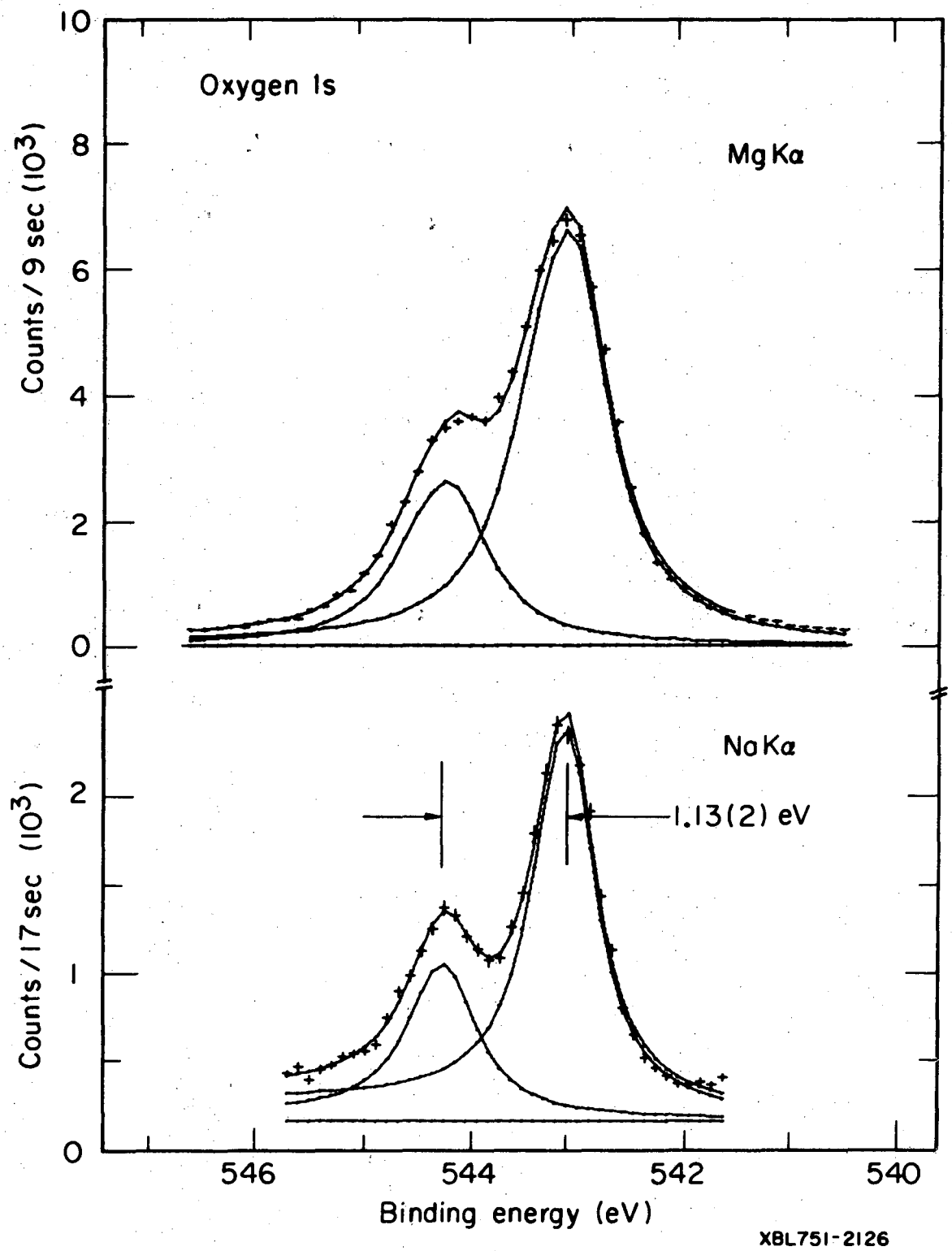

Fig. 28. Oxygen 1s taken with magnesium (upper) and sodium (lower spectrum) x-rays. $\Delta E/E$ of the instrument was the same for both runs.

from the neutral to the ionized system. Furthermore, the charge distributions in the high- and low-spin final 1s hole states were found to be different.[33] This latter observation is important, and is the basis for the departure of the intensity ratio from the simple multiplet ratio of two. According to Gelius et al.,[39] different charge reorganizations with ionization frequently result in different Franck-Condon factors and hence different linewidths. All this seems to suggest that the value obtained by varying the linewidths of the two multiplet states independently may well be the correct ratio (rather than the one reported by Davis et al.[33]).

B. *Methane (C1s)*

The recent introduction of monochromatized x-ray sources into the field of gas-phase photoelectron spectroscopy[1] has made possible the study of inherent shapes of electronic levels in atoms and molecules. One interesting result of such studies is the realization of the importance of vibrational excitation in core-level spectra. Core ionization results in a reorganization of the electronic charge of the system, which frequently leads to a decreased bond length and a narrower molecular potential of the excited state.[39] This results in vibrational excitation. Thus Gelius et al.[39] were able to measure Franck-Condon factors in a number of core spectra (for example, CO and N_2). One particularly favorable case is the carbon 1s of methane. The monochromatized x-ray spectrum[39] shows definite evidence for two vibrational levels, the third being obtained by curve fitting. (The experimental spectrum also seems to suggest its presence.) With sodium K x-ray (Fig. 29) we were able to observe a definite asymmetry on the high binding energy side. Using the experimental Franck-Condon

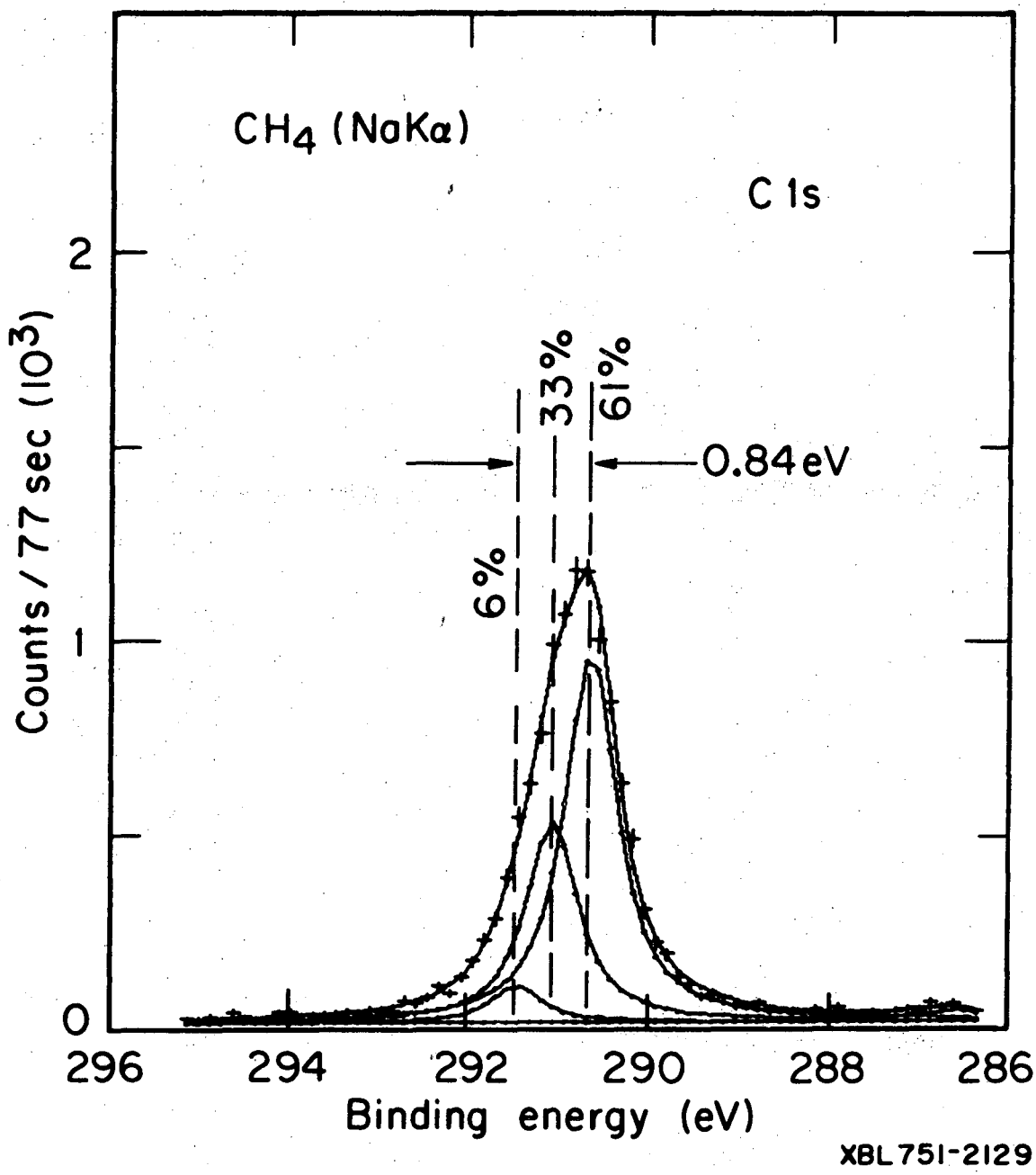

Fig. 29. The carbon 1s spectrum of methane. Counts were obtained at increments of 0.13 eV. Three Lorentzians of equal FWHM were used in the fit. (The linewidth of each was determined to be 0.65(2) eV.) The ratios used are those of reference 39. The Derived separations are 0.43(2) eV and 0.41(7) eV in order o of increasing binding energy. Compare this spectrum with Fig. 2 of reference 39.

factors of Gelius et al [39] we obtained a good fit of the overall peak (weighted variance was 1.48). We also obtained the separation of the vibrational levels of the excited state, 0.43(2) eV and 0.41(7) eV, in order of increasing binding energy. (Compare with 0.43(2) from Ref. 39.) Since the core hole is symmetrically located with respect to the four hydrogens, only the symmetrical C-H stretching mode will be excited. The agreement with theory[40] and with the results of Gelius et al. speaks well for the ability of NaKα to probe vibrational envelopes.

C. *Meta Difluorobenzene (C1s)*

Core level ionization in the fluorinated benzenes is the subject of a paper by Davis, Shirley and Thomas.[41] The authors measured core binding energy shifts relative to binding energies of standards. A CNDO potential model was used to predict the shifts. Starting with the electrostatic potential of an electron at a nucleus

$$e^2 \langle \sum_i 1/r_i \rangle - e^2 \sum_j Z_j/R_j \qquad (5)$$

where r_i is the distance between the parent nucleus and the ith electron, and R_j is the distance between the nucleus and the jth other nucleus with charge Z_j. One takes the negative of the difference in electrostatic potential at a nucleus between two molecules to be the 1s binding energy shift of an electron associated with that nucleus.[42] In the fluorobenzene work, the first term was evaluated exactly. The second was calculated in two ways: 1) all basis functions were assumed to be spherically symmetrical and only the diagonal matrix elements between them were retained (point charge); 2) r^{-1} integrals were evaluated exactly, retaining the diagonal

elements as well as the off-diagonal matrix elements between p orbitals on the same center (p - p'). In both cases, CNDO wavefunctions were used.

The model provides a binding energy shift for every 1s electron in a fluorinated benzene. In comparing with experiment, however, Davis et al. were limited by the inability of the existing resolution to distinguish between carbon atoms with small binding energy differences (roughly under 1 eV). One interesting case is metadifluorobenzene. Four types of carbon may exist in principle and this is confirmed by model calculations (Table III). Experimentally, the $C_{1,3}$ type is easily separated from the rest (see Fig. 30). The remaining carbons are not easily distinguishable, but deconvolution of the main peak into three peaks of equal FWHM and area ratios of 1:1:2 yields the separations listed in Table III. The results are in good agreement with the theoretical predictions of Davis et al.

TABLE III. Comparison of carbon 1s shifts in metadifluorobenzene with theoretical CNDO potential model predictions.

	Nucleus	Exptl (eV)	Calcd (eV) (point charge)	Calcd (eV)[41] diagonal + p - p' elements
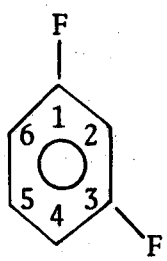	$C_{1,3}$	0.00	0.00	0.00
	C_2	-2.12(3)	-2.33	-3.01
	$C_{4,6}$	-2.46(1)	-2.39	-3.04
	C_5	-1.90(3)	-1.82	-2.26

The smaller linewidth of the peaks obtained by deconvolution, compared to that of the $C_{1,3}$ peak (0.62(3) versus 0.82(3) eV), is somewhat disturbing but not necessarily unrealistic. There is no experimental basis for

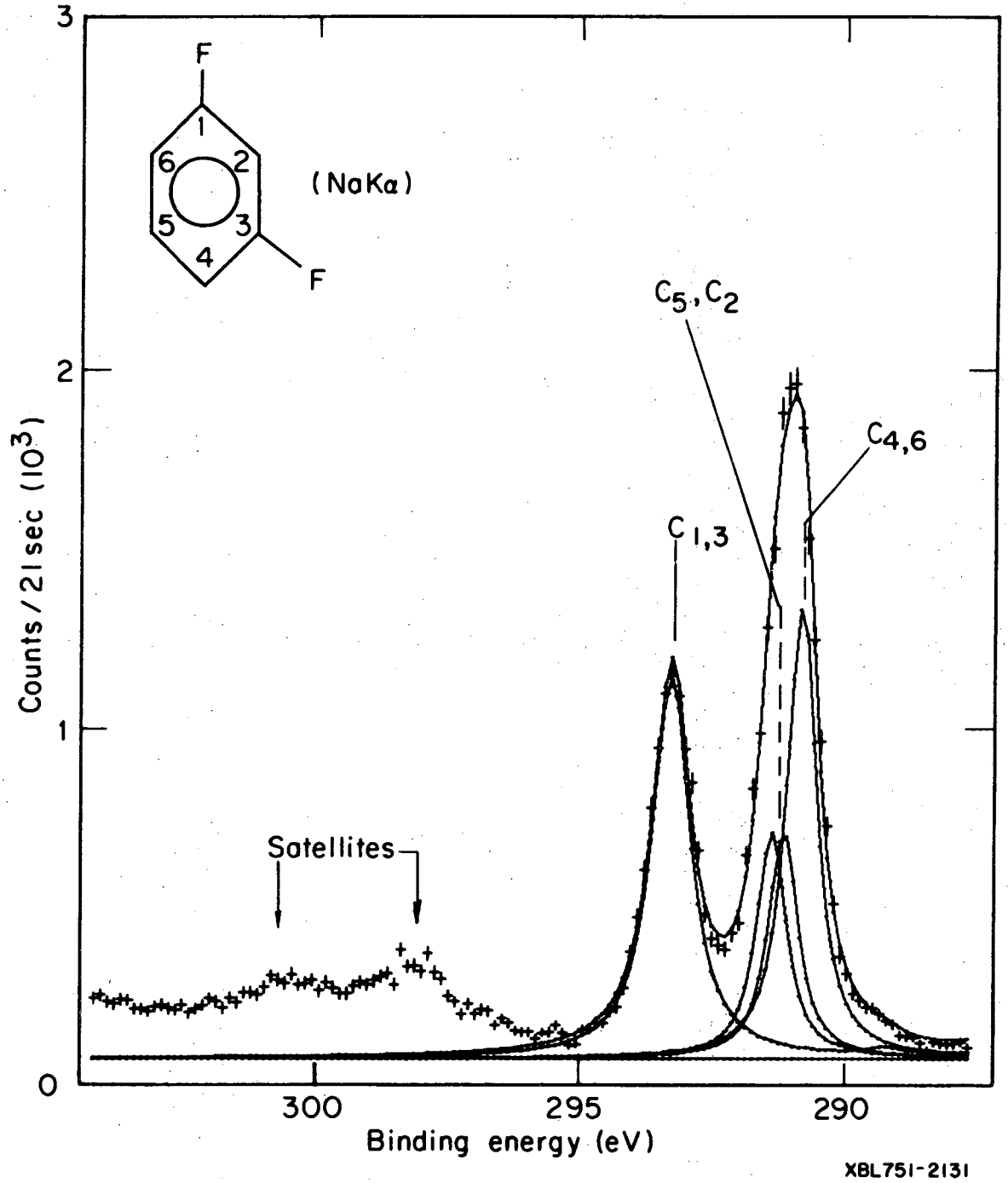

Fig. 30. Carbon 1s and satellite peaks of metadifluorbenzene with NaKα x-rays. Linewidths are: $C_{1,3}$ peak 0.82(3) eV, remaining peaks 0.62(3) eV each.

distinguishing C_2 from C_5; our assignment was made following the model predictions. Clark et al.[43] measured the XPS shifts of solid metadifluorobenzene. From comparison with the other fluorobenzenes they concluded that the carbon *meta* to the fluorines (C_5) should have the higher binding energy. By deconvoluting the main peak, the authors also found that C_2 and $C_{4,6}$ had the same energy (0.5 eV lower than C_5). A good fit of our experimental data was obtained when the composite peak was deconvoluted into two peaks with a constrained area ratio of 3:1. The separation thus determined was 0.42(3) eV, in good agreement with Clark et al.

Figure 30 shows two satellites on the high energy side separated by $\sim$ 2.3 eV. This is the same as the distance between the two main carbon peaks. It therefore seems possible that the same transitions are involved in both satellites. The distance between each of the two carbon peaks and the associated satellite is $\sim$ 7.5 eV. The author has observed satellites with roughly this separation in a number of aromatic compounds. For example, in benzene itself, a satellite having an intensity 0.25 that of the main peak is present $\sim$ 7 eV away. A smaller peak occurs at $\sim$ 11 eV below the main peak. This indicates that the satellites observed in metadifluorobenzene are probably characteristic of the benzene ring in general. Optical data on benzene[44] indicates the presence of four Rydberg series converging to the first ionization potential (9.247 eV). Several members of these series have energies around 7 eV. Thus the most likely interpretation of the satellites in Fig. 30 is that they correspond to electron energy loss due to transitions in *neutral* metadifluorobenzene, since this is by far the most abundant species in the target chamber. This interpretation is in line with the conclusion of Aarons et al.,[45] drawn on the basis of simple

shake-up theory and a localized-hole final state, that no shake-up transitions are likely to occur in benzene at energies < 10 eV from the main peak. However, the pressure dependence of the satellite peaks must be determined before a definite assignment can be made.

D. *Phosphorous Pentafluoride (F1s)*

The XPS core spectrum of PF_5 has been investigated by Shaw, Carroll, and Thomas.[46] One interesting feature of this molecule is the existence of two types of fluorines. The two axial bonds are longer and weaker than the three equatorial bonds. As Shaw et al. note, all five fluorines become equivalent in an nmr experiment above -197°C, due to rapid exchange brought about by the large amplitude vibrations.[47] An XPS experiment, on the other hand, is fast enough to detect the inequivalence.

The F1s binding energy splitting in PF_5 is not as large as in SF_4 and ClF_3, the other two molecules studied by Shaw et al. An analysis of the fluorine charges in these molecules by the authors confirms this by predicting a smaller difference in charge between the two types of fluorines in PF_5. Our NaKα spectrum (Fig. 31) strongly suggests the existence of two peaks, and a fit constraining the area ratios to 3:2 gave a separation of 1.08(3) eV, in good agreement with the 1.2(1) eV value obtained by Shaw et al.[46] The linewidths were found to be 1.85(3) eV for the equatorial fluorines and 2.00(5) eV for the axial. (Shaw et al. fixed the FWHM at 2.0 eV.) Gaussians were found to be far superior to Lorentzians in this case. When our linewidth values are considered along with the linewidths in SF_4[46] and ClF_3,[46] it is seen that in each of the three molecules, the peak corresponding to the axial fluorine(s) is broader than the peak due to the equatorial fluorine(s).

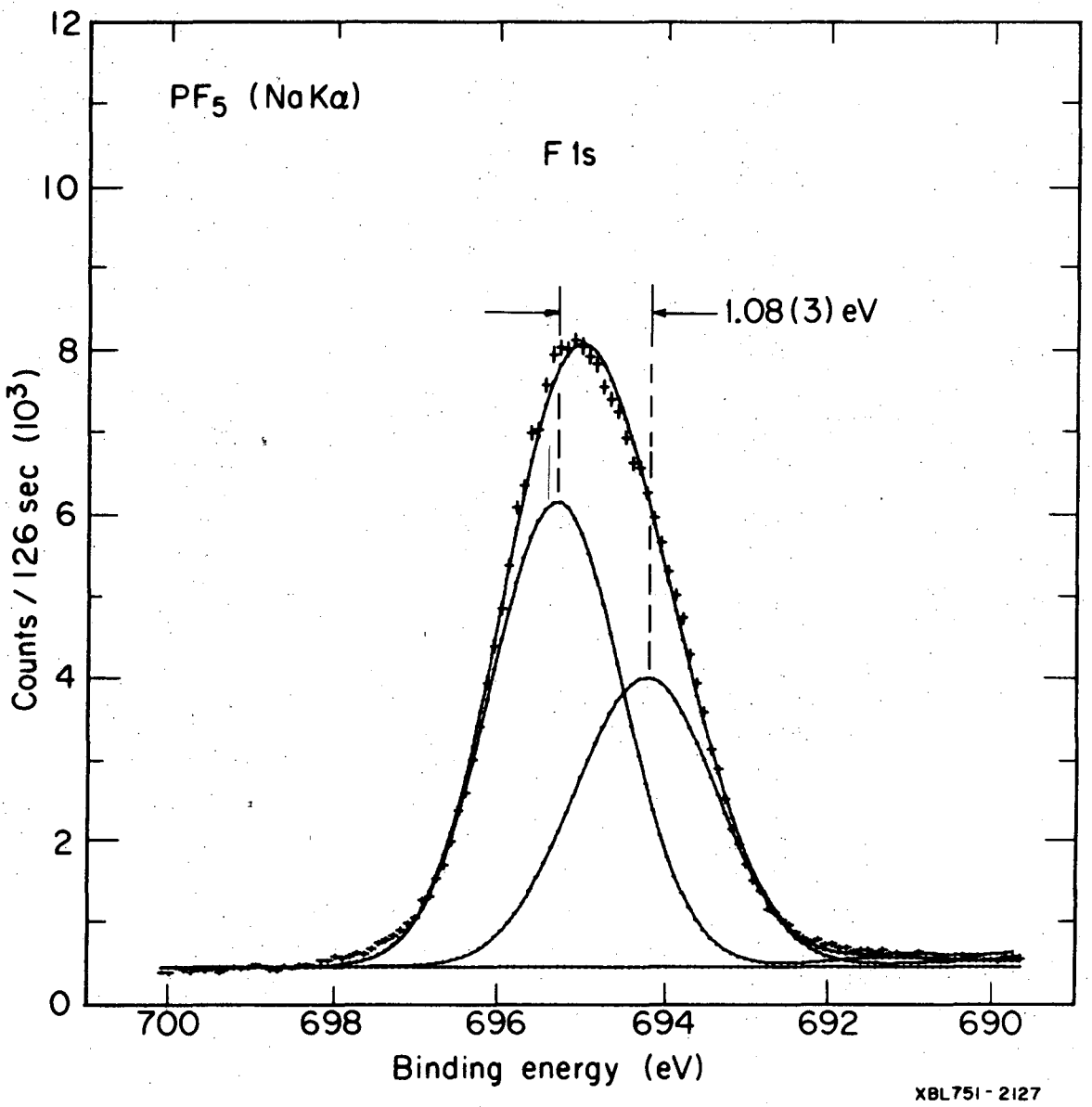

Fig. 31. Fluorine 1s of PF_5. The area ratio was constrained to 3:2. The separation obtained is 1.08(3) eV. Linewidths of the two Gaussians are 1.85(3) eV (equatorial) and 2.00(5) eV (axial).

VII. THE RARE GASES NEON, ARGON, KRYPTON AND XENON

Photoionization in the rare gases is a popular subject of study by experimentalists and theoreticians alike. From the experimental point of view, the rare gases are the only species present in atomic form at room temperature. Prompted by the availability of experimental data, many calculations have been performed. The rare gases offer an excellent introduction to the study of other elements in the periodic table. In this chapter, we are primarily interested in the relative cross sections of the two outermost subshells at the MgKα and YMζ energies. We also report briefly on the YMζ spectra of the 3d and MNN Auger lines of krypton, as well as the 4d levels of xenon.

A. *Results and Discussion*

1. Neon

The most comprehensive experimental study of photoionization in neon was conducted by Wuilleumier and Krause.[9] Since both single- and multiple-electron processes, as well as angular dependence were investigated, the authors were able to partition the total photoionization cross section[48] among the different photoionization events. Furthermore, by using sixteen different x-ray energies, they determined the variation of the cross section with photon energy.

In the present work only the 2s and 2p subshells were studied, using MgKα and YMζ (see Fig. 32). The binding energies were measured relative to each other and the resulting separation is compared to the value obtained by the Uppsala group in Table IV. The three measurements are in good agreement.

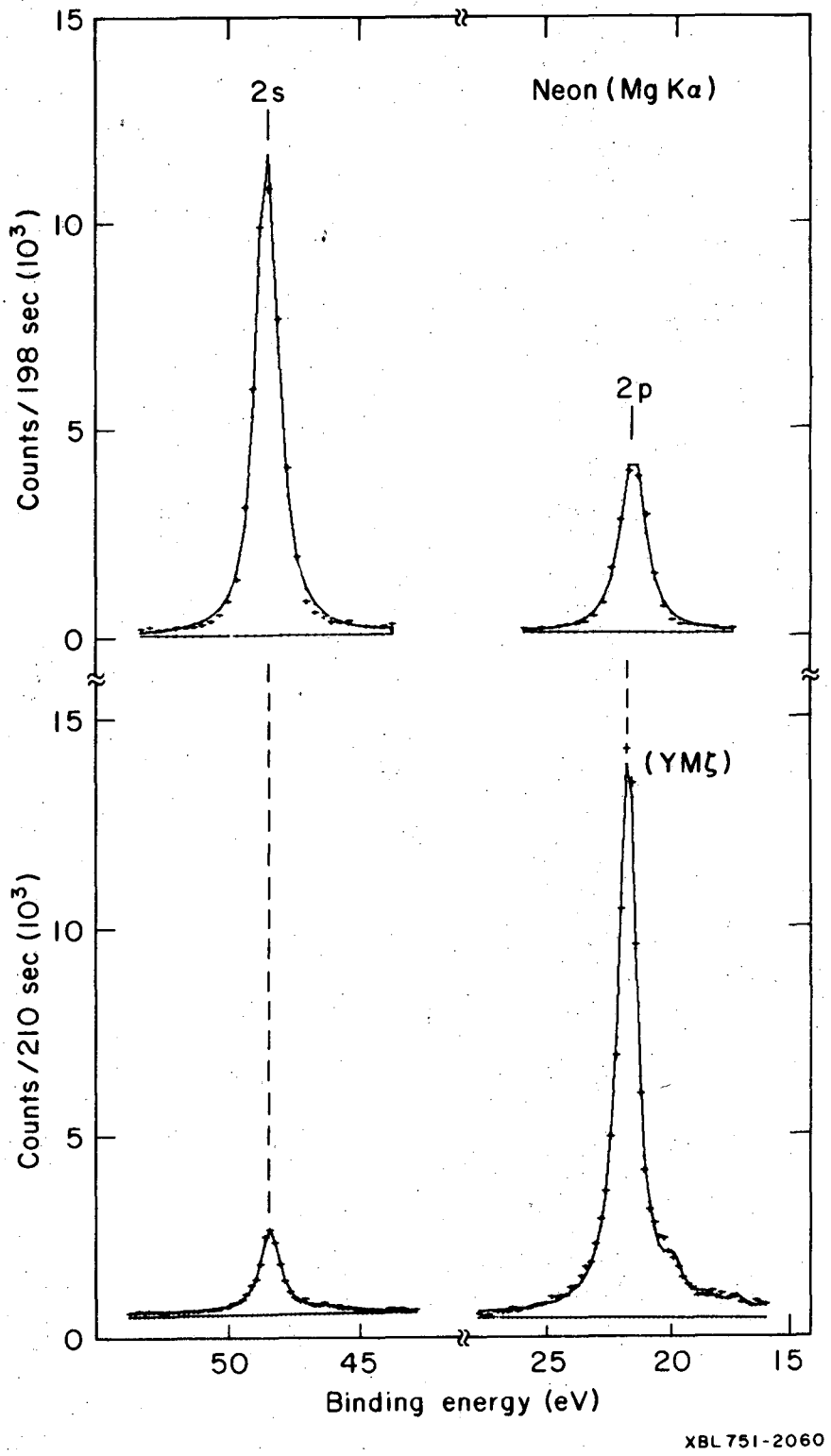

Fig. 32. The Ne2s and 2p levels with MgKα and YMζ.

The intensity ratios at the two energies are compared with other measurements in Table V, after correcting for the variation of spectrometer transmission with energy. The possible change in detector efficiency with electron energy was not taken into account.

TABLE IV. Binding energy separation of the outer s and p subshells of neon, argon and krypton (in eV).

Atom	MgKα	YMζ	MgKα*
Neon	26.69(3)	26.90(1)	26.83(5)
Argon	13.40(3)	13.44(2)	13.5 (1)
Krypton	13.47(3)	13.56(4)	13.3 (2)

*From ref. 37.

This may explain why our ratio is high compared to the value obtained by Wuilleumier and Krause.[9] It must be noted, however, that the background counts in the 2s and 2p regions are comparable, which seems to indicate that there is no marked decrease in detector efficiency at ∿ 80 eV kinetic energy. The p/s ratio at MgKα is in excellent agreement with the measurement of Wuilleumier and Krause.

TABLE V. Valence shell p/s intensity ratios of the rare gases at MgKα and YMζ energies.

	MgKα Relative Intensity			YMζ Relative Intensity	
Atom	This Work	Ref. 37	Other	This Work	Other
Neon	0.42(4)	0.34(2)	0.39(9)*	7.1(3)	6.3(3)*
Argon	1.87(5)	2.0(4)	1.8(1)†	5.3(2)	5.3(2) (ZrMζ)†
Krypton	3.04(5)	2.5(6)	4.7(2)†	2.10(7)	--
Xenon	--	4.0(8)	4.5(2)†	--	--

*Reference 9.
†Reference 10.

2. Argon

As with neon, the two outer subshells were probed with YMζ and MgKα (see Fig. 33). The resulting binding energy separations are listed in Table IV and the area ratios in Table V, where the YMζ (132.3 eV) area ratio is compared with the ZrMζ (151.4 eV) measurement of Spears, Fischbeck and Carlson.[10] It is unlikely that the ratio would change by much over such a small energy range in this region of photon energies. The YMζ 3s peak shows some structure on the high kinetic energy side. As can be seen from Fig. 33, this region was not included in the fit.

Both the binding energy separation and intensity ratio agree very well with previous measurements.

3. Krypton

The MgKα and YMζ spectra of the 4s and 4p subshells are shown in Fig. 34. With YMζ the count rate was low probably due to the small cross section of these levels. The spin-orbit splitting, obtained by constraining the two peaks under the 4p level to an area ratio of 2:1, is .77(3) eV with MgKα and .68(5) eV with YMζ (compare with Moore's value of 0.67 eV).[49]

It is well known[10] that the region below the 4s is rich in satellite peaks. We have repeated the earlier measurement by Spears et al,[10] using MgKα, and the resulting spectrum is shown in Fig. 35. Our yttrium spectrum (Fig. 34) also shows part of the satellite region. It is interesting to note that the intensity of satellites (3 and 4), relative to the 4s level, increases substantially in going from magnesium to yttrium. Spears et al assign the final-state configuration $4s^2 4p^4 5p^1$ to satellite #4 and $4s^2 4p^4 4d^1$ to #3. The first state is described as a shake-up since it

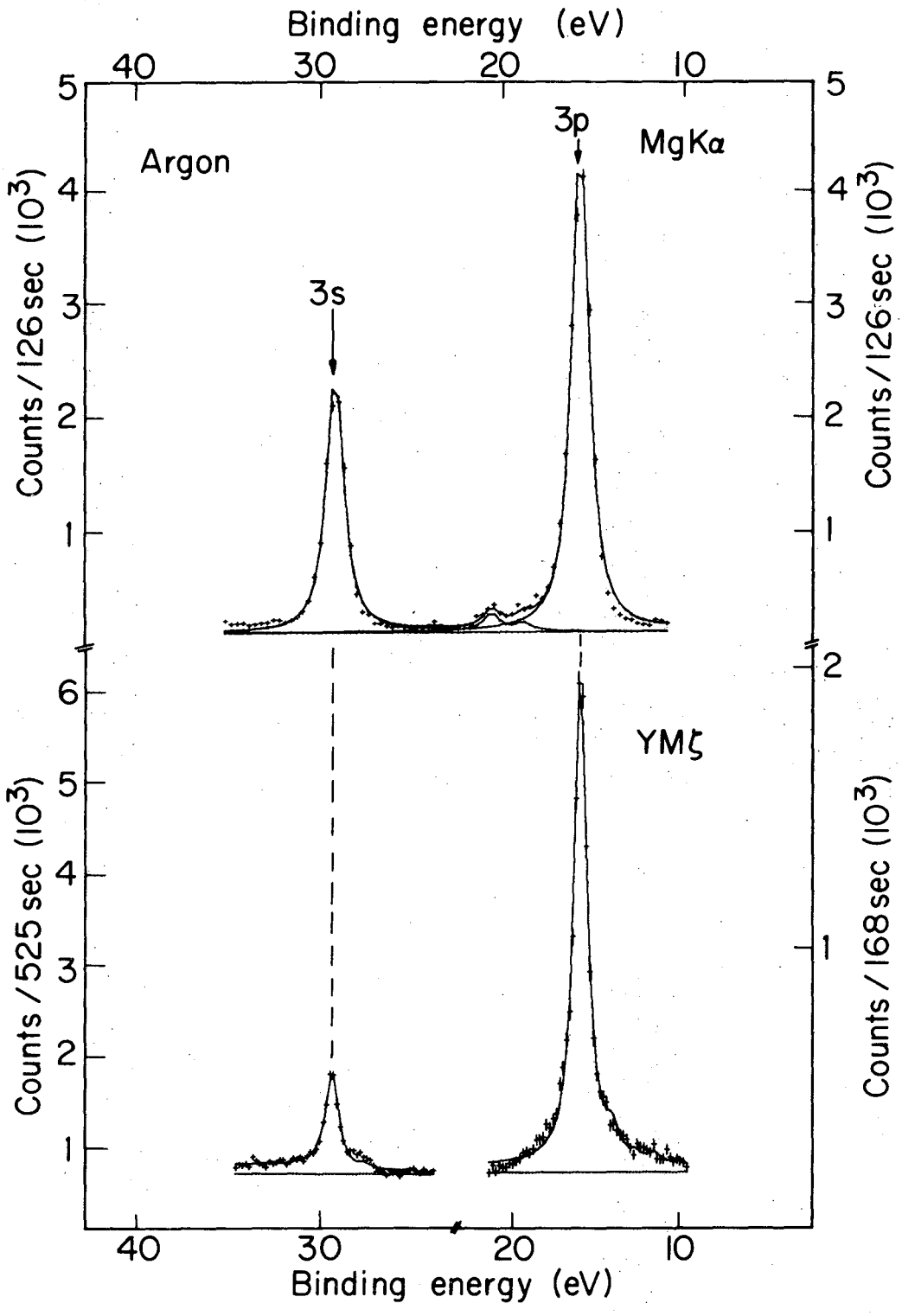

XBL 751-2054

Fig. 33. The argon 3s and 3p levels with MgKα and YMζ.

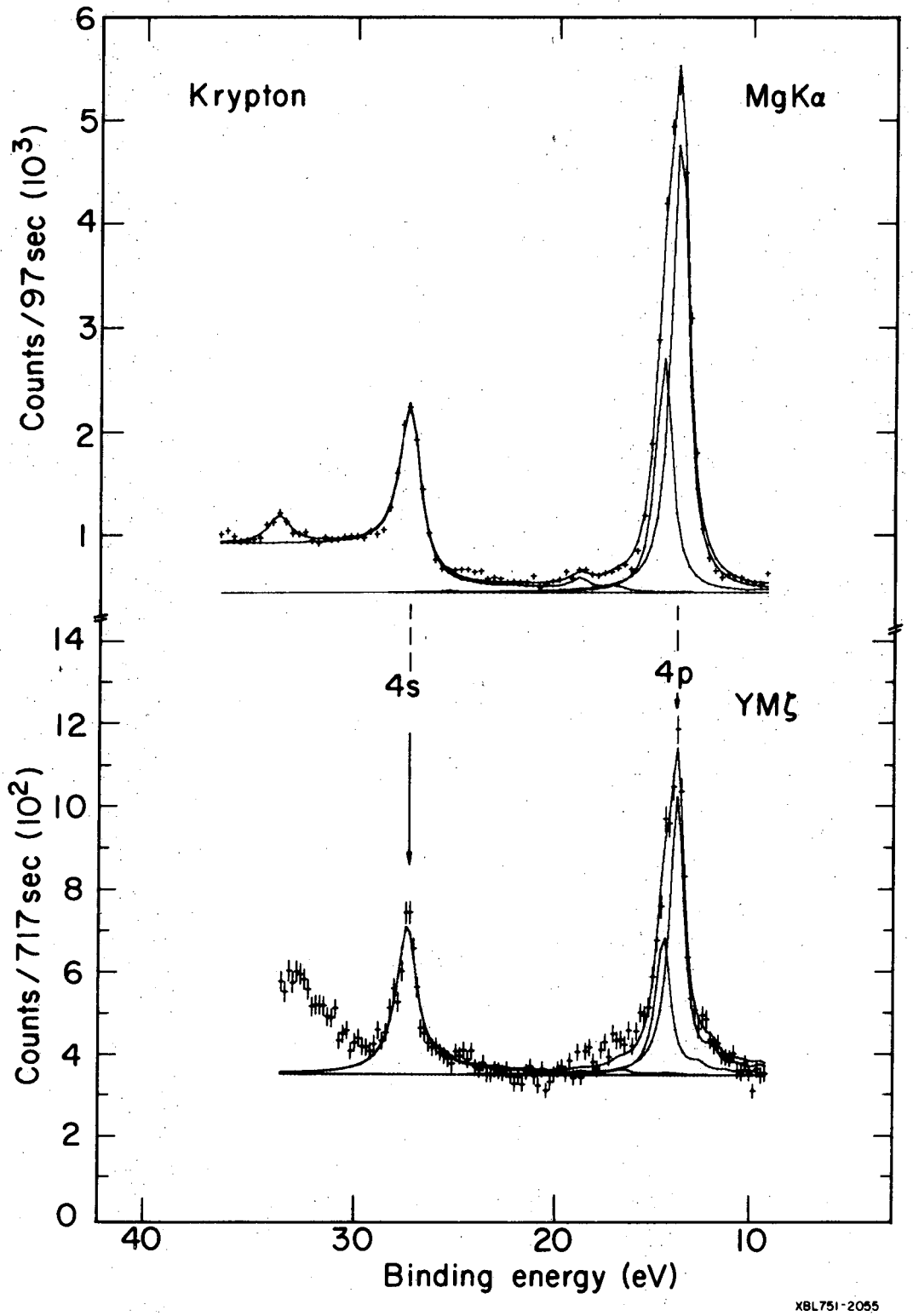

Fig. 34. The krypton 4s and 4p levels with MgKα and YMζ. 4p was fitted with two peaks of area ratio 2:1. MgKα gave a separation of 0.77(3) eV and YMζ 0.68(5) eV.

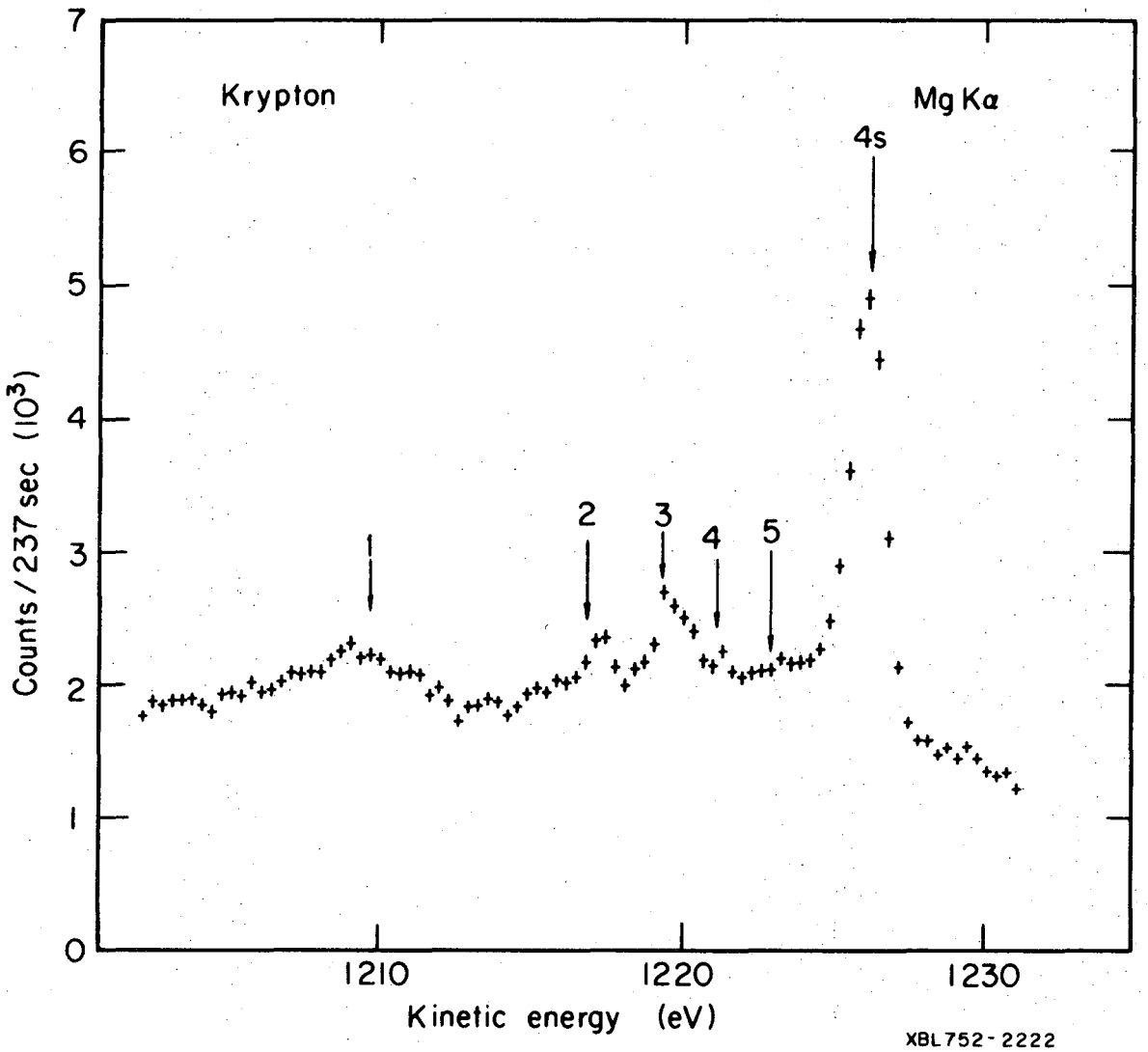

Fig. 35. Krypton 4s and lower kinetic energy region (MgKα). Lines 1, 2 and 5 are probably LMM Augers. Line 3 results from the final state configuration $4s^2 4p^4 4d^1$ and line 4 from $4s^2 4p^4 5p^1$. Some unassigned structure remains. The spectrum is not corrected for the change in spectrometer transmission.

involves a monopole, single electron excitation accompanying 4p ionization. The second is a configuration interaction state, involving a two-electron transition (associated with 4s ionization). It is interesting that the YMζ spectrum appears to support the existence of a state associated with p ionization: the fact that the satellite intensity is greater than the 4s intensity makes it unlikely that the whole structure can originate with 4s ionization.

The remaining numbered peaks (1, 2 and 5) probably correspond to LMM Auger lines. The arrows indicate the kinetic energy values measured by Siegbahn et al.[50] These are 1209.8 eV ($L_3M_{2,3}M_{2,3}$), 1216.9 eV and 1222.9 eV. The authors found, using electron impact, that line #5 is approximately twice as intense as line #2. This is in clear disagreement with our results. Thus if their measurement is correct, it would indicate that line #2 contains contributions due to other transitions.

We have also investigated the 3d region of krypton (Fig. 36). Coincidentally, this region also contains the MNN Auger lines,[50] some of which overlap with the 3d levels. (This explains why $3d_{3/2}$ appears more intense than $3d_{5/2}$.) The arrows in Fig. 36 point to the line positions as determined by Siegbahn et al.[50] The corresponding kinetic energies are collected in Table VI, together with the interpretations of Mehlhorn.[51] According to Burhop and Asaad[52] the lines below $M_5N_1N_{2,3}$ ($^1P_1$) are probably satellites of $M_{4,5}N_1N_{2,3}$, corresponding to the initial state ionization $M_{4,5}N_{2,3}$.

The peak with a designated approximate linewidth of 0.4 eV in Fig. 36 is a composite of three Auger lines having an energy of ∿ 31 eV. This is probably the lowest kinetic energy ever investigated with the Berkeley

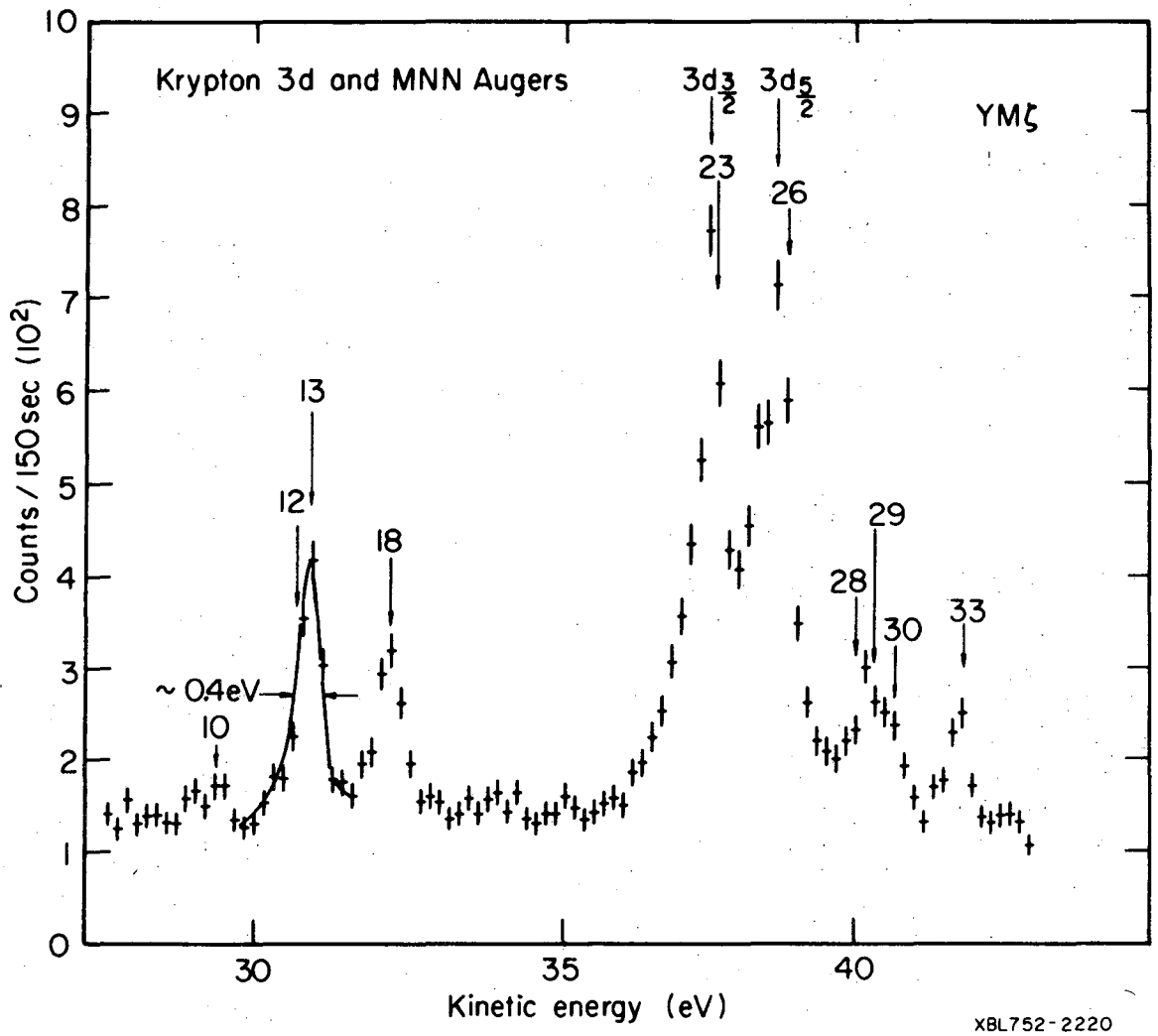

Fig. 36. Krypton 3d and MNN Augers. See Table VI for the energies and assignments of the Auger lines. This spectrum is not corrected for the change in spectrometer transmission.

Iron-Free Spectrometer. The narrow linewidth speaks well for the performance of the magnetic-field compensation system (see Sec. II.A, part 3).

TABLE VI. Some MNN Auger lines of krypton.

Line Number[a]	Kinetic Energy[b] (eV) ± 0.10 (eV)	Transition[c]
10	29.39	
12	30.64	
13	30.89	$M_5N_1N_1(^1S_0)$
18	32.14	$M_4N_1N_1(^1S_0)$
23	37.67	$M_5N_1N_{2,3}(^1P_1)$
26	38.91	$M_4N_1N_{2,3}(^1P_1)$
28	40.19	$M_5N_1N_{2,3}(^3P_0)$
29	40.46	$M_5N_1N_{2,3}(^3P_1)$
30	40.89	$M_5N_1N_{2,3}(^3P_2)$
33	42.14	$M_4N_1N_{2,3}(^3P_2)$

[a]Line numbers the same as in Table B.4, p. 162 of Ref. 37.
[b]From ref. 37.
[c]From refs. 37 and 51.

4. Xenon

We were unable to obtain the 5s and 5p levels with YMζ. The 4d levels, however, are quite intense and are shown in Fig. 37. A spin-orbit splitting of 2.00(2) eV was obtained in excellent agreement with the optical spectroscopy measurement of Codling and Madden[53] (1.97 eV). The

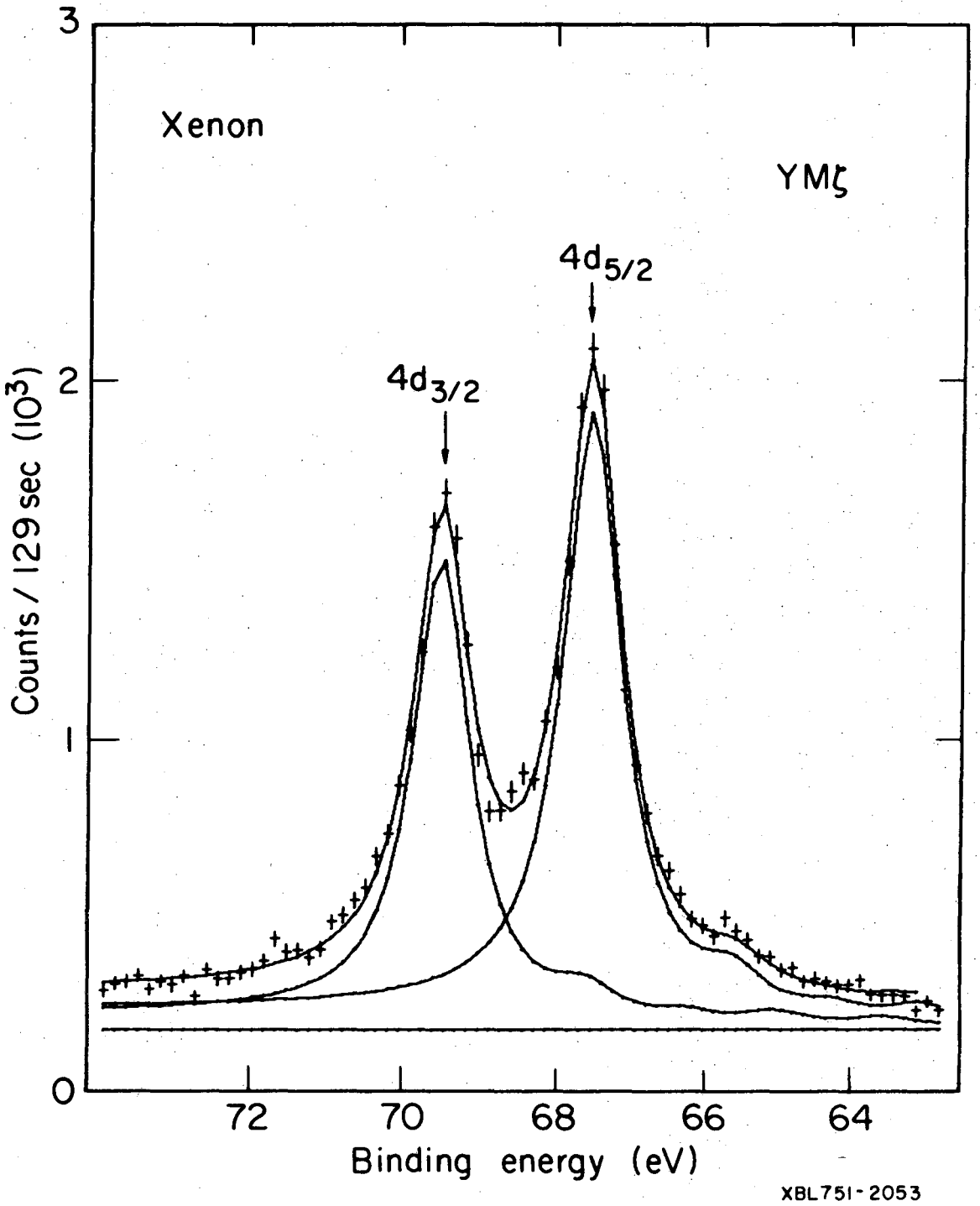

Fig. 37. Xenon 4d levels. Linewidths are 0.91(4) eV for $4d_{3/2}$ and 0.95(3) eV for $4d_{5/2}$. Area ratio is 1:1.36(4).

least-squares fit yields an area ratio of 1.36(4) to 1 instead of the 1.5 to 1 multiplet ratio.

B. *Comparison of Relative Subshell Cross Sections with Theory*

A large number of theoretical papers have dealt with soft x-ray photoionization in recent years. Many include calculations of the photoelectric cross sections of the rare gases. For a review of the literature up to the middle of 1968, the reader is referred to the comprehensive work of Fano and Cooper.[54] Of the more recent calculations,[55] the data of Kennedy and Manson[56] is perhaps most suited for comparison with our experimental results. The theoretical values of Debies and Rabalais[57] for neon will be considered in conjunction with the isoelectronic second-row hydrides (see Section VIII).

To obtain the radial part of the continuum wavefunction, Kennedy and Manson solved the one-electron Hartree-Fock equation assuming a frozen core for the ion with an appropriate $n\ell'$ hole. The same discrete orbitals[58] were used for both the initial and final state. Since the wavefunctions employed were not exact, the dipole-length and dipole-velocity expressions would not be expected to give the same result. Both were therefore computed to check the accuracy of the method. In addition to calculating the total subshell cross sections at photon energies up to 400 eV, Kennedy and Manson also determined β, the anisotropy parameter, as a function of photoelectron energy. β is related to the differential photoionization cross section through the equation

$$(d\sigma/d\Omega)_\theta = (\sigma_{tot}/4\pi)\left[1 - \tfrac{1}{4}\beta\,(3\cos^2\theta - 1)\right] \qquad (6)$$

where θ is the angle between the unpolarized photon beam and the photoejected electron. At 90°, the geometry of our apparatus, we have:

$$\left(\frac{d\sigma}{d\Omega}\right)_{90°} = \sigma_{tot}(1 + \frac{\beta}{4}) \qquad (7)$$

Thus we see that the work of Kennedy and Manson provides us with the necessary data for comparison with our YMζ results. Since the total specific subshell cross sections were tabulated as functions of photoelectron energy, the photon and binding energies were needed. They were obtained from refs. 9 and 37 respectively. The cross sections of interest were interpolated linearly from the tables in ref. 56, where the values are listed at two Rydberg (27.2 eV) intervals. The β's for the p-levels were read from the various figures. The anisotropy parameter for s-shells was assumed equal to two.

The numbers are collected in Table VII and compared to our experimental ratios. For neon the agreement is reasonable. The theoretical p/s ratio is low because, as observed by Krause,[9] the calculation exaggerates the 2s intensity by at least 20% compared to the experimental value. According to Fadley,[59] cross section calculations involving the sudden approximation implicitly include the effect of both the single and multiple electron transitions. It seems that correlation effects are quite important in neon 2s ionization. This is further supported by the success of the model of Amusia et al,[55b,c] which includes correlation, in predicting the correct 2s cross section.

The agreement of the argon p/s ratio with theory is poorer. We are not as confident in this case about the origin of the discrepancy

TABLE VII. Differential photoionization cross sections ($\theta = 90°$) for individual subshells in the rare gases at $h\nu = 132.3$ eV (in megabarns)[a]

Atom	Level	$\sigma_\perp^L$ (Mb)[b]	$\sigma_\perp^V$ (Mb)[b]	$(p/s)^{L}$[c]	$(p/s)^{V}$[c]	$(p/s)_{(exp)}$[c]
Neon[d]	2p	0.280	0.211	5.27	4.30	7.1(3)
	2s	0.0531	0.0491			
Argon[e]	3p	0.0902	0.0760	3.15	3.28	5.3(2)
	3s	0.0286	0.0232			
Krypton[f]	4p	0.0138	0.0124	0.767	0.918	2.10(7)
	4s	0.0180	0.0135			
	3d	0.199	0.171			
Xenon[g]	5p	0.0141	0.0385			
	5s	0.0148	0.0104			
	4d	1.73	0.955			

[a] Theoretical values of subshell cross sections at 132.3 eV were interpolated linearly from the tables in ref. 56. L and V stand for length and velocity formulation respectively.

[b] Theoretical differential cross sections ($\theta = 90°$) at 132.3 eV. Calculated from the subshell cross sections of ref. 56 by means of eq. (7) in text.

[c] Outer p to outer s subshell intensity ratio at 132.3 eV.

[d] 2p asymmetry parameter β interpolated from Fig. 21 of ref. 56 as follows: $\beta_L = 1.45$, $\beta_V = 1.5$.

[e] 3p: $\beta_L = 1.56$ and $\beta_V = 1.5$ from Fig. 24 of ref. 56.

[f] 4p: $\beta_L = 0.13$ and $\beta_V = 0.45$ (Fig. 25 of ref. 56);
3d: $\beta_L = -0.05$ and $\beta_V = -0.1$ (Fig. 22 of ref. 56).

[g] 5p: $\beta_L = -0.07$ and $\beta_V = 0.23$ (Fig. 26 of ref. 56);
4d: $\beta_L = 1.1$ and $\beta_V = 1.2$ (Fig. 27 of ref. 56).

because absolute experimental 3s and 3p cross sections are not available. However, it again seems likely that 3s is overestimated by the calculation. As noted by Krause,[9] correlation in the outer s level is more important in the case of argon and krypton than it is for neon. Thus is is not surprising that the krypton p/s ratio is also in serious disagreement with experiment. Note, however, that theory does predict s to be more intense than p, as found by experiment. (The experimental value in Table V should be divided by 3, since 4p is triply degenerate.) We were unable to measure the exact 3d intensity relative to the outer shells due to the interference of the MNN Auger lines. According to theory, the 3d differential photoionization cross section is roughly an order of magnitude larger than that of 4s or 4p.

The assumption that $\beta = 2$ for xenon 5s may not be valid in view of the work by Walker and Waber.[60] The authors show that when relativistic effects are important, β may depart substantially from its nonrelativistic value. Still, the xenon theoretical differential cross sections in Table VII are interesting to the extent that they show 4d to be $\sim$ 100 times as intense as 5s or 5p. Our experimental observations support this trend: the 4d spectrum was quite intense (Fig. 37) while 5s and 5p were too weak to be observed.

The MgKα and YMζ p/s ratios in Table V show a definite trend. At 132.3 eV (YMζ), the ratio decreases as one goes from neon to krypton. The opposite is true with MgKα. The overlap arguments used by Price et al[6] and Cooper[61] can be adapted to qualitatively explain this trend. For a fixed x-ray energy, let us assume a plane wave for the outgoing electron with a wavelength roughly the same for ionization from s or p

($\sim$ 1.2 Å with YMζ and $\sim$ 0.35 Å with MgKα). At the YMζ energy, this wavelength is such that the outgoing electron wave overlaps better with the diffuse and nodeless 2p orbital of neon than with the contracted 2s orbital. The overlap is proportional to the photoelectric cross section of the orbital in question. As one proceeds to argon, then krypton, the outer p orbital acquires first one then two nodes, which makes for less overlap with the outgoing electron wave. The s orbital, on the other hand, becomes more diffuse as the total number of subshells is increased. A more diffuse s wavefunction overlaps better with the photoejected electron wave.

The situation is reversed at the MgKα energy. The outgoing electron wavelength ($\sim$ 0.35) is shorter than in the yttrium case. Ne2s thus overlaps with it better than Ne2p, but the overlap with s decreases in argon and krypton relative to the overlap with p. The s orbitals match the photoelectron wavelength less as they become more diffuse; the p orbitals match it more as they acquire nodes.

VIII. THE ISOELECTRONIC HYDRIDES CH_4, NH_3, H_2O AND HF

The second row hydrides offer an interesting series of molecules for study by YMζ because they involve a central atom in a relatively simple bonding situation. Further incentive for their study is provided by the recent availability of theoretical cross section values as functions of photon energy.[57] As with the rare gases, we report the molecular orbital spectra with MgKα and YMζ.[62] We also report the intensity of the nitrogen 1s level relative to the molecular orbitals of ammonia.

A. *Experimental*

CH_4, NH_3 and HF were obtained commercially (Matheson Gas Co.). In order to help stabilize the gas flow into the spectrometer, the samples were cooled using standard baths. Methane was cooled in liquid nitrogen, ammonia in a dry ice/acetone bath, and hydrogen fluoride in ice. Water, ammonia and hydrogen fluoride were frozen at liquid nitrogen temperature and pumped on prior to the start of the experiment. Counts were obtained at kinetic energy increments of ∿ 0.3 eV in the magnesium spectra and ∿ 0.2 eV with yttrium. In the former case (except for H_2O), the energies were calibrated using the neon 2s level, at a binding energy of 48.42 eV.[37] The results are shown in Figs. 38 - 40.

Oxidation of the yttrium surface led to broadened lines in some cases. However, it was always possible to distinguish the individual levels and to perform the curve-fitting without constraining the FWHM. Such a constraint could have changed the area ratios somewhat. In the ammonia YMζ spectrum, an interfering structure was observed between the two outer orbitals. Water has intense peaks in that region (see Fig. 40),

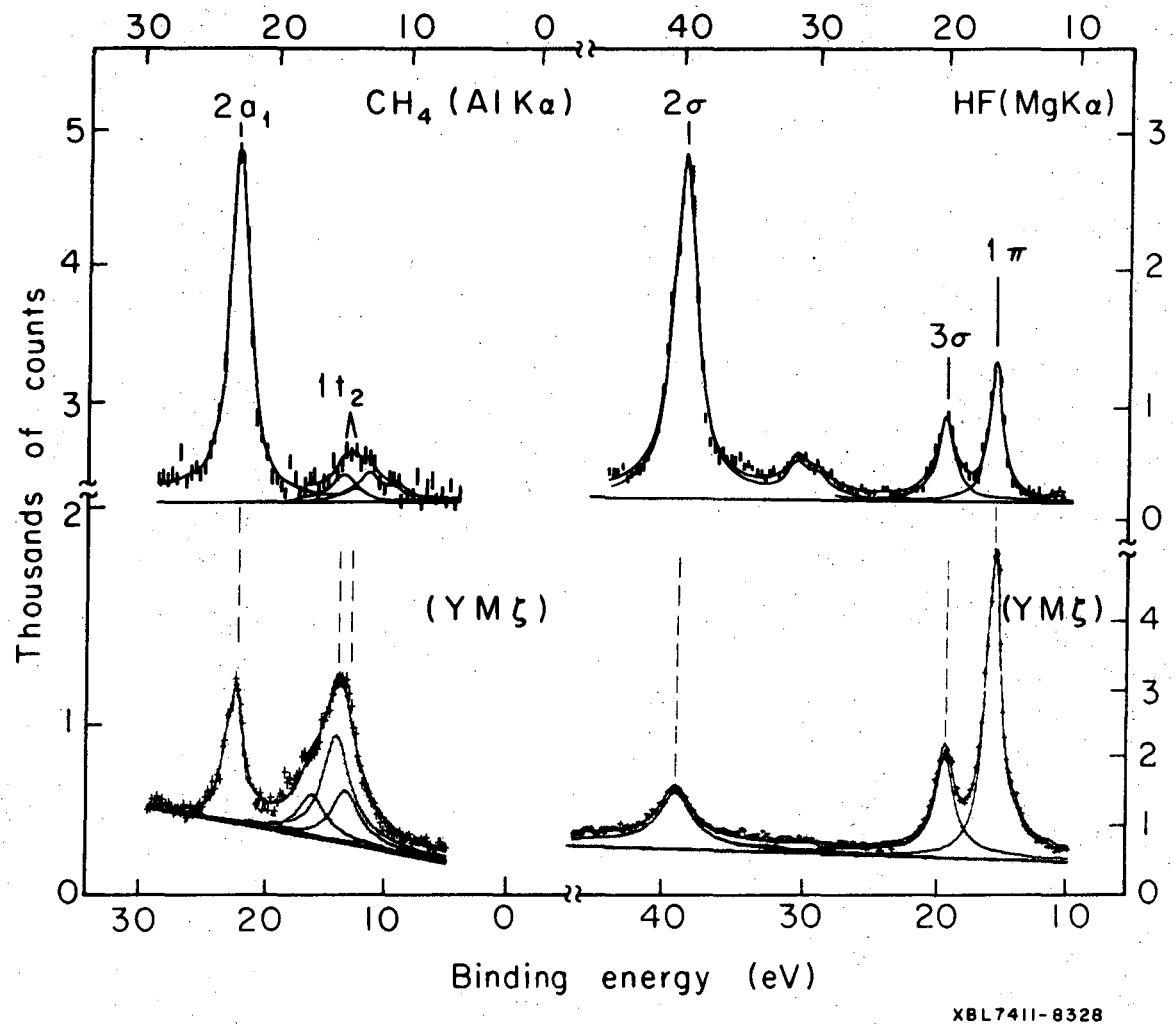

Fig. 38. MgKα spectra (top) and YMζ spectra (bottom) of CH_4 and HF valence orbitals. Counts were obtained at ∿ 0.3 eV (with MgKα) and ∿ 0.2 eV (with YMζ) kinetic energy increments.

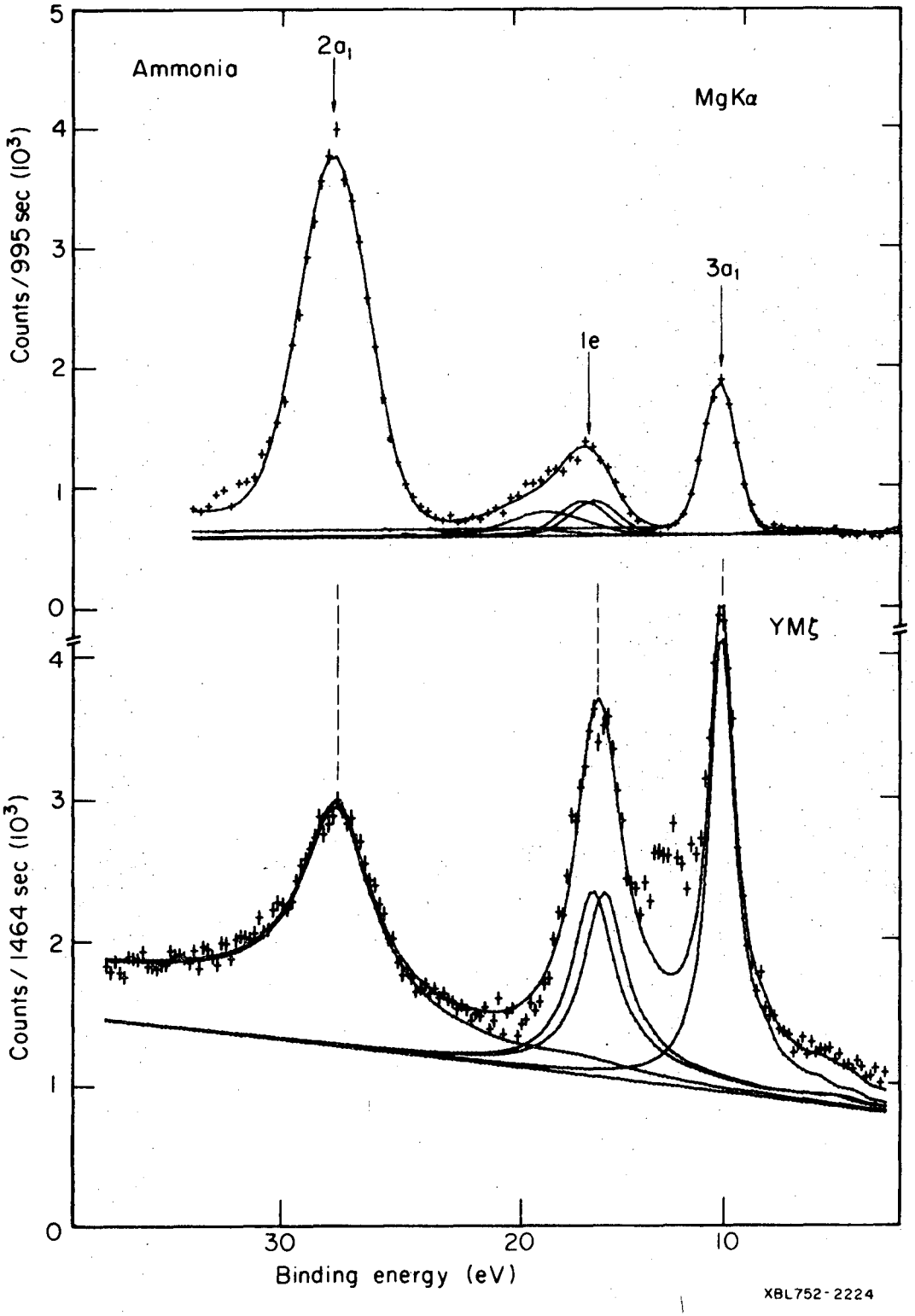

Fig. 39. Ammonia with MgKα (top) and YMζ (bottom). The peak to the left of 1e (MgKα) is a satellite of $2a_1$ resulting from $MgK\alpha_{3,4}$. The structure between 1e and $3a_1$ (YMζ) is due to N1s photoelectrons ejected by OKα x-rays. Oxygen is a contaminant on the anode surface.

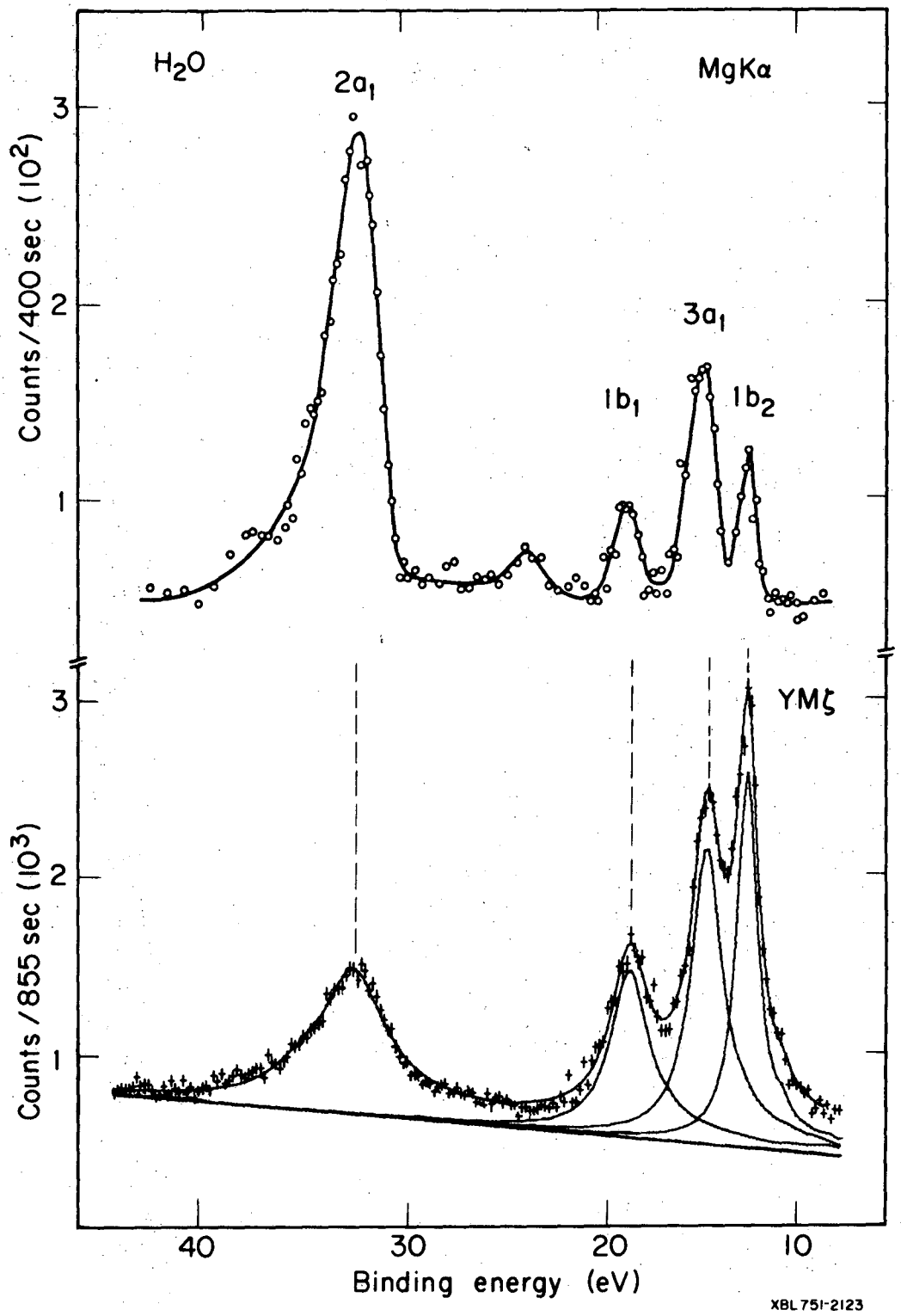

Fig. 40. Water with MgKα (top) and YMζ (bottom). The MgKα spectrum is taken from reference 37.

but its presence was unlikely since the sample was cooled to dry ice temperatures. The kinetic energy of the electrons in the interfering band is ∿ 119 eV. When this is added to the binding energy of nitrogen 1s in ammonia (405.6 eV)[16b] an x-ray energy of ∿ 525 eV is obtained. Thus the most likely interpretation is that the oxide layer on the yttrium surface produces OKα x-rays which eject N1s electrons with an energy falling in the MO region with YMζ x-rays. Future workers with the yttrium source should thus be aware of this type of interference, especially where nitrogen compounds are involved. Fortunately in our case the peaks could be distinguished enough to allow Lorentzians to be fitted to the data points, ignoring the N1s contribution. Interfering x-ray sources of another kind, the $K\alpha_{3,4}$ of magnesium (aluminum in the case of methane) rendered the positions and areas of the $1t_2$ orbital of methane (Fig. 38) and the 1e orbital of ammonia (Fig. 39) somewhat uncertain.

B. *Binding Energies*

The resulting binding energies are listed in Table VIII. Since the YMζ spectra were not referenced, one of the ionization potentials measured with MgKα was used to obtain absolute energies. We also list in Table VIII the results of UPS measurements[63] on the accessible levels of the different hydrides. The binding energies obtained by all three radiation sources are seen to be generally in good agreement. The largest difference between x-ray and UV measurements is in the case of the 1e level of ammonia. We attribute this to the uncertainty introduced by the interfering x-rays discussed above. It was also difficult to determine the mean of the 1e peak because of the flattened summit.[63b]

TABLE VIII. Molecular orbital binding energies of CH_4, NH_3, H_2O, HF and Ne (in eV).

Molecule	Orbital	E_B(MgKα)	E_B(YMζ)	E_B(UPS) [a]
CH_4 [b]	$1t_2$	14.2 (2)	14.5 (1)	14.0
	$2a_1$	23.05(2)	23.05(3) [g]	23.0
NH_3 [c]	$3a_1$	11.04(2)	11.04 [g]	10.85
	1e	16.74(6)	16.49(4)	15.8
	$2a_1$	27.74(2)	27.76(5)	
H_2O [d]	$1b_2$	12.6	12.60 [g]	12.61(6)
	$3a_1$	14.7	14.75(3)	14.73(6)
	$1b_1$	18.4	18.74(4)	18.55
	$2a_1$	32.2	32.61(5)	
HF [e]	1π	16.12(4)	16.12(4) [g]	16.04
	3σ	19.89(7)	19.89(5)	19.90
	2σ	39.65(2)	39.30(4)	--
Ne [f]	2p	21.59		
	2s	48.42(5)		

[a] Vertical ionization potentials.
[b] AlKα values from ref. 65 and UPS values from ref. 63a.
[c] UPS values from ref. 63b.
[d] MgKα values from ref. 37; UPS values from ref. 63c.
[e] MgKα values from ref. 65; UPS values from ref. 63d.
[f] From ref. 37.
[g] Reference value obtained with MgKα (AlKα in the case of methane).

For each hydride except CH_4 the peak corresponding to the deepest lying MO is broader than the rest. The overlap populations between the central atom and the hydrogens in these MO's indicate that they are strongly bonding.[64] This accounts at least partially for the large linewidths. There is also a marked asymmetry on the high binding energy side of the $2a_1$ peaks in water and ammonia which probably reflect the shape of the vibrational envelop composing the peaks.

Calculations[64] show that the $2a_1$ levels are mainly 2s in character. It is interesting to note that their binding energy is a smooth function of the atomic number Z (Fig. 41). The core binding energies correlate similarly with Z, suggesting that, in each case the electrons in the innermost MO are screened from the nucleus by the same amount of charge throughout the hydride series.

The $1t_2$ level of CH_4 and 1e level of NH_3 are known to exhibit Jahn-Teller splitting.[63a,b] A fully split $1t_2$ band should consist of three levels, hence the three-Lorentzian fit in the YMζ spectrum. The area ratios and separatios in this particular case were not unique; our objective was simply to reproduce the overall peak well. The shape of the $1t_2$ band obtained with YMζ is very similar to the UPS result.[63a] For the 1e level of ammonia, a splitting of 0.5 eV was approximated by Turner.[63b] Consequently the 1e level was deconvoluted as two peaks constrained to have equal areas and halfwidths, with a separation of 0.5 eV.

0 0 0 0 4 2 0 6 0 4 8

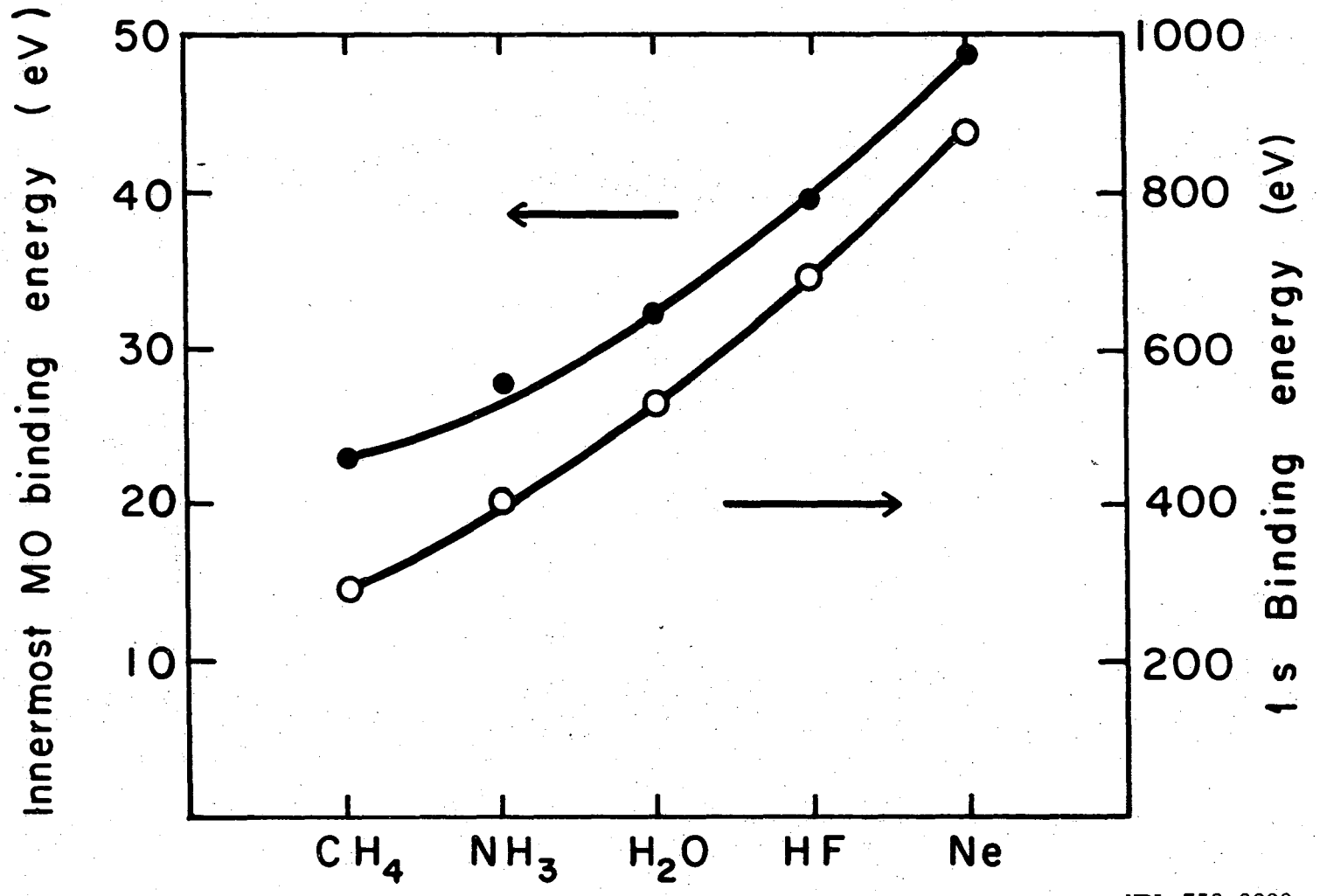

XBL 752-2298

Fig. 41. The binding energy of the innermost MO and of the central atom 1s level in CH_4, NH_3, H_2O, HF and Ne plotted against atomic number. Values are listed in Table IX.

C. *Intensity Ratios*

The same argument employed in the case of the rare gases (Sec. VII.B) can be applied here to account for the cross section variation with photon energy. The photoemission transition probability is proportional to the square of a one-electron momentum matrix element,

$$\text{T.P.} \propto \left| \langle \chi_f(j) \mid \vec{p}_j \mid \phi_i(j) \rangle \right|^2 \tag{8}$$

Here $\phi_i(j)$, $\chi_f(j)$, and $\vec{p}_j$ denote, respectively, the initial bound state, final continuum state, and momentum operator for electron j. The matrix element corresponds very roughly to a Fourier transform of $\phi_i(j)$. It tends, therefore, to be largest when the curvature of $\phi_i(j)$ is such as to yield large Fourier components at the deBroglie wavelength of the outgoing electron continuum state χ. For second-row elements the inner radial nodes of the atomic 2s functions have curvatures that match the wavelength of valence electrons ejected by high energy ($\sim 10^3$ eV) photons, but not those of low energies ($\sim 10^2$ eV). (The wavelength of electrons with these two kinetic energies are 0.39 Å and 1.2 Å respectively.) On the other hand, 2p functions have no nodes and their size matches the low energy electrons better. Thus $\sigma(2s)/\sigma(2p)$ would be expected to decrease dramatically from excitation by $MgK\alpha_{1,2}$ to $YM\zeta$; and as a result of such a change these XPS-MO spectra should reflect atomic orbital composition of each MO.

Inspection of Fig. 38, which compares the $YM\zeta$ and $MgK\alpha_{1,2}$ spectra of CH_4 and HF, shows clearly that these expectations are fulfilled. The intensity ratio $I(2a_1)/I(1t_2)$ in CH_4 drops by a factor of ~ 22 from Mg

to Y energies, confirming the C2s character of the a_1 orbital and the C2p character of the t_2 orbital.

The changes in peak intensities in HF are equally dramatic, and the spectrum is cleaner. We need consider only the fluorine atomic orbitals. The 1π orbital is made up entirely of p functions, with no s admixture, by symmetry. Using the 1π peak as a reference, we note that the 2σ peak intensity drops significantly in going from the magnesium to the yttrium spectrum. This confirms the s character of the 2σ orbital. It sets a very low limit on the atomic $2p\sigma$ contribution. The $3\sigma/1\pi$ intensity ratio also drops, indicating some $2s\sigma$ character, but the decrease is much less dramatic, showing that this orbital is mainly $2p\sigma$ in nature.

The intensity changes with photon energy in ammonia (Fig. 39) and water (Fig. 40) are also in line with the overlap picture. In the YMζ spectrum of water, $1b_2$, which is purely 2p in character, gains substantially relative to the 2s-like $2a_1$ orbital. The 2p contributions to $3a_1$ and $1b_1$ also result in an intensity increase, but the presence of some s character in $3a_1$ makes this increase less dramatic than for $1b_2$. Interestingly, $1b_1$ retains roughly the same intensity relative to $1b_2$ in going from MgKα to YMζ. This behavior would not be expected on the basis of 2p populations alone, since $1b_2$ is totally 2p in character while $1b_1$ is only 60% 2p and 40% hydrogen 1s.[64] One possibility is that the hydrogen 1s cross section increases faster than the oxygen 2p cross section when the photon energy is changed from 1253.6 eV to 132.3 eV. Another more likely explanation is that, since $1b_1$ is strongly O-H bonding,[64] its diffuse electronic population overlaps with the outgoing electron better at 132.3 eV, thus resulting in a cross section that is higher than

would be expected on the basis of 2p population alone. Similarly in ammonia, one of the 1e orbitals is strongly N-H bonding.[64] From Fig. 39 it can be seen that 1e becomes more intense than $3a_1$ at the YMζ energy, despite the fact that $3a_1$ is 90% 2p while 1e is only 60% 2p. Both 1e and $3a_1$ gain with respect to $2a_1$ at low photon energy, as expected.

In columns 4, 6, 8 and 9 of Table IX we compare, respectively, the hydride area ratios at 21.2 eV (HeI), 40.8 eV (HeII), 132.3 eV (YMζ) and 1253.6 eV ($MgK\alpha_{1,2}$) exciting photon energies, from which it is seen that the relative intensities obtained with helium resonance lines are generally quite similar to the values obtained with YMζ. Furthermore, orbital ordering is the same with all three sources. These observations are in line with the overlap picture discussed above, since, as with YMζ, the wavelengths of electrons ejected with the helium lines match 2p orbitals better than 2s.

The simple model proposed by Gelius[36] is useful in this context. According to this model, the photoelectric cross section at high photon energies (roughly 1000 eV and above) for electrons in molecular orbital i is related to the atomic-orbital cross section as follows

$$\sigma_i(\mathrm{MO}) \simeq \sum_j P_{ij}\, \sigma_j(\mathrm{AO}) \quad . \tag{9}$$

Here P_{ij} is the electron population in AO ϕ_j, for molecular orbital i. Equation (9) probably becomes less accurate as the photon energy is reduced.[36] Still, we considered it useful to obtain a set of semi-empirical σ_{2p}/σ_{2s} ratios for the central atoms of the hydrides under study. We therefore used gross populations obtained from the wavefunctions of Snyder and Basch[64] and the area ratios listed in Table IX to obtain

0 0 0 0 4 2 0 6 0 5 0

TABLE IX. Differential photoionization cross section ratios at 21.2 eV, 40.8 eV, 132.3 eV, and 1253.6 eV excitation energy (θ = 90°)

Molecule	MO	E_B(eV) [a]	I_{exp}(MgKα)	I_{theo}(MgKα) [b]	I_{exp}(YMζ)	I_{theo}(YMζ) [b]	I_{exp}(HeII) [b]	I_{exp}(HeI) [b]
CH_4 [c]	$1t_2$	14.2 (2)	0.12(2)	0.052	2.69(7)	7.54	7.14	
	$2a_1$	23.05(2)	1.00	1.00	1.00	1.00	1.00	
	$1a_1$	290.8 [d]	30(1)	26.41	--	--	--	
NH_3	$3a_1$	11.04(2)	0.20(3)	0.020	0.81(5)	22.27	0.81	0.81
	1e	16.74(6)	0.13(4)	0.038	1.04(4)	18.71	1.54	1.78
	$2a_1$	27.74(2)	1.00	1.00	1.00	1.00	--	--
	$1a_1$	405.6 [d]	33(1)	24.11	--	--	--	--
H_2O	$1b_2$	12.6 [d]	0.095 [f]	0.040	0.92(5)	32.38	0.92	0.92
	$3a_1$	14.7 [d]	0.26 [f]	0.222	1.04(6)	20.56	0.96	1.08
	$1b_1$	18.4 [d]	0.081 [f]	0.020	0.70(5)	12.56	0.77	0.92
	$2a_1$	32.2 [d]	1.00 [f]	1.00	1.00	1.00	--	--
	$1a_1$	539.7 [d]	19 [f]	19.28	--	--	--	--
HF	1π	16.12(4)	0.24(2)	0.122	2.93(4)	23.30	2.93	
	3σ	19.89(7)	0.19(3)	0.167	1.18(5)	6.33	1.20	
	2σ	39.65(2)	1.00	1.00	1.00	1.00		
	1σ	694.0 [e]	34(1)	12.70	--	--		
Ne	2p	21.59 [d]	0.42(4)	0.26	7.11(2)	8.20		
	2s	48.42(5) [d]	1.00	1.00	1.00	1.00		
	1s	870.2 (1) [d]		10.54	--	--		

Footnotes to Table IX

[a] MgKα values for all except $1t_2$ and $2a_1$ of CH_4, which were measured using AlKα.

[b] Ref. 57; theoretical results were kindly communicated to us by J. W. Rabalais.

[c] AlKα used instead of MgKα in obtaining the experimental ratios.

[d] Ref. 37.

[e] B. E. Mills, private communication.

[f] Calculated by the authors of Ref. 57 from the spectrum in Ref. 37.

cross section ratios at both the magnesium and yttrium energies. The hydrogen 1s cross section was taken equal to zero in all cases, since we found it impossible to obtain a spectrum of hydrogen 1s with either MgKα or YMζ. The four s functions used in the double zeta basis set of Snyder and Basch were not separated into 1s and 2s contributions. All four were considered 2s in the analysis of the MO spectra. For each hydride, one area ratio of two MO's is needed (in conjunction with the appropriate gross populations) to obtain σ_{2p}/σ_{2s}. We have used the area ratios of $2a_1$ to each of the remaining MO's (Table IX) to obtain more than one value of each of the atomic cross section ratios (except C_{2p}/C_{2s}, since methane has only two MO's). The results, listed in Table X, are an average of the different obtainable ratios.

The ratios at the MgKα energy (AlKα in the case of methane) are compared to the theoretical ratios of Huang and Ellison[66] and Nefedov et al.[67] The former assumed a plane wave for the outgoing electron, employing Slater-type orbitals orthogonalized to the 1s core,[66a] or SCF Clementi atomic orbitals (CAO),[66b] to represent the bound orbitals. The CAO results are in excellent agreement with our semiempirical calculations. Slater-type orbitals yield ratios that are somewhat smaller than ours, but the agreement is still good. We note that the SCF relativistic Hartree-Fock-Slater calculations of Nefedov et al[67] (Table X) represent ratios of *total* (as opposed to differential) 2p-to-2s cross sections. However, as the authors point out, the correction in this case is small (a factor of 1.00 - 1.08). It should also be noted that the oxygen and fluorine ratios of Nefedov et al. were computed for O^- and F^-, respectively, instead of the neutral species.

TABLE X. Relative photoelectric cross section ratios ($\sigma_\perp 2p/\sigma_\perp 2s$) for second row atoms. [a]

Atom	R [b] (132 eV)	R [b] (1254 eV)	R (STO) [c] (1254 eV)	R (CAO) [d] (1254 eV)	R [e] (1254 eV)
C	1.16	0.052 [f]	0.012	0.048	0.032 [f]
N	0.66	0.083	0.023	0.077	0.058
O	0.90	0.11	0.042	0.11	0.070
F	1.39	0.13	0.077	0.17	0.098
Ne	2.37	0.14 [g]	0.12	0.25	0.14

[a] To take the 2p degeneracy into account, all ratios in this Table must be multipled by 3.

[b] Semiempirical ratios calculated using Eq. (9). Gross populations were calculated from Ref. 64 and area ratios from Table IX.

[c] From Ref. 66a; Slater-type orbitals were used to represent the occupied orbitals, with 2s orthogonalized to the 1s AO. The continuum state was represented by a plane wave.

[d] From Ref. 66b; SCF Clementi atomic orbitals used instead of STO's.

[e] Theoretical *total* cross section ratios using a Hartree-Fock-Slater potential (Ref. 67). Oxygen and fluorine cross sections were computed for O^- and F^- respectively, the rest for the neutral species.

[f] Cross section ratio at 1487 eV photon energy.

[g] Experimental value.

The four sets of MgKα ratios listed in Table X all indicate that σ_{2p}/σ_{2s} increases in going across the periodic table from carbon to neon. At the YMζ energy, the ratios do not appear to change monotonically with atomic number, but the general trend seems to be the same as that at the MgKα energy. The YMζ values are generally much closer to unity than the MgKα values. Thus the YMζ energy seems to fall in a region where the 2s and 2p intensities are about equal.

In columns 5 and 7 of Table IX we list the theoretical molecular orbital area ratios of Debies and Rabalais.[57] The calculations are based on the equations derived by Ellison,[68] again employing a plane wave for the continuum electron and the frozen orbital approximation for the remaining ion. *Ab initio* molecular wave functions with minimal basis sets of nonorthogonal Slater-type orbitals were used. Orbital exponents were chosen according to Slater's rules. The computations correctly predict that the intensity ordering of the $2a_1$ and $1t_2$ levels of methane is reversed in going from the MgKα to the YMζ excitation energy (Fig. 38). The correct intensity ordering at 1254 eV is also predicted for ammonia. However, at the YMζ energy, $3a_1$ is calculated to have a slightly higher intensity than 1e, contrary to the experimental result. Similarly, the calculation reverses the intensity order of the outer two MO's of water at 132 eV. It is interesting to note that if peak *heights* were compared instead of peak areas, the calculations would yield the correct intensity ordering, both in water and in ammonia. In HF, however, the wrong order is predicted for the outer two MO's at the MgKα energy. The theoretical fluorine 1s intensity also compares poorly with the experimental value. Finally, the neon 2p/2s relative intensity agrees

quite well with experiment, both at 132 eV and 1254 eV excitation energies.

As shown by Fadley,[59] the assumption that the orbitals of the ion remain frozen during ionization, invoked in the present calculations, leads to cross sections which include the probability for multiple as well as single electron excitations (see Sec. VII.B. for a similar discussion). In the case of the hydrides, one observes no intense satellite peaks in the MO region. Core ionization, however, is often accompanied by multiple electron transitions. In hydrogen fluoride, for example, the probability for multiple electron transitions is $\sim$ 20% of the probability for single electron ionization.[69] The core spectrum of neon is known to contain discrete satellites totaling $\sim$ 12% of the main line. Addition of multiple-electron intensities to the core intensities of these two systems widens the gap between the experimental and theoretical ratios.

In general, the theoretical results are in better agreement with experiment at 1254 eV than at 132 eV. This is not surprising, since the plane wave approximation becomes better the higher the electron energy. For all the hydrides as well as neon, the intensity of the 2p-like to the 2s-like orbitals seem to be overestimated at the YMζ energy and underestimated at the MgKα energy.

IX. NITROGEN, CARBON MONOXIDE, ETHYLENE AND OXYGEN

We continue our investigation of small molecules by considering three more systems for which theoretical cross sections are available: nitrogen, carbon monoxide, and ethylene. The calculations were performed by Rabalais et al.[70] and are similar in quality to the hydride cross sections considered in the previous section. The last part of this section deals with the molecular orbital spectrum of oxygen up to ∿ 30 eV binding energy. Oxygen presents an interesting case for study by XPS because of multiplet splitting (see Sec. VI.A. for a discussion of the core spectrum).

A. *Nitrogen and Carbon Monoxide*

The YMζ spectra are shown in Figs. 42 and 43, together with the magnesium results of Siegbahn et al.[37] As in the case of ammonia, nitrogen 1s photoelectrons excited by OKα x-rays are expected to appear in the YMζ MO spectrum, primarily under the $1\pi_u$ and $2\sigma_u$ peaks. Since the outer three peaks of nitrogen are well resolved, it seems that oxidation was insignificant in this particular run. The region of the spectrum corresponding to higher binding energy is taken from a separate run. Thus the ratio of the innermost MO to the outer three is approximate.

Satellite structure was observed in both nitrogen and carbon monoxide, part of which appears to overlap with the peak corresponding to the deepest lying MO. The satellite at ∿ 25 eV binding energy in the nitrogen spectrum was assigned by Siegbahn et al.[37] as a shake-up state associated with the $2\sigma_u$ level. The monochromatized AlKα spectrum of carbon monoxide[1] shows three satellite bands at ∿ 24, ∿ 28 and ∿ 32 eV binding energy. These are visible in the YMζ spectrum (Fig. 43), though

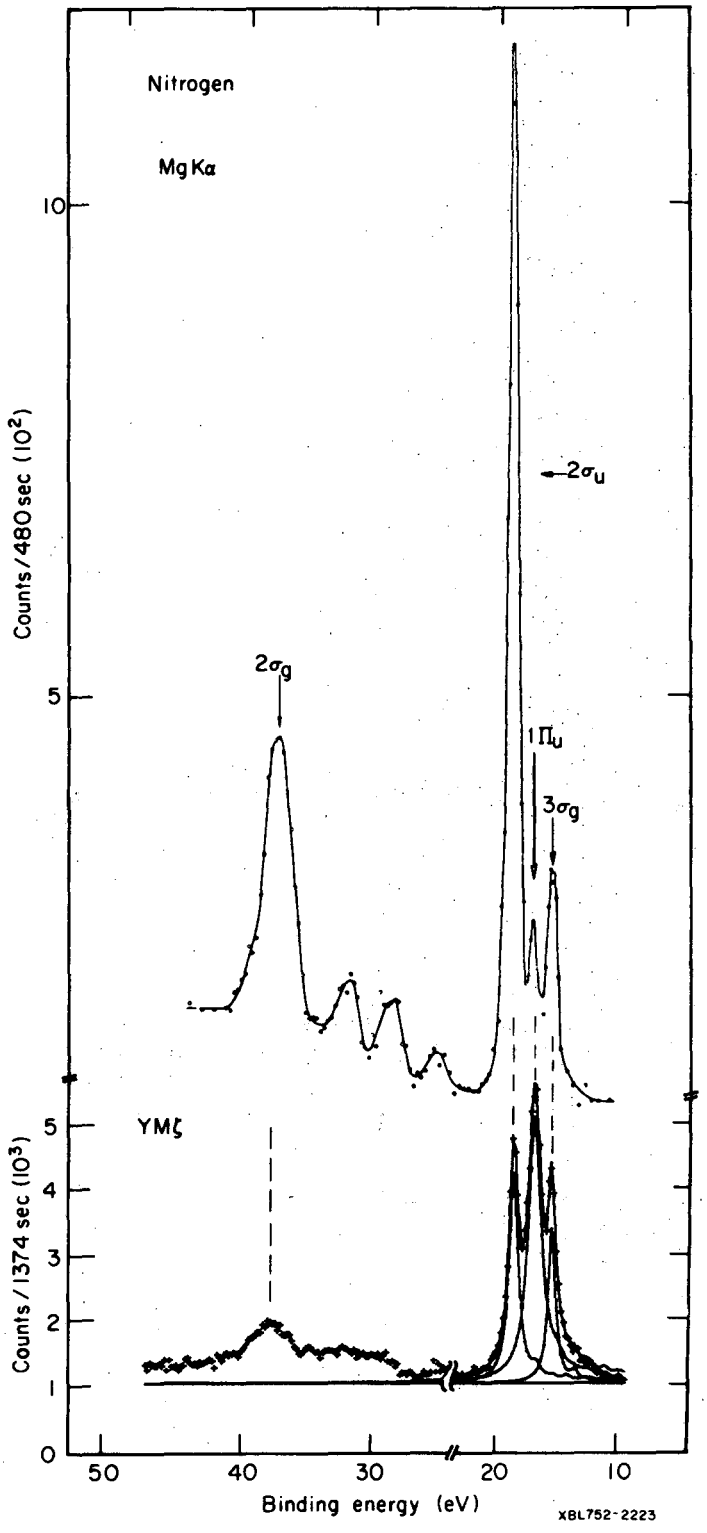

Fig. 42. Nitrogen with MgKα (top) and YMζ (bottom). MgKα spectrum is taken from reference 37. The ratio of the outer three MO's to the innermost (YMζ spectrum) is approximate since the two regions were not scanned simultaneously.

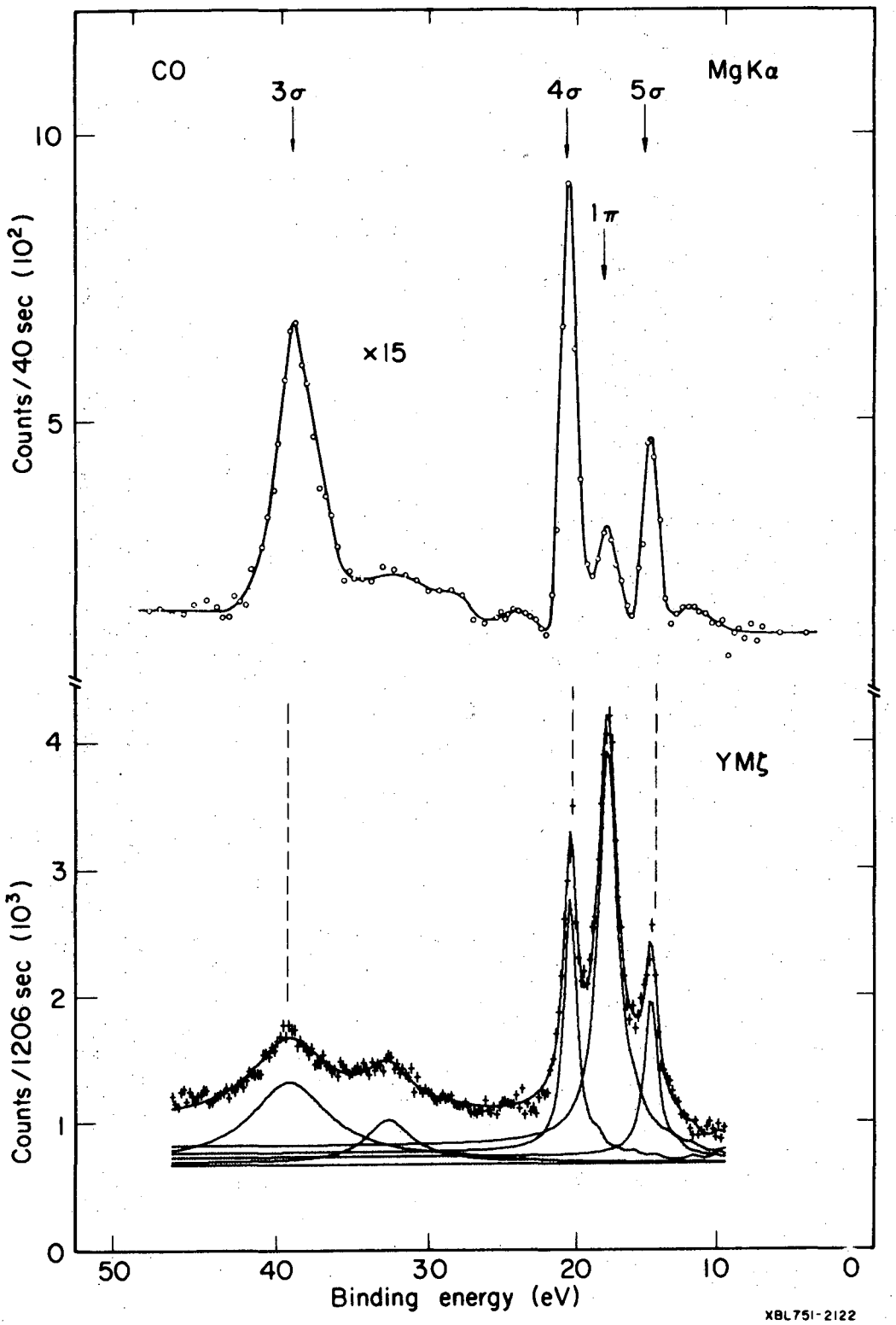

Fig. 43. Carbon monoxide with MgKα (top) and YMζ (bottom). MgKα spectrum is taken from reference 37.

not as clearly. Only the satellite at ∿ 32 eV was fitted with a separate peak. Judging from its intensity in the YMζ spectrum, this satellite appears to be associated with transitions involving the outer three orbitals.

We observe that the qualitative changes in cross section in going from MgKα to YMζ excitation are similar to those observed in the hydride series. The level composed entirely of p orbitals ($1\pi_u$ in nitrogen and 1π in carbon monoxide) gains substantially in intensity at the YMζ energy relative to the deep-lying (s-like) σ MO. The intensity change in orbitals of mixed (s and p) parentage is again seen to be intermediate between those orbitals of predominantly s or p composition.

In Table XI we compare the area ratios at the MgKα and the YMζ energy with the theoretical results of Rabalais et al,[70] who also determined the experimental magnesium intensities from Siegbahn's[37] spectra.

We note that the intensity ordering of the outer three MO's is predicted correctly by the calculations, both for CO and N_2. The experimental intensity ratio of the nitrogen 1s level was not corrected for the change in spectrometer transmission with energy. For a magnetic spectrometer, the change is substantial, in this case being close to 50% (using the intensity of the MO's as a reference). This would bring the experimental value into very good agreement with theory. However, a similar correction on the core-level intensities of carbon monoxide would result in less agreement with theory.

The HeI and HeII experimental intensity ratios[70] listed in Table XI are again similar to the relative areas at the YMζ energy, and the orbital intensity ordering is the same with all three sources.

0 0 0 0 4 2 0 6 0 5 5

TABLE XI. Relative differential photoionization cross sections for nitrogen and carbon monoxide.

	Orbital	E_B(eV) [a]	I_{exp}(MgKα) [b]	I_{theo}(MgKα) [c]	I_{exp}(YMζ)	I_{theo}(YMζ) [c]	I_{exp}(HeII) [c]	I_{exp}(HeI) [c]
N_2	$3\sigma_g$ [d]	15.5	1.00	1.00	1.00	1.00	1.00	1.00
	$1\pi_u$	16.8	0.50	0.22	3.03(7)	1.64	2.1	1.4
	$2\sigma_u$	18.6	5.0	4.96	1.68(7)	0.14	0.47	0.32
	$2\sigma_g$	37.3	3.50	5.23	∿2	0.20		
	$1\sigma_u, 1\sigma_g$	409.9	145	193.44	--	--		
CO	5σ [e]	14.5	1.00	1.00	1.00	1.00	1.00	1.00
	1π	17.2	0.5	0.31	3.44(7)	1.88	3.85	1.25
	4σ	20.1	2.5	1.63	1.46(7)	1.65	2.00	0.26
	3σ	38.3	5.0	5.15	2.33(9)	0.36		
	2σ	295.9	55	45.36	--	--		
	1σ	542.1	120	92.73	--	--		

[a] From Ref. 37.

[b] Experimental area ratios determined by Rabalais et al.[70] from the spectra in Ref. 37.

[c] Ref. 70; YMζ values communicated to us by J. W. Rabalais.

[d] Theoretical $\sigma_\perp$ at 132 eV is 5.43×10^{-20} cm^2 and 7.32×10^{-23} cm^2 at 1254 eV.

[e] Theoretical $\sigma_\perp$ is 3.04×10^{-20} cm^2 at 132 eV and 9.81×10^{-23} cm^2 at 1254 eV.

Carbon monoxide and nitrogen are of course isoelectronic, and it is interesting to note the similarity between their spectra, both at the YMζ and the MgKα energy. It is also apparent from the monochromatized AlKα results[1] that the satellites between ∿ 22 eV and ∿ 35 eV have similar binding energies and relative intensities in both molecules. Our YMζ results reflect a change in the appearance of these satellites. This may or may not be significant since the extent of contributions from inelastic scattering was not assessed in this case.

B. *Ethylene*

The MgKα and YMζ spectra are shown in Fig. 44. With MgKα, the outer four orbitals are very weak. There is also the problem of interference from the $K\alpha_{3,4}$ satellites of the more intense $2a_g$ and $2b_{3u}$ levels. Consequently, the close-lying $1b_{2u}$, $3a_g$ and $1b_{1g}$ could not be distinguished clearly. The arrows in the figure point to their expected peak positions on the basis of UPS results.[72] Only one peak was employed in the least-squares fit to represent all these MO's. On the other hand, the monochromatized AlKα spectrum[71] shows the individual levels, but their areas appear somewhat uncertain due to the low intensity. Robin et al[72] determined the orbital ordering from *ab initio* calculations. His results were confirmed by Gelius,[71] using the model described in Sec. VIII.C.

The MgKα spectrum was reference to neon 2s. However, only the binding energies of the three intense peaks in the spectrum could be determined accurately. The values are listed in Table XII, together with the UPS results of the remaining MO's. With YMζ, we were able to distinguish $1b_{1g}$, but $1b_{2u}$ and $3a_g$ again could not be meaninfully separated.

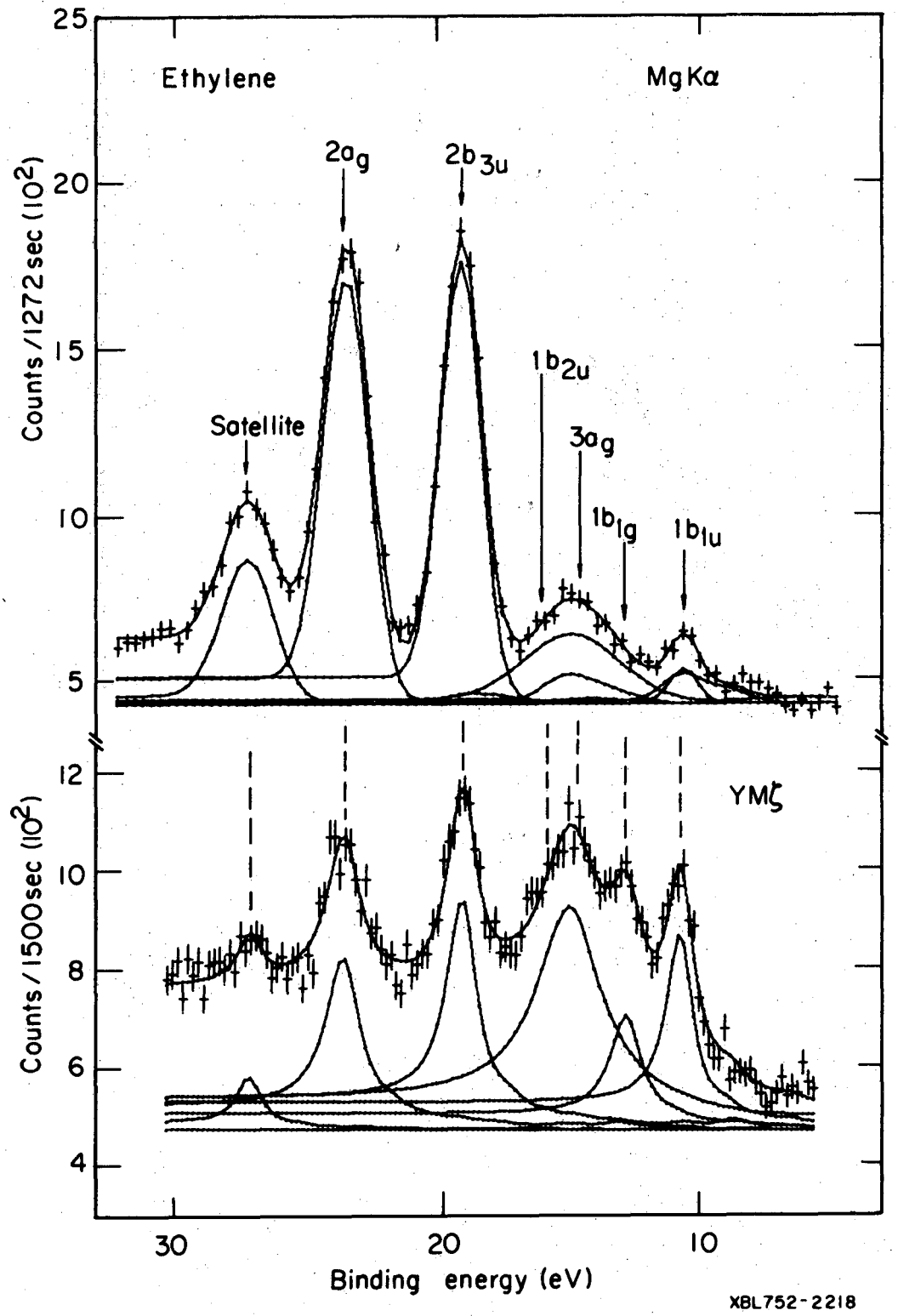

Fig. 44. Ethylene with MgKα (top) and YMζ (bottom). The satellite in the MgKα spectrum is 0.39(6) the intensity of $2b_{3u}$ with a FWHM of 2.3(1) eV. FWHM is 2.02(4) eV for $2a_g$ and 1.81(4) for $2b_{3u}$.

TABLE XII. Ethylene binding energies and differential photoionization cross section ratios.

Orbital	E_B(eV)	I_{exp}(MgKα)	I_{theo}(MgKα)[a]	I_{exp}(YMζ)	I_{theo}(YMζ)[a]	I_{exp}(HeII)[a]	I_{exp}(HeI)[a]
$1b_{1u}$	10.51(4)[c]	0.05(2)	0.015	0.9(2)	4.42	0.9	0.9
$1b_{1g}$	12.85[c]	--	0.017	0.6(4)	2.20	1.12	1.31
$3a_g$	14.66[c]	0.35(9)	0.033	--	1.96	1.33	1.41
		$(1b_{1g} + 3a_g + 1b_{2u})$		2.4(2)			
$1b_{2u}$	15.87[c]	--	0.023	$(3a_g + 1b_{2u})$	1.84	1.02	0.89
$2b_{3u}$	19.23(2)	0.93(3)	0.68	1.2(1)	1.34	0.21	0.20
$2a_g$[b]	23.65(2)	1.00	1.00	1.00	1.00	0.24	
MO shake-up	27.39(5)	0.39(6)	--	0.2(4)	--		
$1a_g, 1b_{3u}$	290.7[d]	69.98(3)	43.6	--	--		
core shake-up	299.10(7)	14.87(9)	--	--	--		

[a] Reference 70; theoretical values communicated to us by J. W. Rabalais.

[b] Theoretical $\sigma_\perp$ at 132 eV is 5.83×10^{-21} cm^2 and 2.00×10^{-22} cm^2 at 1254 eV.

[c] UPS results of Ref. 72.

[d] Reference 16a.

In both spectra a satellite was observed at ∿ 27 eV, which had been obtained earlier with filtered AlKα radiation. The MgKα results indicate that it must be largely, if not entirely, associated with $2a_g$ or $2b_{3u}$, judging from its high intensity. Gelius[71] also cited its high energy as an indication that it does not originate from any of the outer four MO's. The possibility of it being due to an energy loss is ruled out since then two satellites of nearly equal intensity would be expected, corresponding to transitions in neutral ethylene induced by electrons from $2b_{3u}$ and $2a_g$.

A satellite was also observed in the core spectrum (Fig. 45). The core region was scanned alternately with the MO region, in order to obtain relative intensities. Of course, the core satellite must be treated with care, since the possibility of energy loss cannot immediately be ruled out. It was studied with AlKα and at two different pressures. No change in intensity relative to the main peak, or in position was detected. Our ethylene sample was c.p. grade, with a stated purity of at least 99.5%. A carbon containing impurity with such a C1s binding energy (C1s of ethylene plus 8.4 eV) almost certainly contains fluorine. However, none could be detected when the F1s region was monitored. We therefore believe that the satellite corresponds to a state of ionized ethylene. The sloping background on the high binding energy side of Fig. 45 indicates that more structure may be present at higher binding energies. A preliminary run with AlKα showed this to be the case. However, the pressure dependence of those peaks was not examined.

It is interesting to note that the MO satellite is 8.13 eV away from $2b_{3u}$, which is close to the core satellite separation from the main

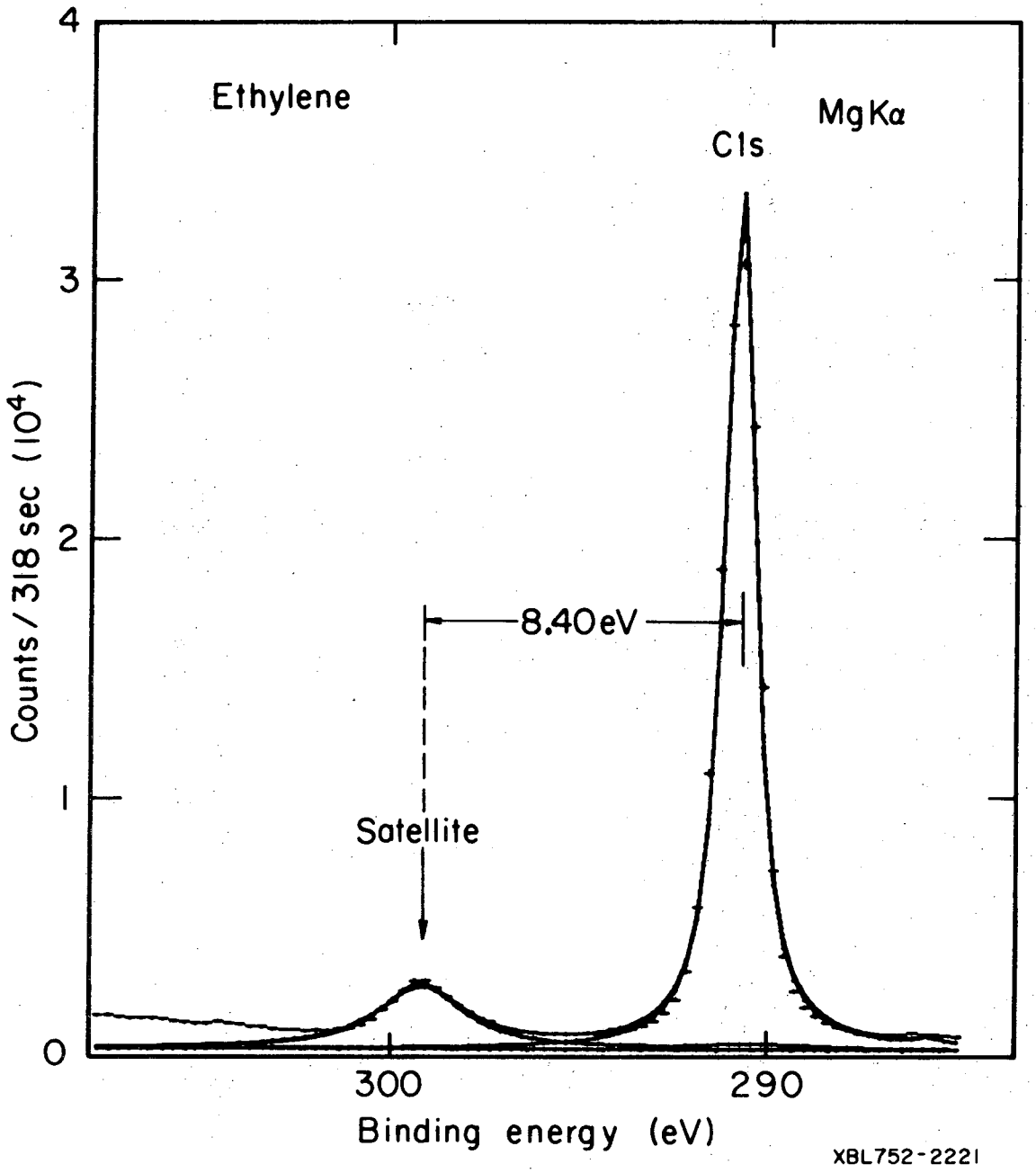

Fig. 45. Core spectrum of ethylene. Satellite is 0.21 of the main peak. Linewidths are: satellite 2.7(3) eV, carbon 1s, 0.84(2) eV.

peak (8.4 eV). Thus analogous transitions may be involved in both cases. It must be noted, however, that the core satellite is considerably broader than the C1s peak (2.7(3) eV versus 0.84 eV). In contrast, the satellite in the MO region has a linewidth roughly comparable to that of $2a_g$ and $2b_{3u}$ (2.3(1) eV versus 2.02(4) eV for $2a_g$ and 1.81(4) eV for $2b_{3u}$). The broadening of the core satellite may indicate that more than one transition is involved. If a simple shake-up mechanism is invoked (monopole transition in the valence shell accompanying ionization), then two final states would be expected, depending on the coupling of the three unpaired electrons in the ion. Broadening may also be due to a short lifetime or to vibrational excitation.[71] The latter would be especially likely if the shake-up involves a transition from a bonding to an anti-bonding orbital, as is probably the case here.

The possibility that the core and MO satellites correspond to analogous transitions is further supported by the intensity analysis. From Table XII we see that the core satellite is 21%, the intensity of C1s, while the MO satellite is 42%, the intensity of $2b_{3u}$ (39% the intensity of $2a_g$). Since the C1s peak is composed of two levels, $1a_g$ and $1b_{3u}$, of essentially the same binding energy, it seems possible that the shake-up transitions are associated with only one of them, most likely $1b_{3u}$ (judging from the energy separation discussed above).

Gelius[71] performed multiple-scattering Xα calculations[75] to determine the energy of the transition $1b_{1u} \rightarrow 1b_{2g}$ ($\pi \rightarrow \pi^*$) in the presence of a valence hole. $\pi \rightarrow \pi^*$ is a transition from the highest occupied orbital, $1b_{1u}$, to the lowest unoccupied orbital of ethylene, $1b_{2g}$. From optical data[73] on the neutral species, the energies of the resulting $^3B_{3u}$ and $^1B_{3u}$

states are 4.6 eV and 7.6 eV respectively. Gelius found an average energy of $\sim$ 5.4 eV from the hole-state calculation. Accordingly, he proposed that a $2a_g$ vacancy is involved in the MO satellite, since the latter is 3.74 eV away from the $2a_g$ peak. The satellite was therefore assigned as the $^2B_{3u}$ state: $2\underline{a}_g[1\underline{b}_{1u}\ 1b_{2g}^*(^3B_{3u})]$ (underlining indicates removal of an electron), which interacts with the $^2B_{3u}$ state resulting from simple ionization of a $2b_{3u}$ electron. A similar assignment may be possible in the core spectrum, provided the $1b_{1u} \rightarrow 1b_{2g}$ transition in the presence of a core hole is shown to have an energy close to 8.4 eV. A more likely explanation, which is probably valid at least for the core shake-up, is possible if the core hole is assumed to be localized. The reduction in symmetry in the ion means that the $1b_{1u} \rightarrow 1b_{2g}$ transition now becomes $b_2 \rightarrow b_2$, which is monopole. This mechanism is further supported by the agreement between the energies of the $1b_{1u} \rightarrow 1b_{2g}(^1B_{3u})$ transition, 7.6 eV, and the energy of the shake-up transition, 8.4 eV. More detailed calculations are needed, however, before a definite assignment can be made.

The change in the relative intensities of the various orbitals with photon energy is qualitatively the same as in N_2 and CO. At 1253.6 eV, the outer four orbitals have low intensity because they are predominantly 2p in character. When the exciting radiation energy is lowered to 132.3 eV, they are seen to gain intensity relative to $2a_g$ and $2b_{3u}$. With regard to relative intensities, the spectrum of ethylene is reminiscent of that of methane (Sec. VIII), both at the YMζ and the MgKα energy.

The experimental intensity ratios at the HeI,[70] HeII,[70] YMζ and MgKα energies are listed in Table XII, from which it is clear that the

relative intensities do not seem to change much in going from HeI to HeII radiation in this case. Both resemble the intensity ratios with YMζ radiation, except for the $2b_{3u}$ and $2a_g$ relative intensities. The theoretical results of Rabalais et al.[70] at 1254 eV and 132 eV are shown in columns 4 and 6, respectively. Only the intensity ordering of $3a_g + 1b_{2u}$ relative to $1b_{1u}$ (at 132 eV) is reversed by the calculations. Addition of the satellite intensity to $2b_{3u}$ brings it into very good agreement with theory at 132 eV. This is not the case at 1254 eV, however. The theoretical C1s relative intensity is too low, even without adding the area of the satellite to the experimental area of the main peak.

C. *Oxygen*

The spectra taken with MgKα and YMζ are shown in Fig. 46. Only the region below ∿ 30 eV binding energy was considered. Essentially the same region (12 - 28 eV) has been studied previously with the 584 Å and 304 Å He lines,[76] while the entire MO spectrum with MgKα was reported earlier by Siegbahn et al.,[37] referenced to the Ar $2p_{3/2}$ line.

The ground state electronic configuration of molecular oxygen is:

$$KK(\sigma_g 2s)^2(\sigma_u 2s)^2(\pi_u 2p)^4(\pi_g 2p)^2\ {}^3\Sigma_g^- \quad .$$

Ionization from $\pi_g 2p$ yields one doublet state, $X^2\Pi_g$. This level appears well resolved in our spectra, and therefore constitutes a good energy reference for the remaining states. Its vertical ionization potential is 12.33 eV from UPS, indicating that the 13.1 eV value of Siegbahn et al.[37] is probably too high. Edqvist et al.[76] measured a ${}^2\Pi_{1/2}$ - ${}^2\Pi_{3/2}$ spin-orbit splitting of 23 meV. Such a small splitting is, of course, beyond the

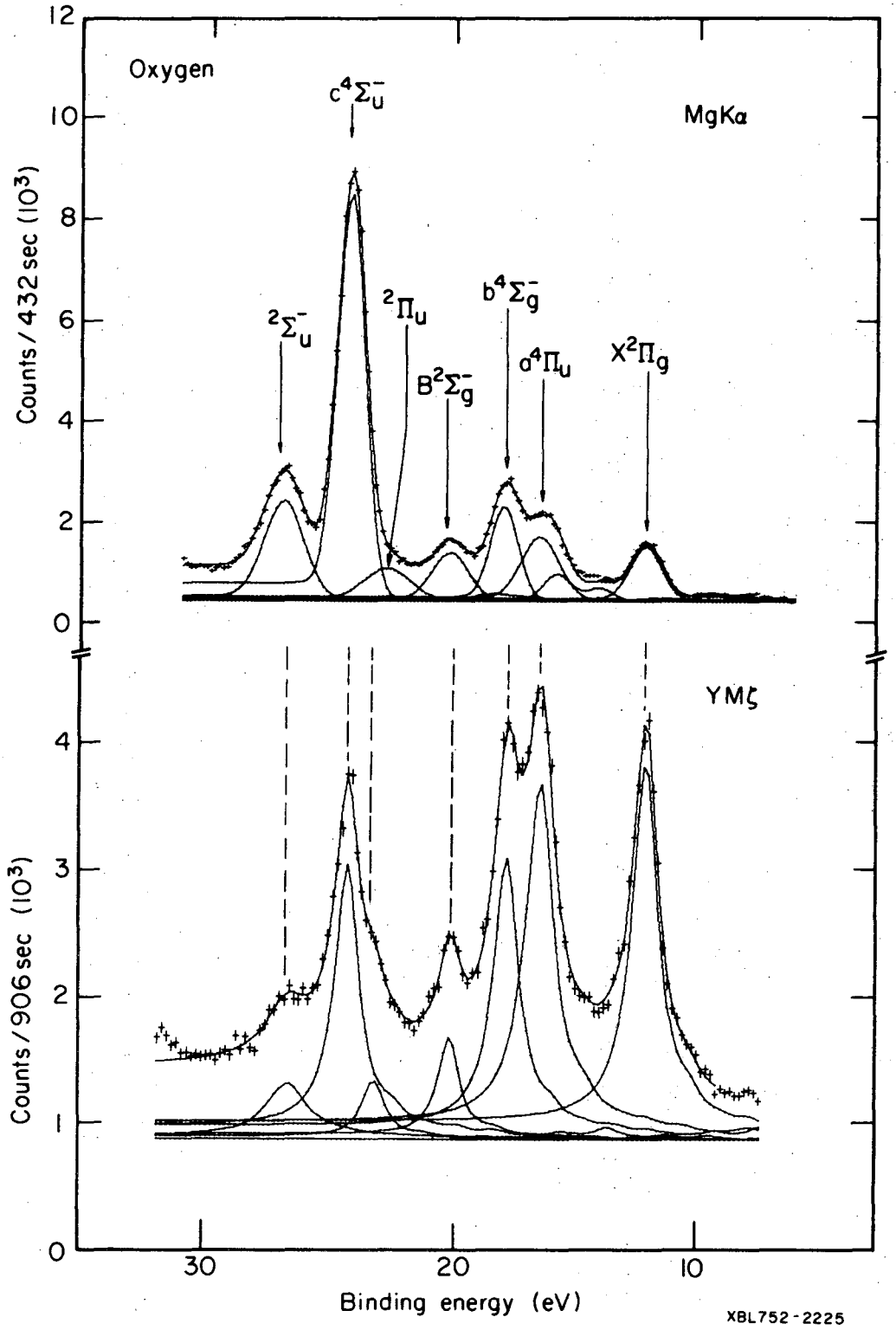

Fig. 46. Oxygen MgKα spectrum (top) and YMζ (bottom) up to ∿ 32 eV binding energy. With MgKα, counts were obtained at increments of ∿ 0.15 eV; and with YMζ at increments of ∿ 0.2 eV.

resolution capabilities of XPS. The intensity of the $X^2\Pi_g$ state relative to the $\sigma_u 2s$ levels is much enhanced in going from the MgKα to the YMζ spectrum, which is to be expected since this state is entirely 2p in character by symmetry.

Ionization from the fully occupied $\pi_u 2p$ orbital may yield the following states: $a^4\Pi_u$, $A^2\Pi_u$, $^2\Pi_u$, $^2\Pi_u$ and $^2\Phi_u$. As Edqvist et al.[76] point out, $^2\Phi_u$ cannot be reached by a one-electron transition from the ground state of O_2 and would therefore not be expected to appear in the photoelectron spectrum. The $a^4\Pi_u$ and $A^2\Pi_u$ states are severely overlapped in the UPS spectrum, and can only be separated by careful deconvolution of the two vibrational progressions.[76] Since their vertical I.P.'s differ by 1 eV (see Table XIII), it might have been possible to deconvolute them in the XPS spectrum, had it not been for the interference of the $b^4\Sigma_g^-$ state at 18.2 eV. As it is, only the $a^4\Pi_u$ state could be distinguished clearly, and its energy is in excellent agreement with the UPS result.

It is interesting that the intensity ordering of the partially resolved peaks at 16.7 eV and 18.2 eV is reversed in going from the MgKα to the YMζ spectrum. This confirms the 2s character of $b^4\Sigma_g$ and the 2p character of $a^4\Pi_u$.

In least-squares fitting of our experimental spectra we found that the two innermost peaks of the MgKα spectrum are best represented by Gaussians, while the remaining peaks may be fitted well with either Gaussians or Lorentzians. We only show the Gaussian fit in Fig. 46, but in Table XIII we list area ratios from both.

The quantitative relative intensities obtained by curve fitting are helpful in confirming the existence of $A^2\Pi_u$, which is otherwise very

TABLE XIII. Oxygen binding energies (eV) and MO relative intensities.

State	E_B(MgKα)	E_B(YMζ)	E_B(HeI)	I(MgG)[b]	I(MgL)[c]	I(YMζ)
$X^2\Pi_g$	12.33(2)[d]	12.33(1)[d]	12.33	1.00(3)	1.00(7)	1.00(2)
$a^4\Pi_u$	16.70(2)	16.72(2)	16.70	1.41(4)	1.0 (1)	1.00(5)
$A^2\Pi_u$	--	--	17.73	1.51(4)	1.7 (1)	0.71(7)
$b^4\Sigma_g$	18.17(2)	18.09(2)	18.17			
$B^2\Sigma_g$	20.39(7)	20.42(3)	20.43	1.0 (1)	0.7 (1)	0.22(9)
$^2\Pi_u$	23.0 (4)	23.47(6)	24.0	0.9 (6)	--	0.13(5)
$c^4\Sigma_u^-$	24.51(2)	24.56(2)	27.4	6.58(7)	--	0.65(4)
$^2\Sigma_u^-$	27.25(2)	26.96(8)	--	2.31(4)	--	0.2 (2)

[a] From Ref. 76.
[b] Gaussian fit.
[c] Lorentzian fit.
[d] Reference value.

difficult to observe directly by XPS because of insufficient resolution. Since this state is separated from $b^4\Sigma_g^-$ by only $\sim$ 0.5 eV (see Table XIII), the peak at $\sim$ 18 eV must be a composite of the two states. Now the ratio of $b^4\Sigma_g^-$ to $B^2\Sigma_g^-$ would not be expected to change by much when the excitation source is changed. From Table XIII, the relative intensity of the $\sim$ 18 eV peak ($b^4\Sigma_g^- + A^2\Pi_u$) to the $B^2\Sigma_g^-$ peak increases by a factor of $\sim$ 2 when MgKα is replaced with YMζ (taking the average of the Gaussian and Lorentzian fits). This behavior indicates the presence of a 2p-like state which gains in intensity at the YMζ energy.

Dixon and Hull[77] performed semi-empirical configuration interaction calculations on the oxygen ion resulting from Π_u ionization to determine the relative intensities of the different Π_u states. They predicted an intensity ratio of $a^4\Pi_u$ to the three $^2\Pi_u$ states of 2:0.34:0.001:0.64. Edqvist et al.[76] found an experimental $a^4\Pi_u$ to $A^2\Pi_u$ ratio of 2:0.3. They also identified the diffuse band at 24.0 eV in the HeII spectrum as $^2\Pi_u$, since its intensity relative to $a^4\Pi_u$ is 0.75:2. Our YMζ spectrum shows definite evidence for a state at 23.5 eV. The same state in the MgKα spectrum can be obtained by deconvolution. It is clear from Fig. 46 that the resolution with MgKα is somewhat better than with YMζ in this case. Thus the state at 23.5 eV must have a higher intensity at 132 eV relative to $c^4\Sigma_u^-$ than at 1254 eV. This confirms its p character and its assignment as $^2\Pi_u$. Our energy value is somewhat lower than the UPS result, however.

The energies of the $c^4\Sigma_u^-$ and $^2\Sigma_u^-$ states are $\sim$ 0.8 eV lower than the values reported by Siegbahn et al.[37] (25.3 eV and 27.9 eV respectively). Furthermore, the energy of $c^4\Sigma_u^-$ differs by almost 3 eV from the UPS result. Our measured splitting of 2.74(3) eV (MgKα value), on the other hand,

agrees better with the 2.6 eV result of ref. 37. It is interesting that the multiplet splitting in the MO region is a factor of two larger than the core splitting (1.1 eV). This is due to the larger exchange integrals between the unpaired electron of the ionized level and the electrons in the π_g orbital.[78]

The area ratio of $c^4\Sigma_u^-$ to $^2\Sigma_u^-$ appears to be in excess of the degeneracy value of 2. Positive deviations from the multiplet ratio have been observed in the core spectrum (see Sec. VI.A.) as well as in other systems. In the present case, part of the deviation may be an artifact of the fitting procedure.

The $a^4\Pi_u/^2\Pi_u$ ratio of 2:0.64 predicted by Dixon and Hull[77] appears to disagree with our experimental relative intensity of 2:1.3(6) with MgKα and 2:0.26(7) with YMζ. The MgKα value is too uncertain to permit conclusions to be drawn. On the other hand, the YMζ ratio is more reliable. Still, one must be cautious in interpreting the result since the area of $a^4\Pi_u$ may contain contributions from the unresolved $A^2\Pi_u$ state. The latter is separated from $a^4\Pi_u$ by 1 eV (see Table XIII) and is predicted to have an intensity 0.17 that of $a^4\Pi_u$. In view of this, the agreement with the calculation of Dixon and Hull must be considered satisfactory.

X. THE FLUORINATED METHANES CH_3F, CH_2F_2, CHF_3 AND CF_4

Most of the YMζ results presented thus far have dealt with systems with well established orbital assignments. The fluorinated methanes, on the other hand, present a challenge in this respect since some ambiguities in orbital ordering remain, in spite of numerous studies of this series.[79]

In a recent paper,[65] we reported the MgKα spectra of the fluorinated methanes, as well as methane and hydrogen fluoride. Discussion of both the binding energies and orbital assignments were given, the latter relying on the Gelius model discussed in Sec. VIII.C. In the present study, only relative binding energies were measured. The spectra are shown in Figs. 47 and 48. Comparison with the binding energy results of ref. 65, obtained with MgKα, is made in Table XIV. As expected, the agreement is good in most cases.

In columns 5, 6 and 7 of Table XIV we list the relative intensities obtained with HeII, YMζ and MgKα photon sources. Although the HeII intensity ratios are only approximate,[63a] they do reflect the general trend observed in earlier systems: HeII and YMζ relative intensities are roughly similar. Furthermore, the intensity ordering of the different bands is generally the same at both exciting energies.

Since no subshell cross section calculations have been performed for the fluoromethanes, we decided to analyze the data using the Gelius model. We have previously (Sec. VIII.C.) obtained the $\sigma(C2p)/\sigma(C2s)$ and $\sigma(F2p)/\sigma(F2s)$ ratios at 132 eV from the spectra of methane and hydrogen fluoride respectively. The $\sigma(F2s)/\sigma(C2s)$ ratio is also needed in order to calculate the relative intensities of the fluorinated methanes. The $3a_1$ and $4a_1$ levels of CH_3F were used, together with the populations

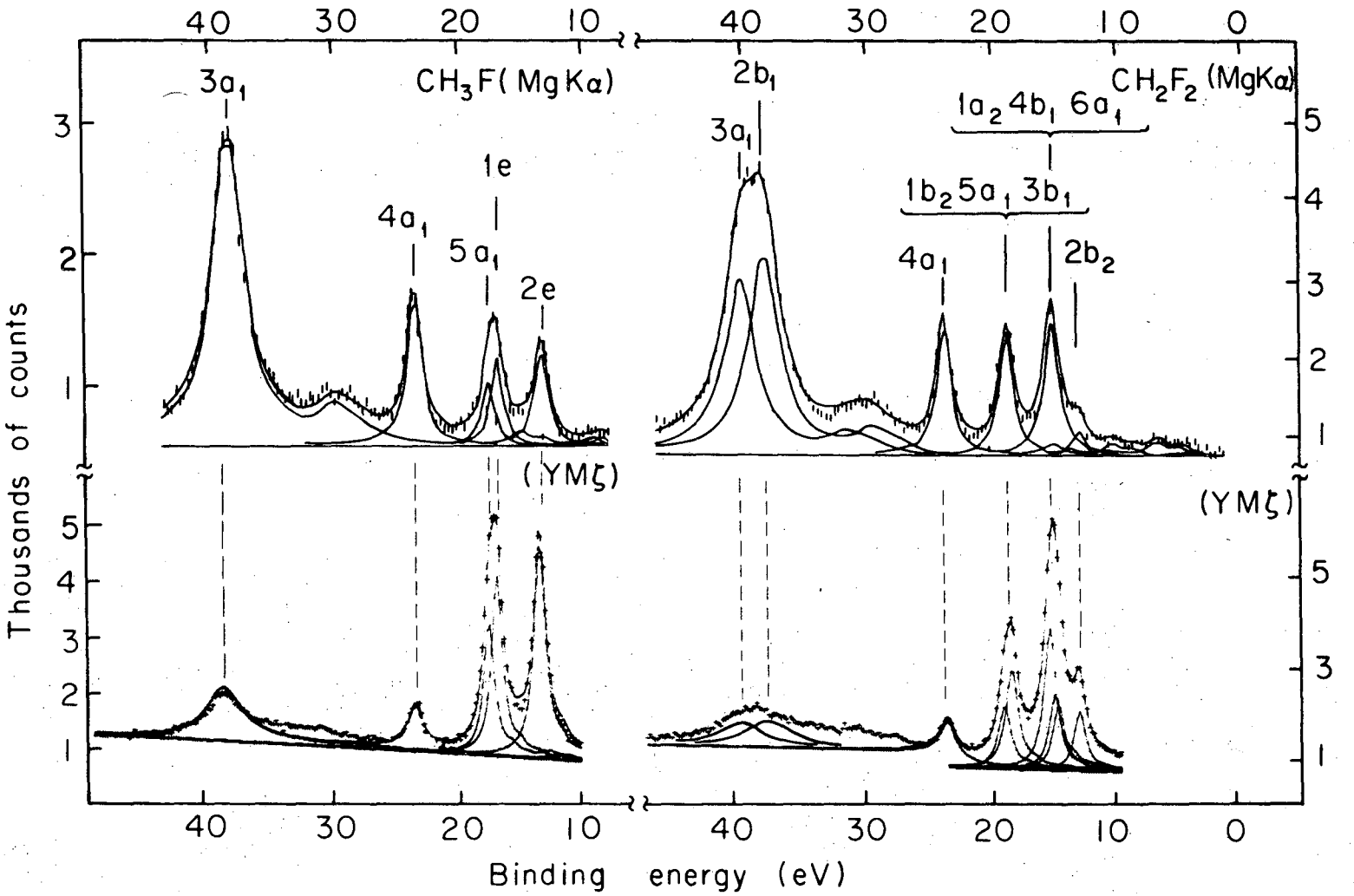

Fig. 47. MgKα and YMζ photoemission spectra of CH_3F and CH_2F_2 valence orbitals. Counts were obtained at ∿ 0.3 eV (with MgKα) and ∿ 0.2 eV (with YMζ) kinetic energy increments.

0 0 0 0 4 2 0 6 0 6 3

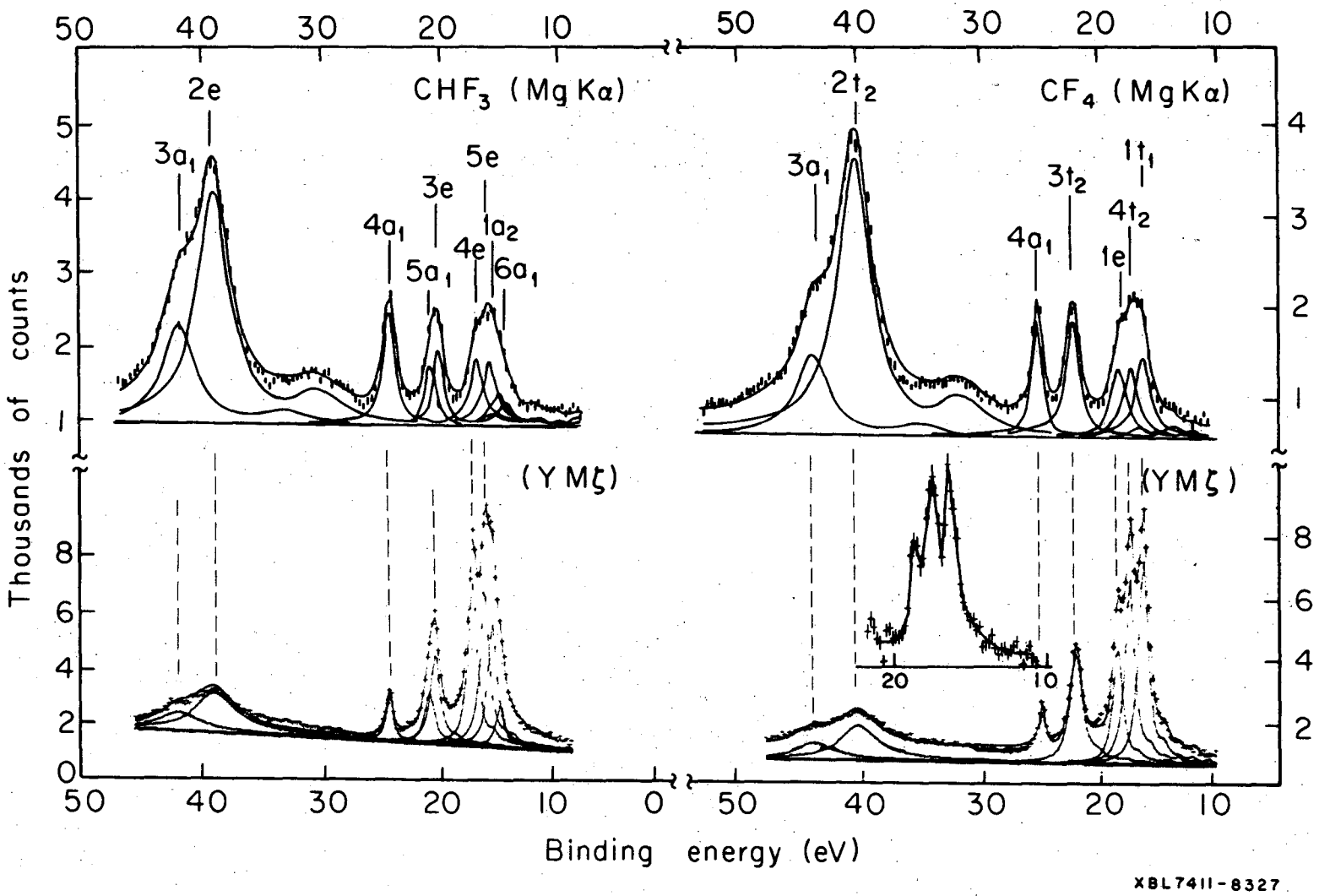

Fig. 48. MgKα and YMζ photoemission spectra of CHF_3 and CF_4 valence orbitals. Inset shows the outer three MO's of CH_4 measured at high resolution (clean anode). Counts were obtained at ∿ 0.3 eV (with MgKα) and ∿ 0.2 eV (with YMζ) kinetic energy increments.

TABLE XIV. Molecular orbital binding energies and intensity ratios for the fluorinated methanes.

Molecule	MO	E_B(MgKα)[a]	E_B(YMζ)[a]	I_{exp}(HeII)[b]	I_{exp}(MgKα)[c]	I_{exp}(YMζ)	I_G(YMζ)[d]	I_N(YMζ)[d]
CH_3F	$3a_1$	38.41(3)	38.41[e]		1.	1.	1.	1.
	→ $4a_1$	23.48(3)	23.48(6)[i]	0.3	.23(1)	.4 (1)	.40	.39
	$5a_1$	17.56(9)	17.55(8)	1.5	.08(2)	.9 (1)	1.00	1.00
	1e	16.85(7)	16.88(8)	($5a_1$ + 1e)	.11(2)	1.2 (1)	1.93	1.78
	2e	13.31(4)	13.35(6)	1.5	.13(1)	1.52(4)	1.30	1.56
CH_2F_2	$3a_1$	40.13(7)	40.13[e]		3.18(5)	∿1.3	1.55	1.50
	$2b_1$	38.20(7)	38.20[e]		3.57(6)	∿1.5	1.63	1.72
	→ $4a_1$	23.86(3)	23.86(3)[i]	0.4	1.	1.	1.	1.
	$1b_2$	19.76(7)	--	2.0	.14(1)[g]	--	1.41	1.25
	$5a_1$	19.07(3)	19.31(3)	($1b_2$+$5a_1$+$3b_1$)	.28(1)[g]	1.13(4)	1.73	1.61
	$3b_1$	18.51(4)	18.71(3)		.28(1)[g]	1.81(4)	1.93	1.91
	$1a_2$	15.61(2)	15.60(5)[f]	3.1	.32(1)[g]	2.5 (1)	2.33	2.47
	$4b_1$	15.20(2)	15.19(5)[f]	($1a_2$+$4b_1$+$6a_1$)	.32(1)[g]	1.3 (2)	2.29	2.55
	$6a_1$	14.91(2)	14.90(5)[f]		.25(1)[g]	1.1 (2)	1.74	1.98
	$2b_2$	13.17(2)	13.16(4)	1.0	.18(1)[g]	1.02(6)	1.12	1.45
CHF_3	$3a_1$	42.03(9)	42.03[e]		1.	1.	1.	1.
	2e	39.15(4)	39.15[e]		2.38(2)	2.17(7)	2.12	2.41
	→ $4a_1$	24.38(3)	24.38(3)[i]	0.3	.43(1)	.52(9)	.89	.97
	$5a_1$	20.89(3)	20.89(3)	1.4	.14(1)	.78(7)	1.02	1.00
	3e	20.25(3)	20.39(3)	($5a_1$ + 3e)	.21(1)	1.41(7)	2.52	2.66

0 0 0 0 4 2 0 6 0 6 4

TABLE XIV (continued)

Molecule	MO	$E_B(MgK\alpha)^a$	$E_B(YM\zeta)^a$	$I_{exp}(HeII)^b$	$I_{exp}(MgK\alpha)^c$	$I_{exp}(YM\zeta)$	$I_G(YM\zeta)^d$	$I_N(YM\zeta)^d$
CHF_3	4e	17.03(4)	17.08(3)	1.0	.21 [g]	2.35(8)	3.02	3.42
	5e	15.99(4)	16.00(4)[h]	1.5	.21 [g]	2.3 (1)	2.98	3.59
	$1a_2$	15.29(4)	15.30(4)[h]	0.9	.12 [g]	1.8 (1)	1.53	1.89
	$6a_1$	14.67(4)	14.60(4)[h]	0.6	.071[g]	.6 (2)	.92	1.28
CF_4	$3a_1$	43.81(10)	43.81[e]		1.	1.	1.	1.
	$2t_2$	40.30(4)	40.30[e]		3.45(3)	2.06(7)	3.16	3.73
	→ $4a_1$	25.11(2)	25.11(2)[i]	0.5	.55(1)	.61(6)	1.14	1.30
	$3t_2$	22.14(2)	22.21(3)	2.4	.59(1)	2.46(6)	3.69	4.09
	1e	18.43(4)	18.55(3)	1.6	.28(1)	2.09(7)	3.07	3.53
	$4t_2$	17.41(4)	17.48(3)	3.1	.38(1)	3.32(7)	4.42	5.49
	$1t_1$	16.23(3)	16.28(3)	3.7	.41(1)	3.66(6)	4.61	5.96

[a] E_B is MO binding energy in electron volts. $E_B(MgK\alpha)$ were obtained from ref. 65.

[b] From ref. 63a.

[c] From ref. 65.

[d] $I_G(YM\zeta)$ is the calculated relative intensity using the atomic cross section ratios in Table XV and gross populations, I_N using net populations.

[e] Separation from $4a_1$ level obtained from the MgKα results of ref. 65.

[f] Separations from ref. 65.

[g] Area ratios calculated from the Gelius model using CNDO populations.

[h] Separations obtained from the UPS results of ref. 63a.

[i] Reference value obtained from the XPS results of ref. 65; arrows indicate reference level.

calculated from the wavefunctions of Snyder and Basch.[64] The atomic cross section ratios obtained from Eq. (9) are shown in Table XV. Three types of populations were employed: gross, net and overlap (gross minus net). The photoelectric cross section of hydrogen was again taken to be zero.

TABLE XV. Derived relative atomic photoelectric cross sections at 132.3 eV photon energy.

Ratio, R	R(gross)[a]	R(net)[a]	R(overlap)[a]
$\sigma(C2p)/\sigma(C2s)$[b]	1.16	1.13	1.20
$\sigma(F2p)/\sigma(F2s)$[c]	1.38	1.22	1.82
$\sigma(F2s)/\sigma(C2s)$[d]	3.82	3.67	6.81

[a]Populations were calculated from the wavefunctions of ref. 64.
[b]From relative areas of $2a_1$ and $1t_2$ levels of methane.
[c]From relative areas of 2σ and 1π levels of hydrogen fluoride.
[d]From relative areas of $3a_1$ and $4a_1$ levels of methyl fluoride.

The two right columns of Table XIV show the calculated relative intensities. The gross and net populations were again computed from the wavefunctions of Snyder and Basch.[64] For CH_3F, the experimentally derived intensity ratios agree reasonably well with predictions based on either gross or net populations. In fitting the YMζ $3a_1$ peak we have deliberately excluded the structure to the right of the peak. This is probably due to satellite peaks from the outer levels,[80] and therefore should not be added to the area of $3a_1$. The large decrease in the relative intensity of this peak and a similar but somewhat less pronounced effect in the $4a_1$ peak in going from the MgKα to the YMζ spectrum, is characteristic of the

F2s and C2s atomic orbitals, respectively. Although particularly clear in CH_3F, it is also very apparent in the other fluorine derivatives.

The improved energy resolution in the YMζ spectrum makes it even clearer than before[65] that the peak at lowest binding energy arises from a single final state (the 2e orbital) while the next peak has two components (the $5a_1$ and 1e orbitals). In fitting this compound peak with two components we found good agreement between the 1e - $5a_1$ spacings as derived from the MgKα and the YMζ spectra (0.7 eV in both cases). The lower binding energy component was more intense in each spectrum, and the 1e peak was predicted to be more intense in each case. Thus on the basis of intensities the lower energy component of the second peak appears to belong to the 1e state.

In CH_2F_2 the $3a_1$ and $2b_1$ (fluorine 2s) states yield a low broad peak as expected. The two levels were deconvoluted by hand due to severe interference from the outer orbital satellites. Their relative intensities are therefore only approximate. The $4a_1$ (carbon 2s) state is also identified by its loss of relative intensity in the YMζ spectrum. The 19 eV peak gains in intensity relative to the inner three orbitals but loses relative to those at 13 and 15 eV. This is strong evidence for mixed 2s and 2p character, thus strongly supporting the previous assignment of the $1b_2$, $5a_1$, and $3b_1$ states to this peak. The YMζ data yield no new information on the order of these three states within the peak; in fact the MgKα spectrum was better in this respect, because only two component peaks were required to fit this peak in the YMζ spectrum. (The complete deconvolution of the MgKα spectrum of CH_2F_2 is shown in Fig. 3 of ref. 65.)

The high relative intensities of the 13 and 15 eV peaks in the YMζ

spectrum confirm their 2p character, in agreement with the previous assignments.[65] The $2b_2$ peak at 13 eV is well resolved. The 15 eV peak has a slightly rounded but symmetrical appearance, indicating that the $1a_2$, $4b_1$, and $6a_1$ states lie close in energy.

The CHF_3 and CF_4 spectra are shown in Fig. 48. Their general appearance is similar to that of CH_2F_2: tightly bound compound F(2s) peaks near 40 eV, the $4a_1$ (C2s) peak near 25 eV, and two more peaks, of which the one near 22 eV has strongly mixed 2s and 2p character. The CF_4 spectrum has been thoroughly discussed before, and we note only that the YMζ spectrum (see inset) shows a resolution of the 1e, $4t_2$, and $1t_1$ peaks that rivals the results obtained by Gelius[71] with monochromatic AlKα x-rays.

The CHF_3 spectrum illustrates the power of using YMζ radiation. The peak at 21 eV is asymmetric toward high binding energy. Since the 3e component peak is predicted to have at least twice the intensity of the $5a_1$ peak, the former appears to have the lower binding energy. The spectral area between 14 and 18 eV requires at least four peaks for a fit: its detailed shape further requires that the peak intensities increase monotonically with binding energy, with the exception that the two most tightly bound peaks can have similar intensities. The fit shown in Fig. 48 was based on the known UPS (vertical) energy separations[63a] among the three least tightly bound components. The derived intensities agree fairly well with predicted values, confirming the listed level ordering.

In summary, the spectra presented here again confirmed the anticipated changes in relative intensities that were expected to accompany this large reduction in photon energy. Intensity ratio predictions based on

the simple atomic orbital population model show generally good qualitative agreement with experiment. These results give no basis for choice among gross or net populations. The YMζ line appears to possess real diagnostic value for molecular photoelectron spectroscopy.

ACKNOWLEDGMENTS

Professor David Shirley, my research director, played a major role in my scientific development, especially during the "formative" years of graduate study. I will remember him not only for his scientific insight, but also for his extraordinary ability to motivate and lead research projects.

Both in scientific and other matters, I have learned a lot from the other members of my research group. I would especially like to mention Dr. D. "Bill" Davis, Mr. Sefik Süzer, Mr. Richard Martin, and Miss Bernice Mills. Drs. Winfield Perry and Richard Rietz from Professor Jolly's group were also helpful, particularly in inorganic chemical work. More recently, I would like to acknowledge the friendliness and assistance of Dr. Shuit Tong Lee.

Professor Ronald Cavell (University of Alberta) and Dr. Wigbert Siekhaus provided useful advice during some of the phases of this work.

I enjoyed many hours of machining under the cheerful supervision of Mr. Charles Butler. His day-by-day assistance with technical problems is sincerely appreciated. Also in the mechanical department, I wish to thank Mr. D. N. "Ed" Voronin, who was involved in much of the design work needed for this thesis. I would also like to acknowledge Mr. Eugene Miner for discussions concerning the photoelectron spectrometer of the future, and Mr. Joseph Katz, who worked tirelessly to maintain our electronics equipment, even on weekends and holidays.

Thanks are due to the U. S. Energy Research and Development Administration and the American people for generous financial support.

The last year or so of my study at Berkeley was brightened by the love and affection of Miss Joan Parham.

REFERENCES

1. U. Gelius, E. Basilier, S. Svensson, T. Bergmark and K. Siegbahn, J. Electron Spectrosc. 2, 405 (1974).
2. J. A. Bearden, Rev. Mod. Phys. 39, 78 (1967).
3. K. Siegbahn, C. Nordling, A. Fahlman, R. Nordberg, K. Hamrin, J. Hedman, G. Johansson, T. Bergmark, S. E. Karlsson, I. Lindgren and B. Lindberg, ESCA - Atomic, Molecular and Solid State Structure Studied by Means of Electron Spectroscopy (Almqvist and Wiksells AB, Stockholm, Sweden, 1967).
4. M. O. Krause and F. Wuilleumier, Phys. Letters 35A, 341 (1971).
5. M. O. Krause, Chem. Phys. Letters 10, 65 (1971).
6. W. C. Price, A. W. Potts, and D. G. Streets, Electron Spectroscopy (D. A. Shirley, ed., North-Holland, Amsterdam, 1972), p. 187.
7. L. L. Lohr, Jr., ibid, p. 245.
8. M. O. Krause and F. Wuilleumier, J. Phys. B 5, L143 (1972).
9. F. Wuilleumier and M. O. Krause, Phys. Rev. A 10, 242 (1974).
10. D. P. Spears, J. H. Fischbeck and T. A. Carlson, Phys. Rev. A 9, 1603 (1974).
11. K. Siegbahn, Alpha-, Beta- and Gamma-Ray Spectroscopy, Vol. I (K. Siegbahn, ed., North-Holland, Amsterdam, 1965), Ch. III.
12. See for example D. W. Davis, R. L. Martin, M. S. Banna and D. A. Shirley, J. Chem. Phys. 59, 4235 (1973).
13. C. S. Fadley, G. L. Geoffroy, S. B. M. Hagström and J. M. Hollander, Nucl. Instr. Methods 68, 177 (1969).
14. G. Johansson, J. Hedman, A. Berndtsson, A. Klasson and R. Nilsson, J. Electr. Spectrosc. 2, 295 (1973).
15. C. S. Fadley, Ph.D. Thesis, University of California, UCRL-19535, Ch. III.
16. See for example, a) T. D. Thomas, J. Chem. Phys. 52, 1373 (1970); and b) W. L. Jolly, P. Finn, R. K. Pearson and J. M. Hollander, Inorg. Chem. 10, 378 (1971).
17. D. W. Davis, Ph.D. Thesis, University of California Lawrence Berkeley Laboratory, LBL-1900, Ch. I.
18. Reference 3, p. 59.

19. The author was encouraged to take this approach by Professor R. G. Cavell (University of Alberta, Department of Chemistry).
20. B. L. Henke and E. S. Ebisu, Advances in X-Ray Analysis (C. L. Grant et al, eds., Plenum Press, New York, 1974), 17, 150.
21. F. Wuilleumier, Advances in X-Ray Analysis (Birks et al., eds., Plenum Press, New York, 1973), 16, 70.
22. W. Bambynek, B. Crasemann, R. W. Fink, H.-U. Freund, H. Mark, C. D. Swift, R. E. Price and P. V. Rao, Rev. Mod. Phys. 44, 716 (1972).
23. Eugene Miner, Lawrence Berkeley Laboratory, private communication.
24. The author acknowledges the skill of J. Bryan in winding these filaments.
25. L. Yaffe, Ann. Rev. Nucl. Sci. (E. Segrè, ed., Annual Reviews, Inc., Palo Alto, California, 1962), 12, 153.
26. a) A. J. Caruso and H. H. Kim, Rev. Sci. Instrum. 39, 1059 (1968);
b) S. Hayakawa, T. Kato, F. Makino, H. Ogawa, Y. Tanaka and K. Yamashita, Jap. J. Appl. Phys. 9, 542 (1970).
27. M. O. Krause, "Photoelectrons: Counterparts of Roentgen Rays", International Conference on X-Ray Processes in Matter (Helsinki University of Technology, Otaniemi, Finland, July 29 - August 1, 1974).
28. For a more complete discussion of the program, see reference 15, Ch. IV.A.
29. C. E. Moore, Atomic Energy Levels, National Bureau of Standards Circular No. 467 (U.S. GPO, Washington, D.C., 1947), 1, 92.
30. T. A. Carlson and M. O. Krause, Phys. Rev. A 140, 1057 (1965).
31. a) M. Siegbahn and T. Magnusson, Z. Physik 88, 559 (1934);
b) J. A. Bearden, Rev. Mod. Phys. 39, 78 (1967);
c) G. Dannhäuser and G. Wiech, Phys. Letters 35A, 208 (1971).
32. R. K. Bohn and S. H. Bauer, Inorg. Chem. 6, 304 (1967).
33. P. S. Bagus, M. Schrenk, D. W. Davis and D. A. Shirley, Phys. Rev. A 9, 1090 (1974).
34. S. Pignataro and G. Distefano, J. Electron Spectrosc. 2, 171 (1973).
35. T. Åberg, Ann. Acad. Sci. Fenn A 6, 308, 1 (1969).
36. U. Gelius, in Electron Spectroscopy (D.A.Shirley, ed., North-Holland, Amsterdam, 1972), p. 311.

37. K. Siegbahn, C. Nordling, G. Johansson, J. Hedman, P. F. Hedén, K. Hamrin, U. Gelius, T. Bergmark, L. O. Werme, R. Manne and Y. Baer, ESCA Applied to Free Molecules (North-Holland, Amsterdam, 1969).
38. See for example references 12, 33 and 37 (pp. 56-61).
39. U. Gelius, S. Svensson, H. Siegbahn, E. Basilier, Å. Faxälv and K. Siegbahn, Chem. Phys. Letters 28, 1 (1974).
40. W. Meyer, J. Chem. Phys. 58, 1017 (1973).
41. D. W. Davis, D. A. Shirley and T. D. Thomas, J. Am. Chem. Soc. 94, 6565 (1972).
42. For a review of models of this kind, see D. W. Davis and D. A. Shirley, J. Electron Spectrosc. 3, 137 (1974).
43. D. T. Clark, D. Kilcast, D. B. Adams and W. K. R. Musgrave, J. Electron Spectrosc. 1, 227 (1972).
44. P. G. Wilkinson, Can. J. Phys. 34, 596 (1956).
45. L. J. Aarons, M. F. Guest and I. H. Hillier, J. Chem. Soc., Faraday Trans. (Series 2) 68, 1866 (1972).
46. R. W. Shaw, Jr., T. X. Caroll and T. D. Thomas, J. Am. Chem. Soc. 95, 5870 (1973).
47. See for example E. L. Muetterties, Accounts Chem. Res. 3, 266 (1970).
48. This is known from experiment, see reference 20, Vol. 13, p. 639.
49. Reference 29, Vol. II, p. 174.
50. Reference 37, pp. 158 and 162.
51. W. Mehlhorn, Z. Physik 187, 21 (1965).
52. E. H. S. Burhop and W. N. Asaad, Advances in Atomic and Molecular Physics (D. R. Bates and I. Esterman, eds., Academic Press, New York, 1972), 8, 163.
53. K. Codling and R. D. Madden, Phys. Rev. Letters 12, 106 (1964).
54. U. Fano and J. W. Cooper, Rev. Mod. Phys. 40, 441 (1968).
55. See for example, a) F. Combet-Farnoux, J. Phys. (Paris) 30, 521 (1969); b) M. Ya. Amusia, N. A. Cherepkov and L. V. Chernysheva, Zh. Eksp. Teor. Fiz. 60, 160 (1971), [Sov. Phys.-JETP 33, 90 (1971)]; c) M. Ya. Amusia, V. K. Ivanov, N. A. Cherepkov and L. V. Chernysheva, Phys. Lett. A 40, 361 (1972).

56. D. J. Kennedy and S. T. Manson, Phys. Rev. A 5, 227 (1972).
57. T. P. Debies and J. W. Rabalais, J. Am. Chem. Soc. 97, 487 (1975).
58. The wavefunctions are the Hartree-Slater functions (central field) tabulated by Herman and Skillman. See F. Herman and S. Skillman, Atomic Structure Calculations (Prentice-Hall, Englewood Cliffs, New Jersey, 1963).
59. C. S. Fadley, Chem. Phys. Letters 25, 225 (1974).
60. T. E. H. Walker and J. T. Waber, Phys. Rev. Letters 30, 307 (1973).
61. J. W. Cooper, Phys. Rev. A 128, 681 (1962).
62. Methane was studied with AlKα, instead of MgKα, by B. E. Mills.
63. See for example, a) CH_4: C. R. Brundle, M. B. Robin and H. Basch, J. Chem. Phys. 53, 2196 (1970);
b) NH_3: D. W. Turner, C. Baker, A. D. Baker and C. R. Brundle, Molecular Photoelectron Spectroscopy (Wiley-Interscience, London, 1970).
c) H_2O: C. R. Brundle and D. W. Turner, Proc. Roy. Soc. A 307, 27 (1968).
d) HF: C. R. Brundle, Chem. Phys. Letters 7, 317 (1970).
64. L. C. Snyder and H. Basch, Molecular Wave Functions and Properties (John Wiley & Sons, New York, 1972).
65. M. S. Banna, B. E. Mills, D. W. Davis and D. A. Shirley, J. Chem. Phys. 61, 4780 (1974).
66. a) J.-T. J.Huang and F.O.Ellison, Chem. Phys. Letters 25, 43 (1974);
b) J.-T. J.Huang and F.O.Ellison, J. Electron Spectrosc. 4, 233 (1974).
67. V. I. Nefedov, N. P. Sergushin, I. M. Band and M. B. Trzhaskovskaya, J. Electron Spectrosc. 2, 383 (1973).
68. F. O. Ellison, J. Chem. Phys. 61, 507 (1974).
69. R. L. Martin, B. E. Mills and D. A. Shirley, to be published.
70. J. W. Rabalais, T. P. Debies, J. L. Berkosky, J.-T.J.Huang and F. O. Ellison, J. Chem. Phys. 61, 516 (1974).
71. U. Gelius, J. Electron Spectrosc. 5, 985 (1974).
72. M. B. Robin, N. A. Kuebler and C. R. Brundle, in Electron Spectroscopy (D. A. Shirley, ed., North-Holland, Amsterdam, 1972), p. 351.
73. A. J. Merer and R. S. Mulliken, Chem. Rev. 69, 639 (1969).
74. A. Berndtsson, E. Basilier, U. Gelius, J. Hedman, R. Nilsson, C. Nordling and S. Svensson, to be published.

75. J. W. D. Connolly, H. Siegbahn, U. Gelius and C. Nordling, J. Chem. Phys. 58, 4265 (1973).

76. O. Edqvist, E. Lindholm, L. E. Selin and L. Åsbrink, Physica Scripta 1, 25 (1970).

77. R. N. Dixon and S. E. Hull, Chem. Phys. Letters 3, 367 (1969).

78. J. B. Mann, Atomic Structure Calculations I. Hartree-Fock Energy Results for the Elements Hydrogen to Lawrencium, Los Alamos Report No. LA-3690 (1967), p. 45.

79. For UPS results see A. W. Potts, J. H. Lempka, D. G. Streets and W. C. Price, Phil. Trans. Roy. Soc. London A 268, 59 (1970), and reference 63a above. For an x-ray emission study see R. E. LaVilla, J. Chem. Phys. 58, 3841 (1973).

80. For an electron impact study of the Rydberg levels of the fluoromethanes, see W. R. Harshbarger, M. B. Robin and E. N. Lassettre, J. Electron Spectrosc. 1, 319 (1973).

0 0 0 0 4 2 0 6 0 7 0

LEGAL NOTICE

This report was prepared as an account of work sponsored by the United States Government. Neither the United States nor the United States Energy Research and Development Administration, nor any of their employees, nor any of their contractors, subcontractors, or their employees, makes any warranty, express or implied, or assumes any legal liability or responsibility for the accuracy, completeness or usefulness of any information, apparatus, product or process disclosed, or represents that its use would not infringe privately owned rights.

TECHNICAL INFORMATION DIVISION
LAWRENCE BERKELEY LABORATORY
UNIVERSITY OF CALIFORNIA
BERKELEY, CALIFORNIA 94720